Mechanisms and Prediction of Abrasive Wear: Unveiling the Impact of Waviness and Oscillation

Zur Erlangung des akademischen Grades eines

DOKTORS DER INGENIEURWISSENSCHAFTEN (Dr.-Ing.)

von der KIT-Fakultät für Maschinenbau des

Karlsruher Instituts für Technologie (KIT)

angenommene

DISSERTATION

von

M. Sc. Yulong Li

Abstract

Abrasive wear is a dominant factor in limiting the performance and lifespan of tribological systems in many engineering fields. Understanding the complex mechanisms of abrasive wear is essential for prolonging machinery lifetime and reducing energy consumption. In this thesis, experiments were conducted using bearing steel (100Cr6, AISI 52100) pins and disks in a flat-on-flat contact configuration; Al_2O_3 slurries with different particle sizes (5 and 13 µm) were chosen as the interfacial media to induce abrasion.

First, the results presented herein indicate that a speed-induced hydrodynamic effect occurred and significantly altered the systems' tribological behavior in tests performed using a 5 µm sized Al_2O_3 slurry, which was less pronounced with 13 µm sized particle. The hydrodynamic effect can lead to a 14% increase in lubricant film thickness and a decrease in friction of around 2/3, accompanied by a transition from two-body abrasion to three-body abrasion and a change in wear mechanism from microcutting and microploughing to fatigue wear.

Second, typically overlooked factors like the disk waviness and the oscillation of contacting surfaces (due to disk mounting tilt), can lead to frictional fluctuations and uneven wear, even when efforts are made to minimize and control these factors. The results reveal two intriguing findings: (1) even small waviness (a 2 µm "hill" along the 132 mm sliding track) can significantly increase the friction coefficient (up to 91%); (2) areas that have the highest friction tend to appear on the negative slope of the oscillation. By integrating key features from disk waviness profiles and oscillation, we introduce a novel tool, the "High Friction Predictor", specifically identifying areas on the sliding track where friction is likely higher than at other areas. This thesis unveils the capacity to establish guidelines for adjusting surface topography and surface tilt to achieve desired tribological properties.

Zusammenfassung

Abrasiver Verschleiß ist ein kritischer Faktor für die Leistung wie auch die Lebensdauer von tribologischen Kontakten, wie sie in vielen technischen Anwendungsbereichen vorkommen. Grundlegendes Verständnis der komplexen Mechanismen des abrasiven Verschleißes ist essentiell, um die Lebensdauer von Maschinen zu verlängern und deren Energieverbrauch zu reduzieren. In dieser Dissertation wurde das tribologische Verhalten von Wälzlagerstählen (100Cr6, AISI 52100) in einem Stift-Scheibe-Tribometer mit Flächenkontakt untersucht. Um abrasiven Verschleiß zu induzieren, wurden den Experimenten Aufschlämmungen mit Al_2O_3-Partikeln unterschiedlicher Größen (5 und 13 µm) als Grenzflächenmedium hinzugefügt.

Die experimentellen Ergebnisse zeigen, dass ein geschwindigkeitsinduzierter hydrodynamischer Effekt auftritt. Dieser verändert das Reibverhalten bei den tribologischen Experimenten in welchen 5 µm große Al_2O_3-Partikel hinzugegeben wurde erheblich. Dieser Effekt ist weniger ausgeprägt bei der Zugabe von 13 µm großen Al_2O_3-Partikeln. Dieser geschwindigkeitsabhängige hydrodynamische Effekt kann zu einer Zunahme der Schmierfilmdicke um 14% und einer Abnahme der Reibung um etwa zwei Drittel führen, begleitet von einem Übergang von Zwei-Körper-Abrasion zu Drei-Körper-Abrasion und einer Änderung des Verschleißmechanismus von Mikroschneiden und -pflügen zu Oberflächenzerüttung.

Desweiteren wurde der Einfluss der, oft übergangenen, Faktoren wie die Scheibenwelligkeit und die Oszillation der Kontaktflächen (aufgrund der Neigung der Scheibe in der Befestigung) untersucht. Diese führen zu inkonsistenter Reibung und ungleichmäßigem Verschleiß, selbst wenn diese Faktoren minimiert und kontrolliert wurden. Die Ergebnisse erlauben zwei wichtige Erkenntnisse: (1) Selbst geringfügige Welligkeiten (2 µm Höhendifferenz entlang

einer 132 mm langen Verschleißspur) können den Reibungskoeffizienten signifikant erhöhen (um bis zu 91%); (2) Bereiche mit einem Abfall in der Oszillation scheinen die höchesten Reibkoeffizienten hervorzurufen. Durch die Analyse wichtiger Merkmale der Scheibenwelligkeitsprofile und der Oszillation wurde der "Hochreibungs-Indikator" entwickelt. Dieser identifiziert die Sektoren der Verschleißspur, in denen die Reibung wahrscheinlich höher ist als in anderen Sektoren. Diese Dissertation gibt erste Richtlinien zur Anpassung der Oberflächenstruktur und der Oberflächenneigung, um die gewünschten tribologischen Eigenschaften zu erreichen.

Acknowledgment

I would like to take this opportunity to express my heartfelt gratitude to the many individuals who have supported me during my doctoral journey. Thanks to their unwavering support, encouragement, and guidance, I could successfully complete this challenging and rewarding program.

First and foremost, I would like to thank my supervisor, Prof. Dr. Christian Greiner, for his exceptional mentorship, expert guidance, and constructive feedback throughout my research. His unwavering support, dedication, and encouragement played a vital role in shaping the direction and scope of my research, and I could not have achieved this milestone without his help. He is a cordial mentor to my scientific life.

I very much appreciated all the help that I received to finish this thesis. I would like to extend thanks to Dr. Nikolay Garabedian for countless discussions of the research. His support was not only academic but also emotional, and I am deeply appreciative of everything he has done for me. I am very grateful to Dr. Paul Schreiber for his help in providing a solid start to my doctoral career. I have learned so much from him, including valuable insights into academic research, scientific rigor, and teamwork skills. I also would like to thank Dr. Johannes Schneider for his comprehensive assistance in all aspects of my work at KIT. His research guidance and optimistic attitude have been a great source of inspiration and benefit to me. I very much appreciate the discussion with Prof. Dr. Peter Gumbsch at every "Gernsbach meeting"; his research spirit and scientific literacy deeply moved me.

I want to express my most profound appreciation to all of my scientific colleagues who have joined me in facing the daily challenges of tribology. Their expertise, dedication, and collaborative efforts have been instrumental in advancing my research and understanding in

Yulong Li

Karlsruhe, Nov. 2023

Publications

Contributions in journals:

Parts of this work have already been published in the following peer-reviewed journals. I have obtained permission from all the co-authors and publishers to partially use the published results (including texts, equations, tables, and figures) in the current thesis:

- **Y. Li**, P. Schreiber, J. Schneider, C. Greiner, Tribological mechanisms of slurry abrasive wear. *Friction* 11, 1079–1093 (2023).

- **Y. Li**, N. Garabedian, J. Schneider, C. Greiner, Waviness Affects Friction and Abrasive Wear. *Tribology Letters* 71, 64 (2023).

- **Y. Li**, N. Garabedian, J. Schneider, C. Greiner, Prediction of uneven wear and friction. (in preparation)

More peer-reviewed journal publications I was involved in:

- N. Garabedian, P. Schreiber, I. Blatter, A. Dollmann, C. Haug, D. Kümmel, **Y.Li**, F. Meyer, C. Morstein, J. Rau, M. Weber, J. Schneider, P. Gumbsch, C. Greiner, Generating FAIR research data in experimental tribology. *Scientific Data* 9, 315 (2022).

Contributions in conferences (*presenter):

- **Y. Li***, P. Schreiber, J. Schneider, C. Greiner, Tribological mechanisms in abrasive suspensions, MSE 2020 - Materials Science and Engineering Congress, Sep 22-Sep 25 2020, Darmstadt, Germany. (Poster)

- **<u>Y. Li*</u>**, P. Schreiber, J. Schneider, C. Greiner, Abrasive mechanism under lubricated condition, European Symposium on Friction, Wear and Wear Protection 2021, Nov 18-19 2021, online. (Oral talk)

- **<u>Y. Li*</u>**, N. Garabedian, J. Schneider, C. Greiner, Is friction positively correlated with abrasive particle size?, NORDTRIB 2022, June 14-17 2022, Ålesund, Norway. (Oral talk)

- **<u>Y. Li*</u>**, N. Garabedian, J. Schneider, C. Greiner, What controls abrasive wear?, MSE 2022 - Materials Science and Engineering Congress, Sep 27-Sep 29 2022, Darmstadt, Germany. (Oral talk)

- **<u>Y. Li</u>**, N. Garabedian*, J. Schneider, C. Greiner, Inevitable deviations affect tribological behavior, 2023 STLE Annual Meeting, May 21-25 2023, California, the U.S. (Oral talk)

Table of Contents

List of Abbreviations and Symbols

Abbreviations

Abbreviation	Explanation
AFM	Atomic force microscopy
AISI	American Iron and Steel Institute
ASME	The American Society of Mechanical Engineers
Al_2O_3	Aluminum oxide
CWL	Chromatic white light
DIN	German Institute for Standardisation
DFT	Discrete Fourier Transform
EHL	Elastohydrodynamic Lubrication
FFT	Fast Fourier Transform
FVA 1	Base oil according to the standard set by the Forschungsvereinigung Antriebstechnik e.V.
ISO	International Organization for Standardization
LTA	Lubricated to abrasive experiments
PSD	Power spectral density
RMS	Root mean square of roughness profile
SEM	Scanning electron microscopy
SiC	Silicon carbide
STFT	Short-time Fourier transform
TEM	Transmission electron microscopy
TiN	Titanium nitride

Symbols

Symbol	Description	Unit
A_z	The amplitude of oscillation	mm
d	Particle dimension	mm
F_x	Friction force	N
F_z	Normal force	N
g	A window function centered at time t	-
h	Film thickness	μm
Δh	Change in film thickness	μm
j	Imaginary unit to represent the phase of frequency components	-
k_x	Lateral stiffness of a single Hookean spring	N/mm
k_z	Normal stiffness of a single Hookean spring	N/mm
lr	Length of the roughness profile	Mm
m	Mean of the friction coefficient along the sliding track	-
η	Dynamic viscosity of a fluid	Pa·s
N	Load on the friction contact	N
P	The frictional power	J
R_a	Arithmetical mean deviation of roughness profile	μm
R_v	Relative variation in film thickness	μm
t	Time	s
μ	Friction coefficient	-
μ_x	Friction coefficient of a sector on sliding track	-
u_x	Lateral displacement of a single Hookean spring	mm
u_z	Normal displacement of a single Hookean spring	mm
u_{zm}	Average value of oscillation	mm
W_a	Arithmetic average of surface heights	μm
W_t	Total height of waviness profile	μm
$w(ft)$	A dimensionless function describing the oscillation	-
ω	Frequency	Hz
v	Sliding speed	m/s
x	Signal to be transformed	-
z	Z-score of friction coefficient	-
σ	Standard deviation of the friction coefficient along the sliding track	-

1 Motivation

The flourishing of human civilization has brought significant alterations to the environment. The perpetual melting of glaciers and the escalating frequency and ferocity of extreme weather phenomena, such as storms and floods, underscore the need for cleaner energy production and more efficient technologies. To this end, optimizing mechanical systems to minimize friction and wear represents a crucial way to achieve carbon neutrality.

Researchers have made sophisticated designs in lubrication, sealing, and filtration. However, abrasive wear is inevitable. One critical aspect of abrasive wear is that it causes significant material removal, and this process is closely tied to the operational mechanisms of tribological systems. Therefore, a comprehensive understanding of the abrasive wear mechanisms is essential for further optimizing tribological systems.

Additionally, abrasive wear can lead to a sudden increase and significant fluctuations in friction force, which has been seen as a prevalent manifestation of abrasive wear [1–4]. The large fluctuations in friction force can present considerable challenges to the reproducibility and reliability of tribological experiments. For example, consider an extreme case where you conduct two identical experiments, yielding friction forces of 2.0±0.5 N and 1.99±1.5 N, respectively. If we only focus on the average values, one might conclude that the experiments exhibit excellent reproducibility, with only a 0.01 N difference. However, when considering the standard deviation, it is highly likely that they exhibit entirely distinct tribological behaviors. Notably, in tribology, the standard deviation is often not the primary indicator that tribologists employ when comparing friction forces and it is frequently overlooked.

In addition to frictional fluctuations, certain factors in tribological experiments are often regarded as simple parameters and tend to be ignored. For instance, surface topography and oscillation of the contacting surfaces (arising from misalignment in the setup and machine vibration). Is there a correlation between these simple parameters and big frictional fluctuations on abrasive wear?

The present study aims to investigate the wear mechanisms in abrasive wear much more comprehensively, and subsequently provide insightful explanations for the complex phenomena occurring during abrasive wear.

2 State of Art

2.1 Basic Concepts and Terminology of Tribology

The science that studies phenomena and mechanisms that occur during the relative motion of interacting surfaces, known as tribology, has a long and complex history that spans many centuries and cultures, although the word "tribology" was only first coined in 1966 by Peter Jost [5]. The term was derived from the Greek word "tribos", meaning rubbing [6], and includes the study and application of the principles of friction, lubrication, and wear.

2.1.1 Friction

Friction is defined as the force that resists relative motion between surfaces. The first application of friction by humans can be traced back to 400,000 years ago; our hominid ancestors in Algeria, China, and Java made use of friction when they chipped stone tools [7]. However, the first recorded systematic study in tribology dates back merely 500 years and is credited to Leonardo da Vinci, who not only conducted experimental research on friction but also developed bearing materials, investigated wear, and proposed ingenious schemes for rolling-element bearings [8]. Over the next 300 years, Guillaume Amontons, Charles-Augustin de Coulomb, and others revealed that the friction coefficient, usually denoted by μ, is typically not only independent of the normal force F_z, but also nearly independent of sliding speed, contact area, and surface roughness [7,9]. The empirical friction law (F_x is the friction force):

$$\mu = \frac{F_x}{F_z} \qquad (2.1)$$

Since the 20th century, the focus of tribological research has been on understanding the physical mechanisms behind tribology to provide a theoretical basis for controlling friction behavior. Numerous studies have shown that at the microscale, the actual contact area between surfaces is only a small fraction of the apparent contact area [10–12], as shown in Figure 2.1. This actual contact area, caused by surface roughness, increases with increasing pressure [13,14]. The real contact area between two interacting surfaces in contact is typically the source of friction and can be accompanied by wear. The initial wear induced by the real contact area can be assessed by examining variations in surface topography [15,16].
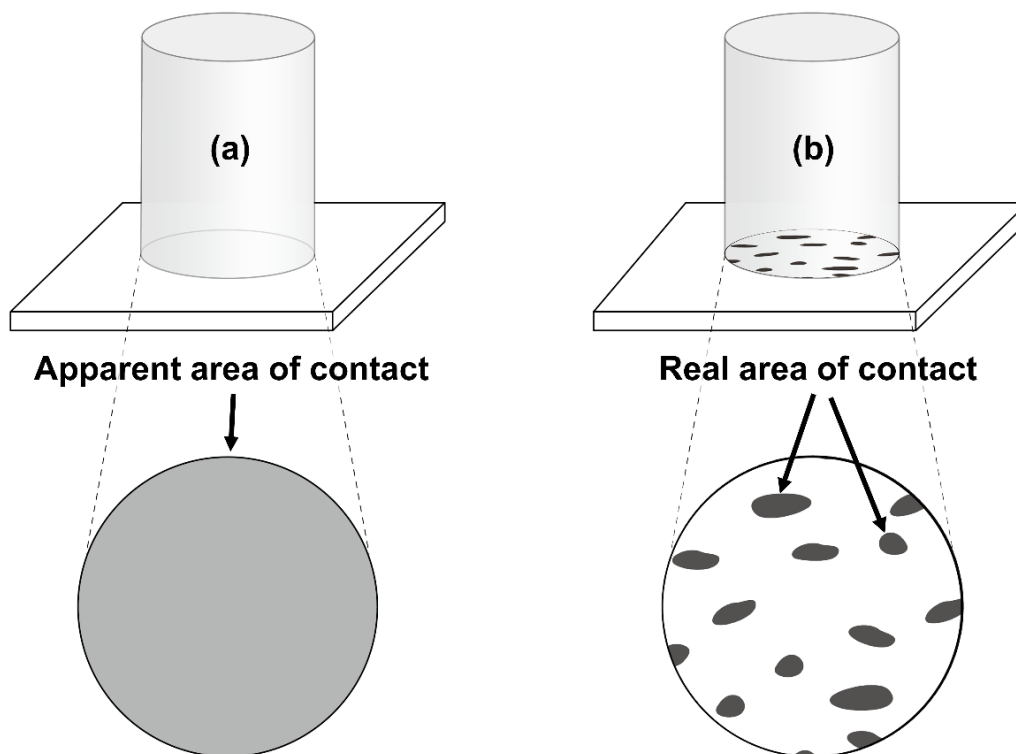
Figure 2.1: (a) The apparent area of contact that one might assume, normally calculated by looking at the visible geometry of the surfaces, without taking into account the roughness and irregularities at the microscopic level; (b) the real area of contact, which refers to the actual physical area where two surfaces are touching each other.

2.1.2   Lubrication

Lubrication, the process of utilizing a substance to decrease friction and minimize wear between two surfaces that come into contact, has been used since at least 1400 B.C. [7]. The ancient Egyptians, for example, lubricated their chariot axles using animal fats (tallow). The mechanisms of lubrication involve the formation of a thin film of lubricant between the two surfaces, which separates them and reduces the real contact area and the friction coefficient. This film of lubricant is able to withstand the normal load and shear forces acting on the surfaces, and it also provides protection against corrosion and oxidation [17]. The lubrication of a tribological system typically has several distinct states, as shown in Figure 2.2, including boundary lubrication, mixed lubrication, elasto-hydrodynamic lubrication, and hydrodynamic lubrication. The classification system for these friction regimes was developed by Richard Stribeck in 1902 [18], and the resulting curve is named in his honor. The Stribeck curve depicts the correlation between the friction coefficient and the dimensionless lubrication parameter known as the Hersey number. This parameter is defined as:

$$Hersey\ number = \frac{\eta \cdot v}{N} \tag{2.2}$$

Here, η stands for the dynamic viscosity of the fluid, v for the sliding speed, and N is the specific load of the tribological contact.
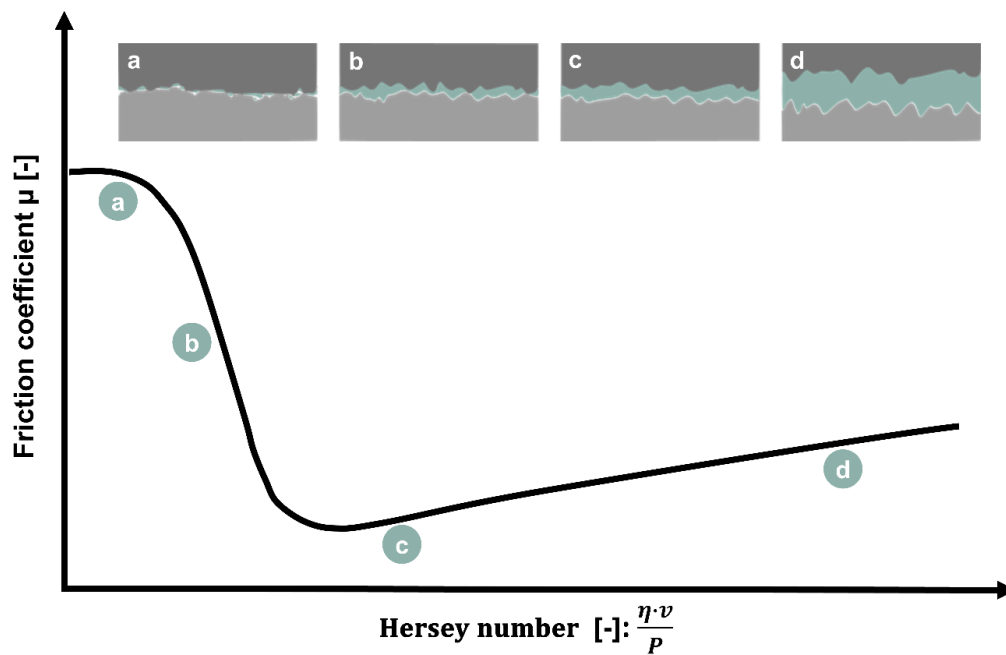
Figure 2.2: The Stribeck curve with classification into different friction regimes based on the specific lubricant film thickness and schematic representation of the respective contact conditions according to [9,19]: (a) boundary lubrication, (b) mixed lubrication, (c) elasto-hydrodynamic lubrication, (d) hydrodynamic lubrication.

Boundary lubrication occurs when the lubricating film is thin, the asperities of the surfaces are in direct contact or only separated from each other by a thin, molecularly adsorbed layer of an intermediate or surrounding medium (Figure 2.2a). This always results in high friction coefficient and wear rates. To minimize energy and material losses in lubricated tribological systems, the goal is to maintain a stable lubricating gap between the two surfaces, as shown in Figure 2.2c,d. These states, where forces are transmitted entirely via a liquid intermediate medium, are referred to as hydrodynamic lubrication (Figure 2.2d) or, if surfaces are elastically deformed due to hydrodynamic pressure, as elastohydrodynamic lubrication (Figure 2.2c). Figure 2.2b shows the transition area between boundary and hydrodynamic regimes, called mixed lubrication, where elastohydrodynamic lubrication and solid contact occur in this regime.

In addition to its primary function of reducing friction by separating contacting surfaces, lubrication can also serve as a means of dissipating heat generated by friction [20] and safeguarding surfaces against the detrimental effects of wear and corrosion [21]. The selection of an appropriate lubricant for a particular application is contingent upon several factors, including the operating conditions and requirements [22]. A range of lubricants is available, comprising oils, greases, and solid lubricants like graphite and molybdenum disulfide.

2.1.3   Wear

Wear, defined by the German Institute for Standardization (DIN 53020 [23]) as the progressive loss of substance from the operating surface of a body occurring as a result of relative motion of the surface, has been intertwined with the development of human civilization since the use of simple stone tools during the Stone Age. For over three million years, wear has been a significant contributor to the failure of tools in human history. Despite extensive efforts to regulate tribology behavior, such as utilizing the Striebeck curve to control the contact gap as described in the previous section, wear remains an intrinsic and persistent phenomenon.

In engineering and materials science, wear mechanisms can be determined by characterizing the removal of a material's surface caused by friction, impact, or other deleterious force. According to DIN 50320 [23], four basic wear mechanisms or any combination of them are involved in the wear process [16]:

- Abrasive wear: the displacement of material caused by the presence of hard particles between contact surfaces.
- Adhesive wear: formation and breaking of interfacial adhesive bonds, resulting in the transfer of material from one surface to the other.

- Surface fatigue: the surface damage of the material takes place due to cycles of stress and deformation and causes cracks and fractures in the surface or subsurface of materials

- Tribochemical reaction: formation of the chemical reaction between the elements of a tribosystem initiated by tribological stresses.

Among all kinds of wear, abrasive wear alone has been estimated to cost 1-4% of the gross national product of industrialized nations [24]. Especially for the industries with dusty environments, several studies affirm 50% of wear problems were the substantial impact of abrasives [16,25,26]. Although researchers have produced sophisticated designs in lubrication, sealing, filtration, and other related fields, abrasive wear is still a vexing problem in practice. Aside from substantial carbon dioxide emissions due to high friction and wear, remanufacturing and replacing worn-out parts incur high economic losses and energy consumption [27–30].

2.2 Abrasive Wear

Abrasive wear is the displacement of material caused by the presence of hard particles, of hard particles between or embedded in one or both of the two surfaces in relative motion, or by the presence of hard protuberances on one or both of the relatively moving surfaces [31], as shown in Figure 2.3. Hard particles can arise from various sources, including processed materials such as silica, alumina, as well as work-hardened wear fragments. Additionally, the adventitious entry of hard particles, such as dirt from outside the tribosystem, can also contribute to abrasive particl presence. If the hardness of the normal machined surfaces is much harder than the opposing surface, the protrusions on the surface, or asperities, can also work as "hard particles".
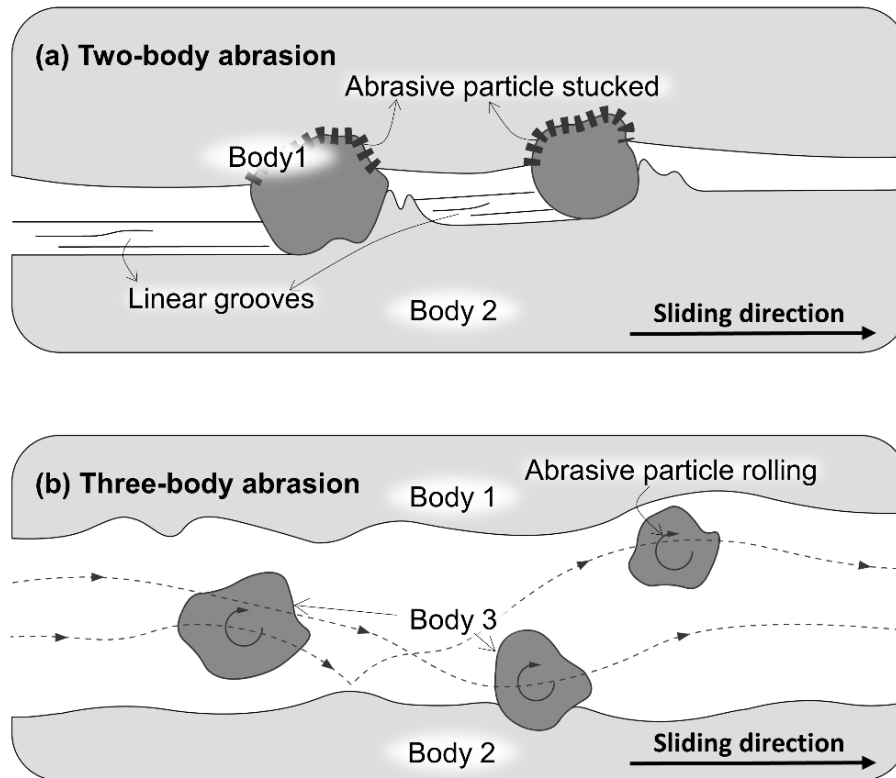
Figure 2.3: Abrasive wear process : (a) two-body abrasion denotes wear by "stuck" particles in one surface and sliding against the surface of a counter body; (b) three-body abrasion means wear is generated by free-rolling particles between interacting surfaces.

To accurately describe the acting mechanisms, abrasive wear can be classified into two-body abrasion and three-body abrasion [32,33]. Two-body abrasion denotes wear by "stuck" particles in one surface and sliding against the surface of a counter body (Figure 2.3a). The particles can cut and plough the counter body's surface during sliding. Three-body abrasion means wear is generated by free-rolling particles between interacting surfaces (Figure 2.3b).

The appearance of worn surfaces in a tribosystem can indicate which wear mechanism was acting. The two different abrasive wear mechanisms, two-body abrasion and three-body abrasion, would indeed cause distinct types of wear surfaces. The dominant mechanism in Figure 2.4a is a three-body process in which the abrasive particles do not embed but roll between the two surfaces, producing a heavily deformed and multiply indented wear surface

with no evident surface directionality [34,35]. In the case of two-body abrasion, as shown in

Figure 2.4. The particles embedded in one surface would cause a series of fine parallel grooves

in the counter surface.
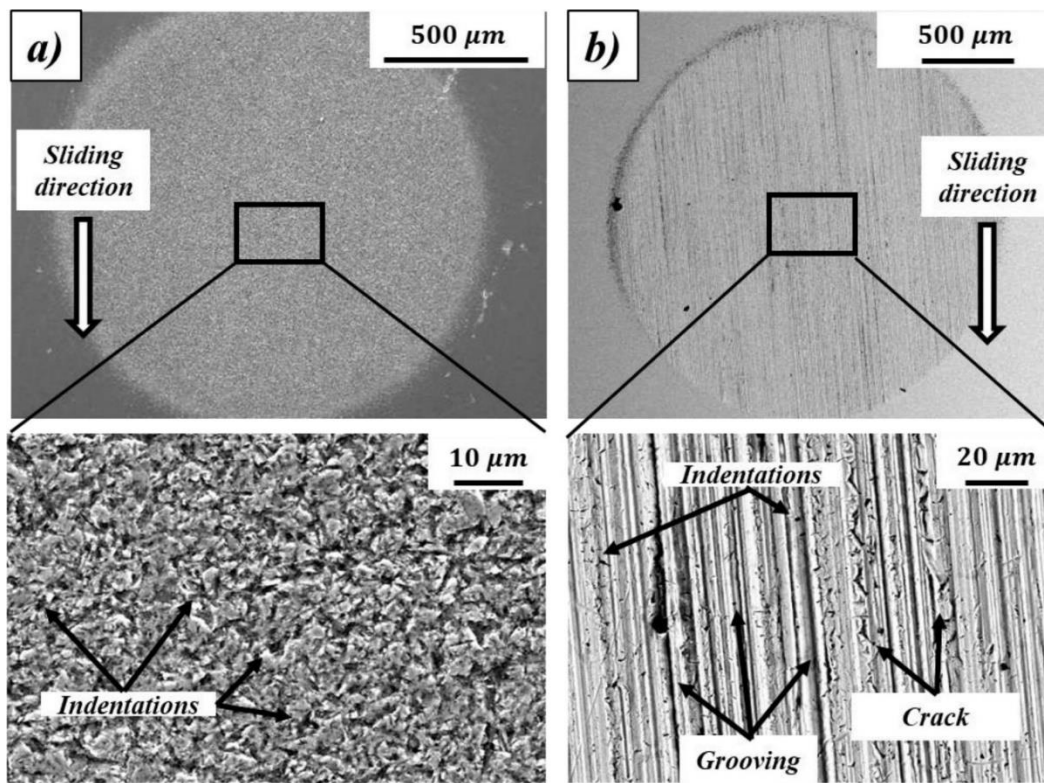
Figure 2.4: SEM images illustrating worn surfaces from micro-abrasion wear scars with
            diverse wear mechanisms [35]: (a) two-body abrasive wear tends to mainly produce
            micro-indentations and micro-cracking on the wear scar; (b) Three-body abrasive
            wear predominantly induces grooving on the wear scar, accompanied by some
            indentations and cracking.

Commonly it is assumed that the wear rates caused by two-body abrasion are higher than those

caused by three-body abrasion because particles are continually cutting and ploughing during

two-body abrasion [16,36–38], while particles are assumed to be rolling most of the time during

three-body abrasion. Additionally, as shown in Figure 2.5, it is generally believed that the wear

rate increases with an increasing particle size. With different experimental conditions and

materials, abrasive particles can generate wear through cutting, ploughing, fatigue, and cracking.
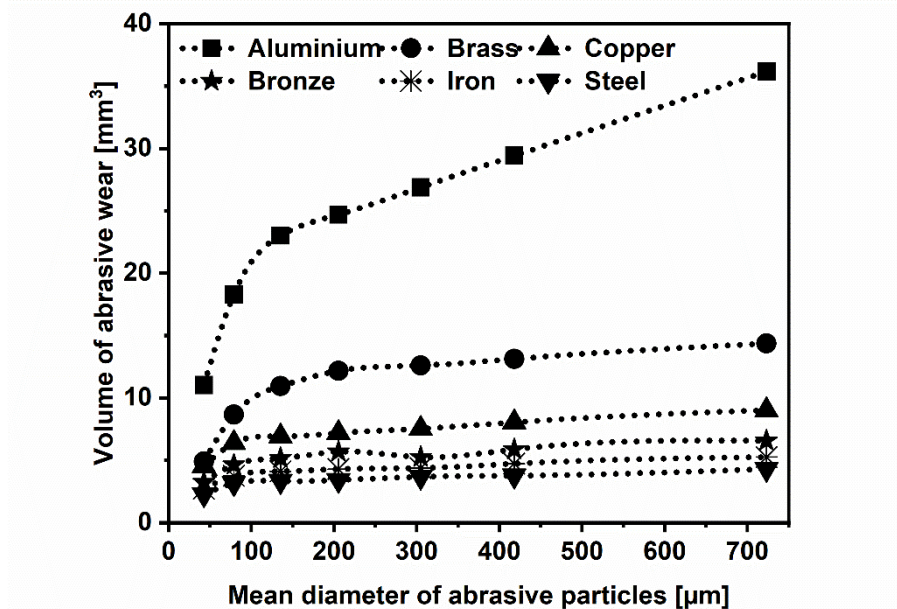
Figure 2.5: The relationship between the volume of abrasive wear and the mean diameter of abrasive particles [38]. The wear of Aluminium, brass, bronze, iron, and steel were tested at a load of 20 N, a sliding distance of 6 m, and a velocity of 0.5 m/s.

Misra and Finnie studied the tribological performance of two-body and three-body abrasion under dry conditions. In their research, two-body abrasion was found to be about nine to twelve times as effective in removing material than three-body abrasion [39–42]. Williams and Hyncica revealed the mechanism of abrasive wear in lubricated contacts using a model based on the particle dimension d and film thickness h, as shown in Figure 2.6. Beyond a critical ratio (d/h), the wear mechanism was reported to change from three-body abrasion to two-body abrasion, and wear also increased with d/h [43,44]. Wear mechanisms and wear performance were also found to be linked to further parameters, such as abrasive size [45,46], abrasive type [28], abrasive concentration [47], speed [48,49], or load [50,51].
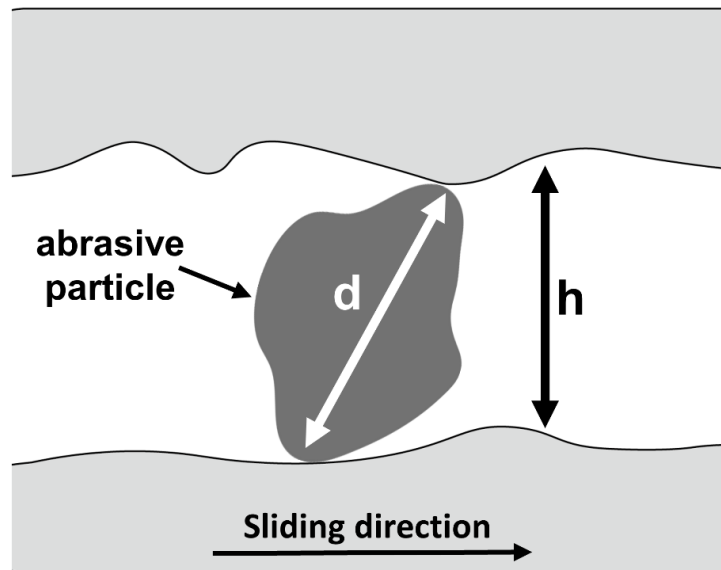
Figure 2.6: A single abrasive particle is described by parameter *d*; *h* is the gap between the surfaces; the lower surface moves from left to right.

Considering the above, efforts have been made to mitigate the abrasive wear performance of tribological systems. Xiao et al. investigated the effects of two additives (polystyrene and silicon nitride) on the tribological performance of water-based slurries with silicon dioxide or alumina abrasives [52]. Polystyrene reduced wear but increased friction, while silicon nitride showed a positive effect on both abrasion resistance and friction reduction. Da Silva et al. studied micro-textured tools in machining and micro-abrasion tests [53]. Texturing increased the tool life in the machining tests but resulted in a pronounced increase in the coating wear rates in the micro-abrasion experiments. In addition to these attempts, coatings [54] and new materials [55] were also investigated as strategies for friction and wear reduction on abrasive wear. However, only limited research [56,57] associates lubricated abrasive wear with hydrodynamic effects along the Stribeck curve [18], causing a lack of experimental support on the Stribeck curve's applicability for lubricated abrasive wear. The Stribeck curve visualizes how friction in a system may change due to a hydrodynamically induced fluid film that can separate contacting asperities and partially carry the applied normal load (as shown in Figure

2.2), which is a conventional approach to suppress wear under normal lubrication [56,58–61]. However, how an increasing fluid film thickness influences lubricated abrasive wear remains unclear.

In addition to the occurrence of high friction build-up and significant wear, abrasive wear also exhibits a noteworthy characteristic, that is, large frictional fluctuations [2–4,62,63]. An example is presented in Figure 2.7 from Ma's [63] study, where the evolution of the friction coefficient of TiN coating is depicted under a normal load of 200 N. As shown in Figure 2.7, after point 2, a considerable amount of abrasive particles was generated from hard TiN debris, which significantly increased the friction coefficient and accelerated the coating's wear. Notably, the occurrence of abrasive wear was also associated with a pronounced increase in frictional fluctuations. However, the cause of fluctuating friction in abrasive wear has not yet been understood, even if frictional fluctuations are an ubiquitous manifestation of abrasive wear.
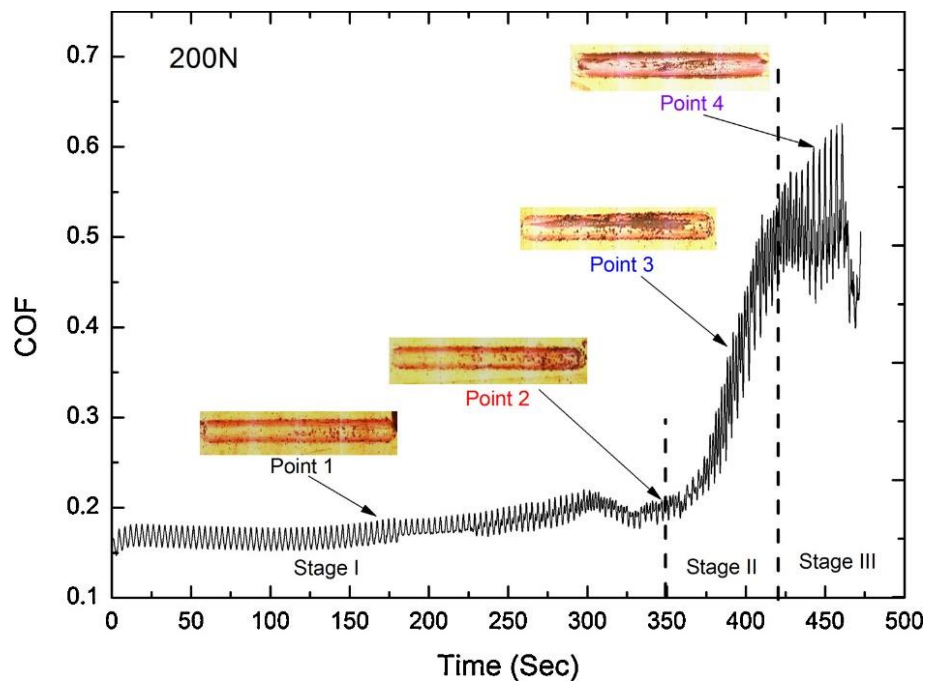
Figure 2.7: Friction coefficient evolution of TiN coating under load of 200 N; in stage I, the friction coefficient remained low and consistent; in stage II (after 350 s), due to the emerges of the thrid body abrasive particle the friction coefficient started to rise rapidly from 0.2 to 0.55; in stage III, the friction coefficient reached a plateau after the TiN coating has been partly removed [63].

2.3 Surface Topography and Oscillation of Contacting Surfaces

The goal of being able to predict friction and wear has been a long-cherished wish for the entire tribology community; however, a comprehensive prediction and control of tribological properties has yet to be fully achieved after more than 100 years of effort. The challenge is due to the complexity of a tribological system, which is influenced by a range of factors, including the microstructure of the materials [64,65], the asperities of the contact surfaces [66,67], and the surrounding environment [68,69]. The situation becomes even more complicated if abrasive wear occurs. In this section, we will introduce certain factors like surface topography and oscillation (due to disk mounting tilt), which are frequently overlooked or insufficiently addressed and that might impact tribological performance.

2.3.1   Surface Topography

A surface, which may appear uniform in most tribological experiments, is actually a planar defect that contains inhomogeneities. Even smooth surfaces, polished to a mirror finish, exhibit microscopic roughness and irregularities in the form of sharp, rough, or rugged projections known as "asperities" (from the Latin asper, which means "rough"). These surface asperities exist across multiple scales and exhibit self-affine or fractal geometries. The arbitrarily complex shape of the boundary between a material and the outside world plays a key role in determining the tribological properties of the surface [66,70,71].

For a typical surface, the irregularities are characterized as mean roughness and waviness parameters, which are considered simple scalar quantities (e.g., roughness R_a and waviness W_t in ISO 4287). These roughness and waviness parameters are not directly evaluated from the primary surface profile but generated from corresponding roughness and waviness profiles after filtering the primary profile in accordance with current standards (e.g., ISO 116610 or ASME B46.1), as shown in Figure 2.8a. Roughness refers to the small, finely-spaced irregularities that can be seen on a surface at a microscopic level. These irregularities are typically caused by the manufacturing process and can include things like scratches, pits, and other imperfections. Waviness, on the other hand, refers to the larger, widely-spaced irregularities that can be seen on a surface at a macroscopic level. Waviness is often caused by factors such as machining or assembly and can include things like undulations, bumps, and other larger surface features. [72]
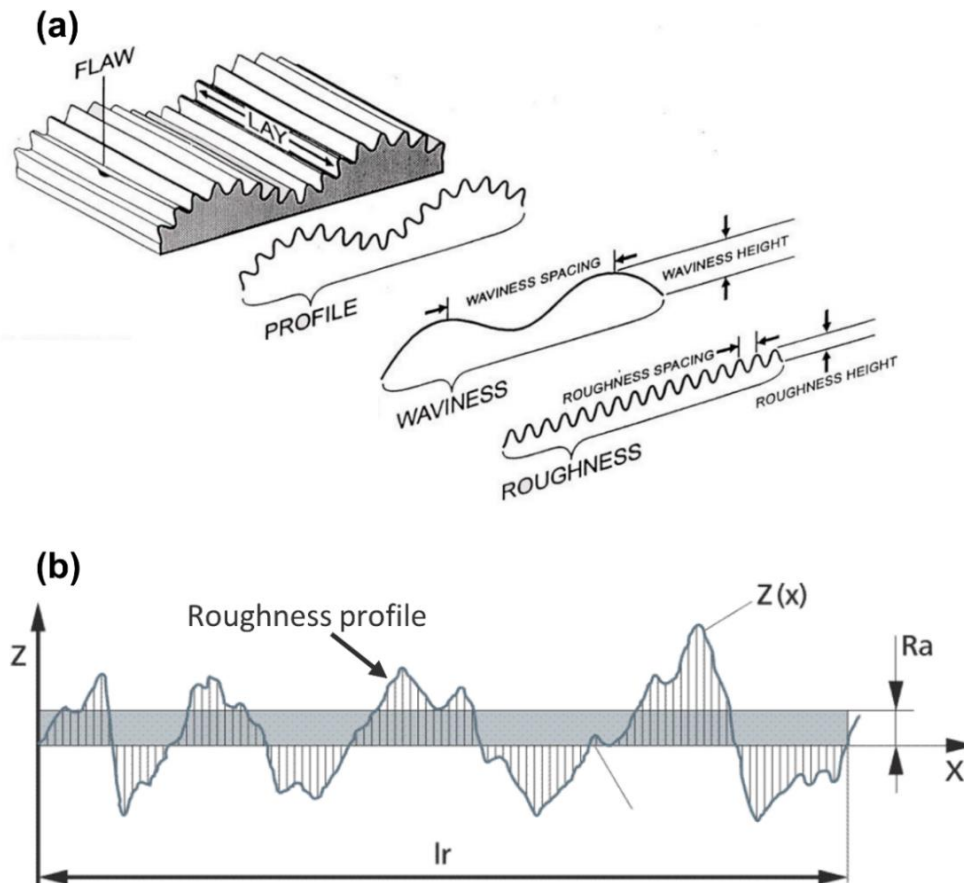
Figure 2.8: (a) Roughness and waviness on a surface [73]; (b) Schematic of arithmetical mean
deviation of roughness profile (R_a); *lr* is the length of the roughness profile, and
Z(x) is the profile height function [74].

Figure 2.8b gives an example of roughness quantities evaluation. The arithmetical mean

deviation of the roughness profile noted as R_a is evaluated by measuring the average distance

between the roughness profile and its mean line within the evaluation length. Where *lr* is the

length of the roughness profile, and *Z(x)* is the profile height function. Roughness R_a is defined

as:

$$R_a = \frac{1}{lr} \int_0^{lr} |Z(x)| dx \qquad (2.3)$$

However, the actual surface topography is far more complex than can be described by a few scalar parameters. To obtain more accurate roughness indicators that can fully characterize surface topography across different length scales, the surface roughness power spectral density (PSD) has been employed [75,76]. The PSD of a surface is a mathematical tool that decomposes a surface into its contributions from various spatial frequencies (wave vectors). Mathematically, the PSD represents the Fourier transform of the signal's autocorrelation function, which includes only the power component (excluding phase) [77–79]. As shown in Figure 2.9 [80], an attempt has been made to develop a single function that comprehensively describes surface topography by taking an arithmetic average of 127 measurements obtained from three different instruments: stylus profilometry, atomic force microscopy (AFM), and transmission electron microscopy (TEM), across more than 30 magnifications. Despite its usefulness in the academia, power spectral density (PSD) is not commonly utilized in most surface finishing processes as a means of characterizing surface topography with quantitative indicators. Even in the academia, it is more common to use quantitative indicators that describe surface topography rather than utilizing the PSD.
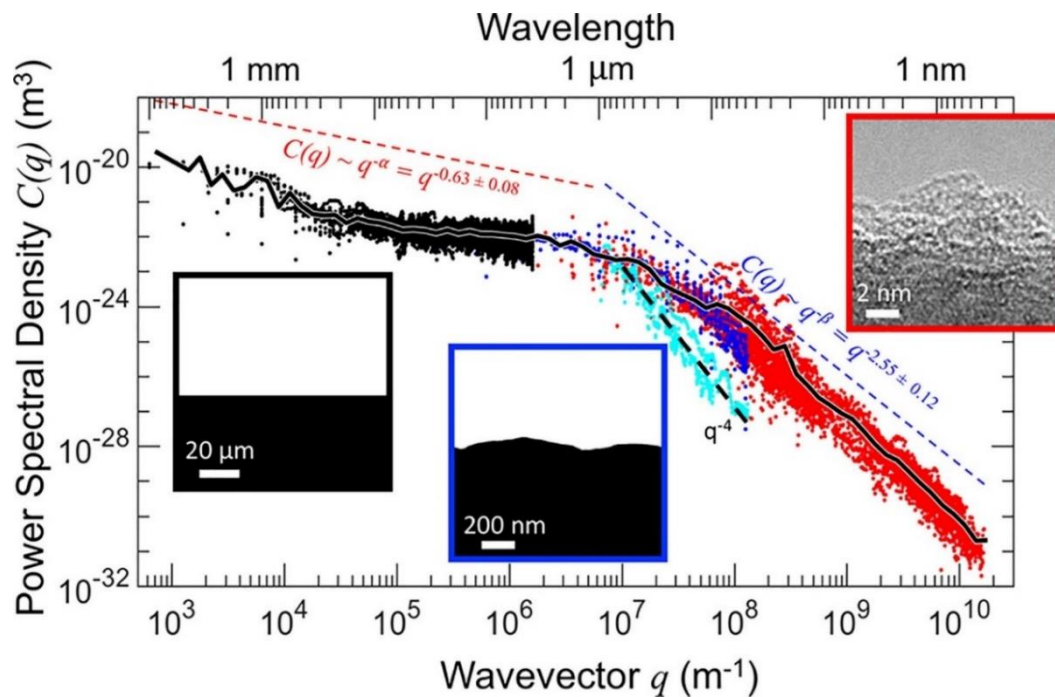
Figure 2.9: Topography of 127 measurements, taken at more than 30 different magnifications and using three different instruments, are combined into a single description of the surface [80]. The reliable portions of line scan measurements from stylus (black), AFM (blue), and TEM (red) are shown as points. The individual measurements are combined into a single PSD (black line with white outline).

The impact of roughness parameters on friction and wear has been thoroughly explored in the literature, showing varied correlations – positive, negative, or non-monotonic. For instance, Al-Samarai et al. [81] discovered that under dry conditions, friction and wear increase with an increase in surface roughness. However, Kubiak et al. observed that carbon steel (AISI 1034) and titanium alloy (Ti-6Al-4Vr) have a lower friction coefficient for rough surfaces in a fretting wear device[82]. Shi et al.'s experiments revealed a non-monotonic correlation between roughness and friction coefficient, where an increase in surface height arithmetic mean S_a (ISO 25178) showed a decreasing trend followed by an increasing trend in friction coefficient [83]. Additionally, Liang et al. [84] observed drastic fluctuations in friction coefficient with the increase of R_a (average surface roughness).

Due to the use of different cut-off lengths for filtering the surface features of interest, surface roughness measurements commonly obscure the waviness portion of the surface profile [85]. Chang et al. [86] found that the waviness W_a (arithmetic average of surface heights, but at higher wavelengths than simple roughness) strongly correlates with friction between Neolite rubber and quarry tiles. Wang et al. [87] discussed the effects of multiscale waviness on the full-film elastohydrodynamic (EHL) performance, finding that the amplitude and frequency are associated with the central film thickness and the Hertzian contact radius of the corresponding smooth EHL problems, respectively.

Although extensive research has been conducted on surface topography, achieving a completely flat surface or repeating the same surface remains elusive. **Consequently, every tribological experiment is carried out on a different surface, even if they are deemed similar by certain parameters (such as R_a).** On the one hand, the minor surface deviations in experimental conditions might govern tribological behavior to an as of yet unknown and surprisingly large amount. On the other hand, the enigmatic impact of minor surface deviations on tribological behavior may contribute to elucidating unresolved open questions in the community (for example, the issues of abrasive wear mentioned in chapter 2.2).

2.3.2   Oscillation of the Contacting Surfaces

Apart from the intricate surface topography, there are other inevitable deviations present in any experiment that sually are minimized during experimental preparation but cannot completely be eliminated – oscillation of the contacting surfaces due to sample mounting tilt. Once the movement of surface initiates, sample mounting tilt will cause periodic oscillations of the contacting surfaces in the normal direction.

The experimental investigations into the impact of oscillation on tribological behavior commenced in the late 1950s [88], and the practical significance of the effects of oscillations on tribological performance is profound. Previous research has demonstrated that ultrasonic vibrations can enhance productivity, resulting in time savings of approximately 5–10% during machining, along with cost savings of about 30%. These improvements can be attributed to decreased interfacial friction and the continuous removal of debris through the application of ultrasonic vibrations during machining processes [89–91]. The utilization of oscillations can also be observed in wire drawing [92,93], press forming [94], and several others.

Socoliuc et al. [95] elegantly demonstrated achieving mechanical resonance by adjusting the oscillation frequency of on an atomic force microscope (AFM). Their experimental set-up, illustrated in Figure 2.10 [96], involves the addition of a small oscillatory force to the normal force by means of an external electrostatic potential applied between the cantilever and the sample. By modulating the oscillatory force at a frequency equivalent to one of the vertical resonance frequencies of the tip-sample contact, the stick-slip motion of the cantilever and, consequently, friction itself could be reliably switched on or off.
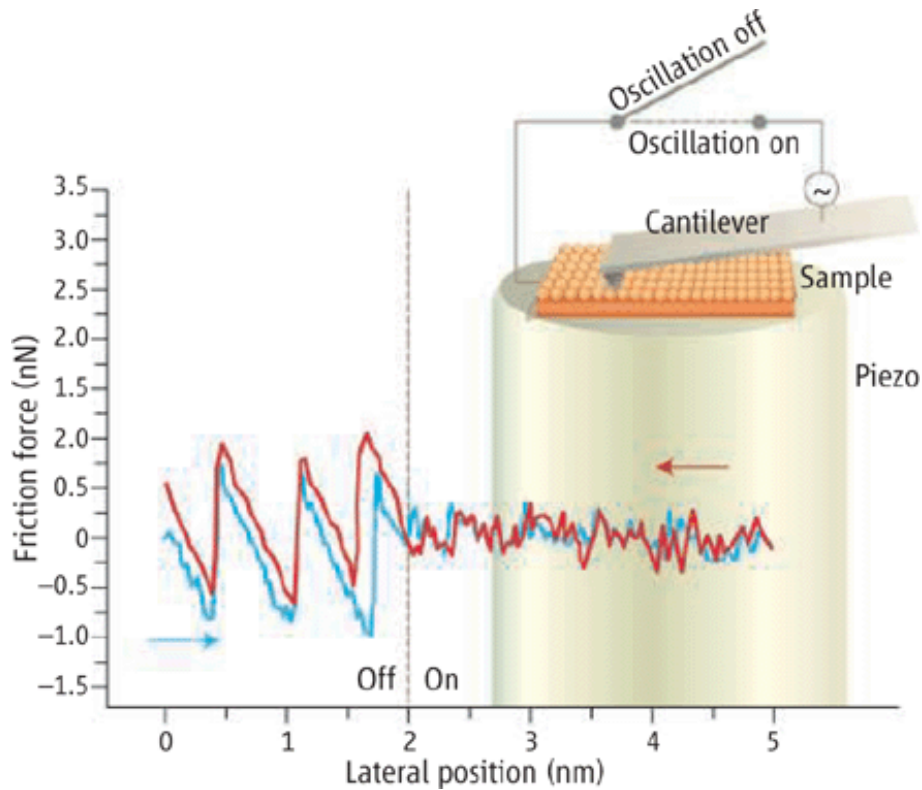
Figure 2.10: Reducing friction with oscillation [96]. With an atomic force microscope (AFM), Socoliuc et al. [95] have demonstrated that the stick-slip phenomenon can be eliminated by slightly modulating the appropriate frequency to the external loading force acting on the cantilever.

Chowdhury et al. [97] investigated the impact of oscillation amplitude on the friction coefficient at a macro scale for various materials, including glass fiber-reinforced plastic, cloth-reinforced ebonite, polytetrafluoroethylene, rubber, and mild steel. The authors employed a pin-on-disk apparatus that generated oscillations in the normal direction on the pin at different amplitudes. The results indicated that the friction coefficient decreases as the oscillation amplitude increases. As shown in Figure 2.11, the reduction of friction coefficient can be up to around 60% when a 200 µm oscillation amplitude is applied to a mild steel pin against a mild steel disk.
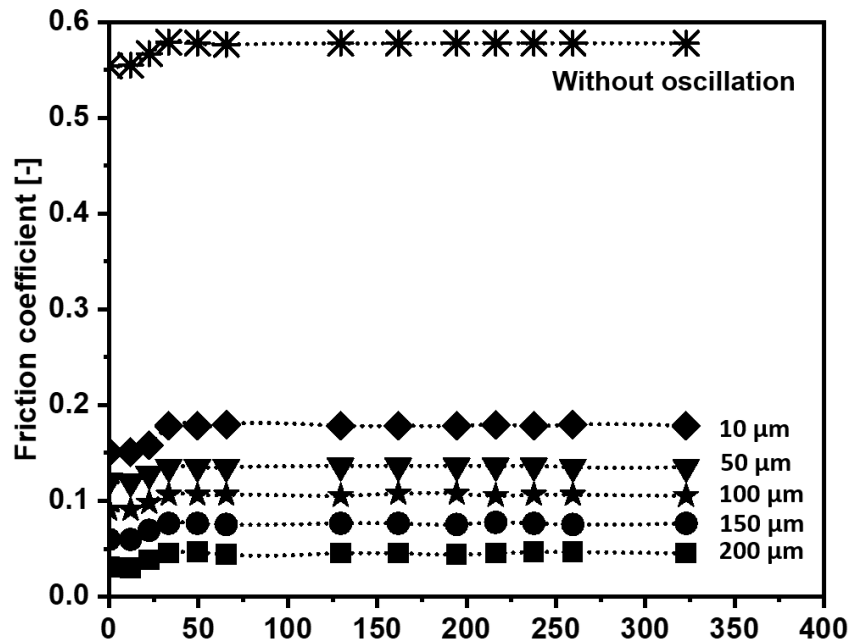
Figure 2.11: The friction coefficient of a 6 mm diameter cylindrical mild steel pin against a mild steel disk was investigated with the variation of testing time at different oscillation amplitudes, maintaining a sliding velocity of 0.785 m/s, normal load of 10 N, frequency of oscillation of 500 Hz, roughness of 1.20 μm (RMS, root mean square of roughness profile), and relative humidity of 50% [97].

These experimental investigations have established an empirical foundation for qualitatively comprehending the impact of oscillations on friction. However, achieving a satisfactory quantitative agreement between experimental findings and theoretical models has not been reached [98], casting doubt on our grasp of the underlying physics of this phenomenon. The issue of which oscillation properties contribute to the decrease of the frictional force is still the subject of debate: Whereas in the case of static friction, the amplitude of displacement oscillation appears to be the critical factor [99], for sliding friction, it seems also related to the sliding velocity, the surface roughness, and the normal load under oscillation conditions [97,100,101].

One of the few theoretical models for the sliding friction under normal oscillation was developed by Popov et al. [101,102]; they begin by looking at the system as a single Hookean

22

spring that has an associated lateral stiffness k_x and normal stiffness k_z, as shown in Figure 2.12. They assume that Coulomb's law of friction (with a constant friction coefficient μ_0 that is the same for both static and sliding friction) holds at the contact point. With the substrate moving beneath a flat plane at a constant velocity of v, the contact spring is dragged along. The lateral displacement u_x is the only unknown variable, which depends on the current state of the system with respect to its initial position. The normal displacement, u_z, of the spring is assessed with respect to its state of initial unstressed contact with the substrate. The externally applied oscillation is explicitly defined by u_z, which is parameterized as follows [101]:

$$u_z(t) = u_{zm} + A_z w(ft) \tag{2.3}$$

Here, u_{zm} is the average value of oscillation. A_z represents the amplitude, and f represents the frequency of the oscillation. $w(ft)$ is a dimensionless function describing the "shape" of the oscillation. The waveform, w, is normalized such that it has a period of 1, a minimum value of -1, and a mean value of 0.
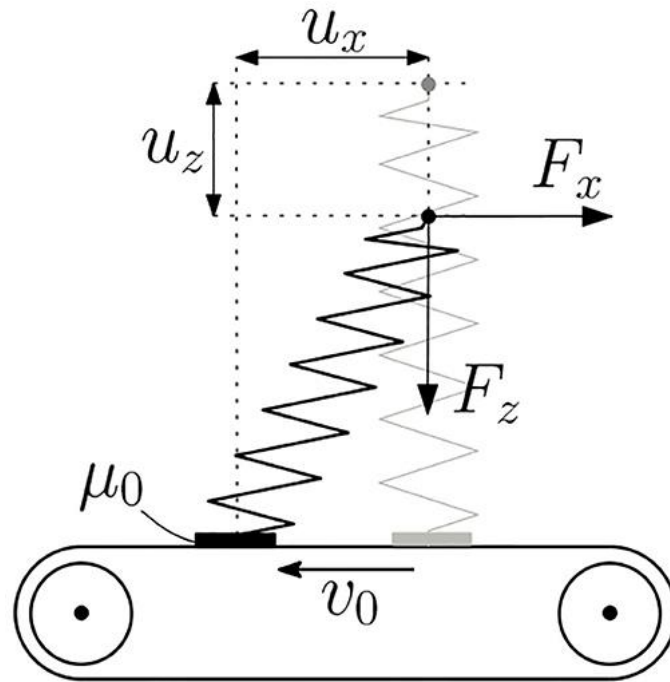
Figure 2.12: A single massless spring is employed as a minimal model for a tribological sliding interaction. The sliding velocity remains consistent; the contact is modeled as a single Hookean spring that has an associated normal stiffness k_z and a lateral stiffness k_x. Amontons friction with the constant coefficient of friction μ_0 is assumed in the contact point [101].

In Popov's model, for small oscillation amplitudes, the surfaces remain in contact at all times since the difference in displacement Δu_z is less than the initial displacement $u_{z,0}$. The frictional contact between the horizontal surfaces is mainly controlled by a stick-slip behavior, with the lower point of the spring being in either stick or slip state. During pure sliding, the tangential friction force F_x is always equal to $\mu_0 F_z$, which is equivalent to $k_x u_x(t) = \mu_0 k_z u_z(t)$ (as shown in Figure 2.13).
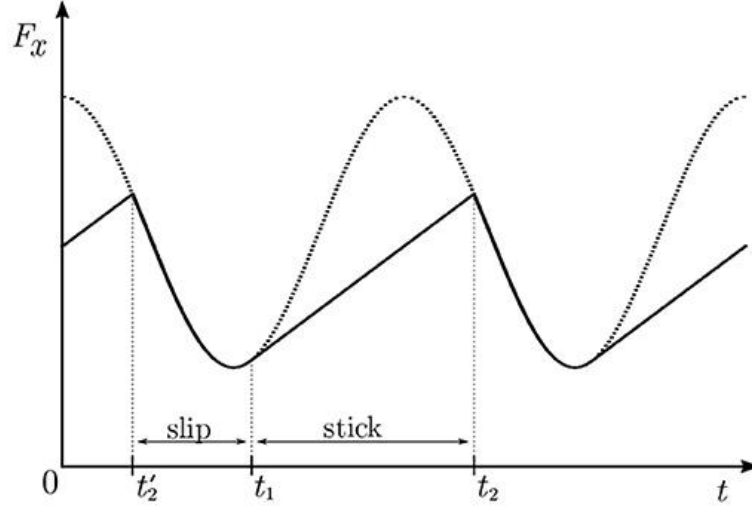
Figure 2.13: Schematic presentation of stick and slip under a harmonic oscillation. The doted line on the graph shows the tangential force that would occur in the absence of stick-slip behavior (i.e., during pure slip), where F_{slip} is equal to $\mu_0 F_z(t)$. In contrast, the solid line shows the actual tangential force under the influence of stick-slip. The stick phases are indicated by straight line segments (e.g., between t_1 and t_2), while the slip phases are represented by sinusoidal segments (e.g., between t'_2 and t_1).

After substituting the displacement u_z from equation (2.3) and rearranging, the lateral displacement and the velocity of the contact point can be calculated:

$$u_x(t) = \mu_0 \frac{k_z}{k_x}(u_{zm} + A_z w(ft)) \tag{2.4}$$

$$u'_x(t) = \mu_0 \frac{k_z}{k_x} A_z w'(ft) \tag{2.5}$$

The transition from slip to stick occurs when the relative motion between the substrate and the contact point reaches zero, as indicated by $u'_x(t) = v_0$. Once stick-slip behavior is initiated, the contact point is dragged along by the substrate at a constant velocity v_0, resulting in a linear increase in both the tangential displacement and force over time:

$$F_{stick}(t) = \mu_0 F_z(t_1) + k_x v_0(t - t_1) \tag{2.6}$$

As depicted in Figure 2.13, the stick phase terminates at time t_2 when the condition $F_{stick}(t_2) = \mu_0 F_z(t_2)$ is satisfied. During the stick phase, the average force and coefficient of friction are reduced compared to the pure slip phase.

2.4 A Summary of the Existing Literature and the Aim of this Thesis

Abrasive wear has been a focal point of research in tribology for several decades. As outlined in chapter 2.2, the research on abrasive wear includes the identification of the underlying mechanisms, the assessment of wear, and the development of abrasive models. Despite these efforts, many unresolved questions persist in abrasive wear:

- It remains unclear how an increasing fluid film thickness affects lubricated abrasive wear

- What factors contribute to large frictional fluctuations during abrasive wear, and whether these fluctuations influence wear?

- Is it possible to predict abrasive wear?

To address these unresolved issues in abrasive wear research, this thesis first aims to enhance the understanding of the mechanisms of abrasive wear by investigating the influence of fluid film thickness on lubricated abrasive wear. Then, the effects of surface topography and oscillation (due to disk mounting tilt) were investigated, commonly considered constant factors that do not affect performance. Finally, this thesis seeks to utilize the insights gained from investigating the effects of the waviness profile and contacting surfaces' oscillation to facilitate the prediction of abrasive wear.

3 Methodology

3.1 Materials and Sample Preparation

The tribological experiments in this thesis were carried out using a pin-on-disk configuration with pins and disks made from bearing steel (100Cr6, AISI 5210). The bearing steel disks, having a diameter of 70 mm, were purchased from Eisen Schmitt (Karlsruhe, Germany). They underwent a hardening and tempering process to reach a hardness of nominally 800 HV. All the disks were fine-ground on a cup grinding machine (G&N MPS 2 R300, Erlangen, Germany) with corundum grinding wheels of grit EK200, resulting in mean roughness values ranging from $R_a = 0.08$ to $0.12\,\mu m$ (measured by HOMMEL-ETAMIC T8000 R120-400 tactile surface profilometer, Villingen-Schwenningen, Germany). The radial height difference along the frictional track was below $2\,\mu m$ ($W_t \leq 2\,\mu m$, measured by FRT MicroProf MPR 1024, Chromatic white light (CWL) profilometry, Bergisch Gladbach, Germany), as shown in Figure 3.1. **Controlling the height difference of the 132 mm disk sliding track remains within 2 μm, representing the minimum achievable value in our laboratory.**

The pins were purchased in the form of 8 mm diameter spheres and then flatted to a circular area of 7.33 mm in diameter by grinding and polishing. They were purchased from KGM (Fulda, Germany) and employed in an as-received condition with a hardness of 700 HV. The flattened surfaces had roughness values ranging from $R_a = 0.02$ to $0.04\,\mu m$ and a flatness below $0.6\,\mu m$. All pins and disks were demagnetized and cleaned with isopropanol for 15 minutes in a sonicating process before the tribological experiments.
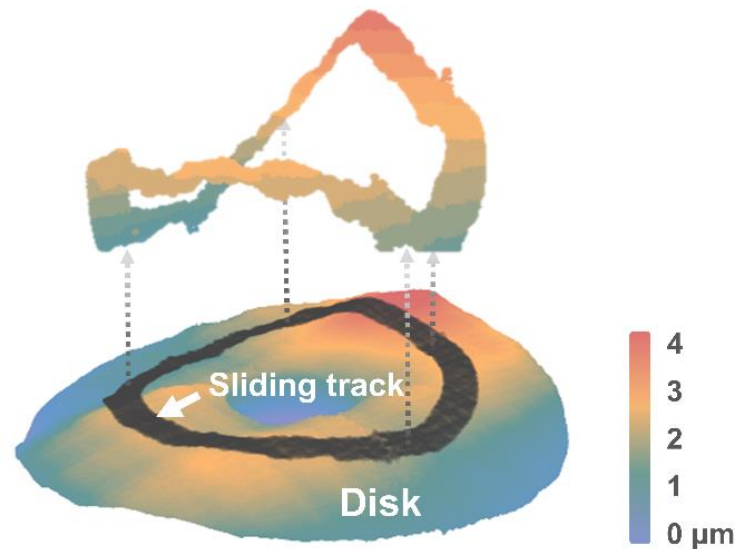
Figure 3.1: Extracting the surface profile of the 7.33 mm width sliding track from chromatic white light (CWL) profilometry data. In the pin-on-disk experiments within this thesis, the diameter of the disk is 70 mm, with a sliding radius of 21 mm and a pin diameter of 7.33 mm. Consequently, the extraction of the disk surface profile involves capturing a circular arc with a width of 7.33 mm at the disk's radius of 21 mm. The height difference of the 132 mm sliding track is below 2 µm. From [103] with permission.

In this thesis, three different interfacial media were utilized. For abrasive experiments, two kinds of water-based Al_2O_3 abrasive slurries with different particle sizes (5 µm and 13 µm, according to FEPA grains standard) were purchased from Joke (Lapping medium BIOLAM®, Bergisch Gladbach, Germany) with a nominal concentration of 12.5 wt.%. The size distribution of the particles in the slurries was measured by laser granulometry (CILAS 1064, Orléans, France), presented in Figure 3.2(a). Both slurries show a narrow, slightly bimodal particle size distribution. A SEM image of a dried slurry shown in Figure 3.2(b) confirms that no specific shape exists. The results for dynamic viscosity measurements are presented in Figure 3.2c. For lubricated experiments, FVA 1 (Klueber Lubrication, Munich, Germany) base oil was employed, with a kinematic viscosity ranging from 14.5 to 15.3 mm^2/s at 40 °C.
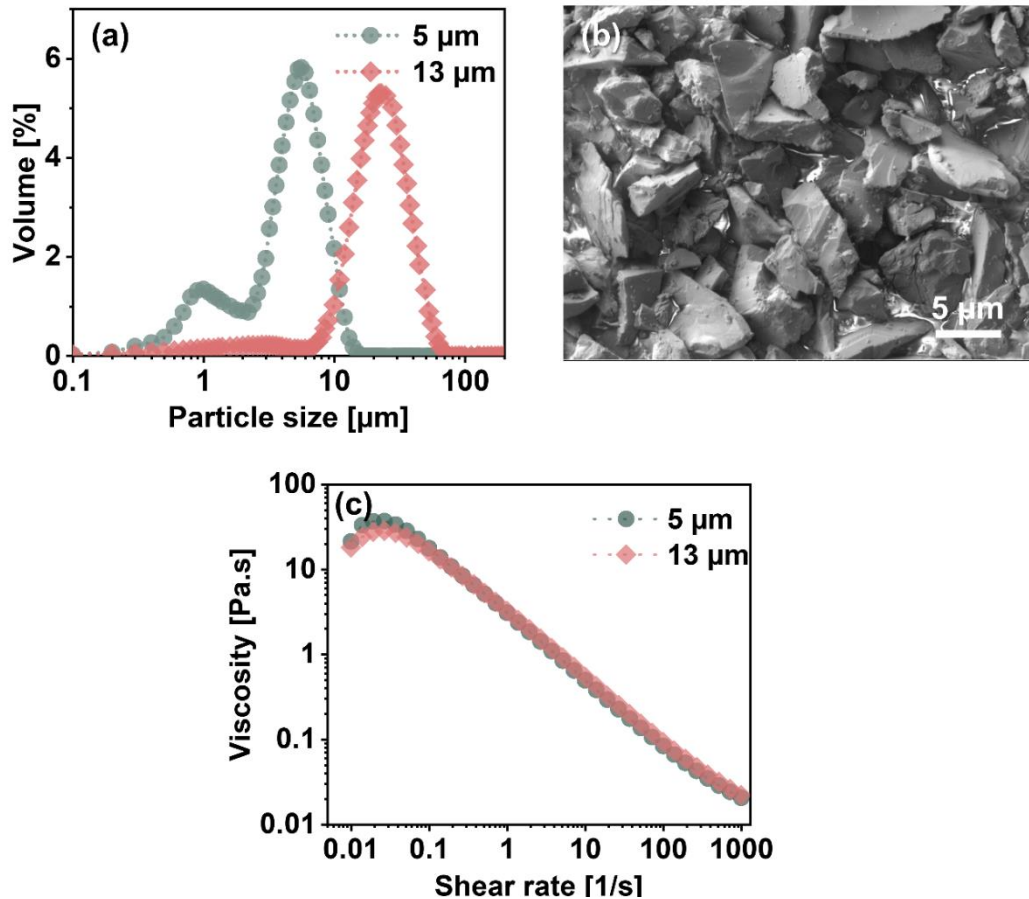
Figure 3.2: Characterization of particles in the slurry: (a) particle size distribution; the median particle size of the two Al_2O_3 slurry is 5 µm and 13 µm, respectively (b) SEM image of Al_2O_3 particles in the 5 µm slurry; (c) dynamic viscosity measurement of 5 µm slurry and 13 µm slurry.

3.2 Tribometer and Disk Mounting

The tribometer utilized in this thesis was a CSEM tribometer from CSM Instruments (located in Peseux, Switzerland, now owned by Anton Paar). To fulfill the requirements of our experiments, the CSEM tribometer was modified two-fold. The experiments in chapter 4.1 were done with CSEM Tribometer 1.0, whereas CSEM Tribometer 2.0 was used in chapter 4.2 and chapter 4.3.

3.2.1   CSEM Pin-on-Disk Tribometer 1.0

Before the tribological tests, as shown in Figure 3.3a, the disk was fixed and leveled by three screws on the disk cover with a hemispherical surface at the bottom. A lever gauge indicator with a scale value of 0.002 mm from Actorn (Ludwigsburg, Germany) was employed to minimize the tilt introduced during the mounting process. **Upon mounting the disk, the height difference along the disk's sliding track remained below 4 µm, representing nearly the lowest achievable value within our laboratory.**

During the tribological tests, a capacitive sensor (AW 210-52-1, E+H Metrology GmbH, Karlsruhe, Germany) was added on the top of the pin holder to measure the pins' movement in the vertical direction (in Figure 3.3b). All the capacitive sensors in the thesis were of the same model.
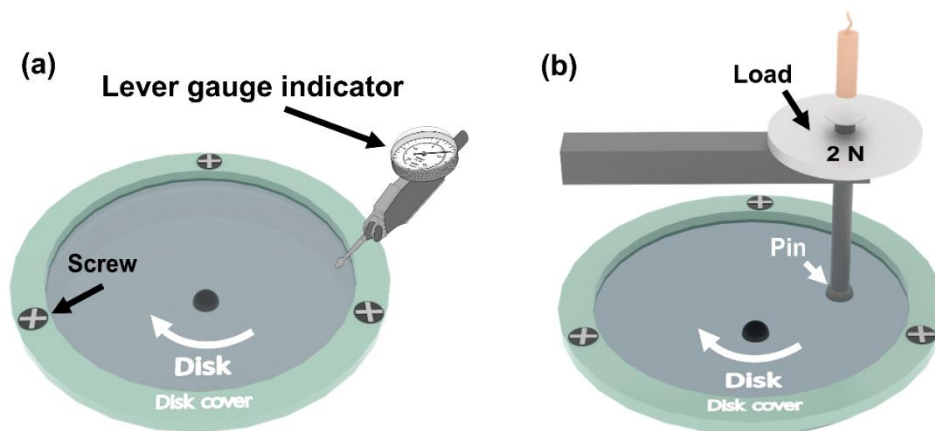
Figure 3.3: Schematic diagram of experimental setup on CSEM tribometer 1.0: (a) before the tribological test, a lever gauge indicator was employed to support the mounting process; (b) experimental setup of the pin-on-disk tribological test. The total height difference on the sliding track was below 4 µm.

3.2.2 CSEM Pin-on-Disk Tribometer 2.0

The CSEM tribometer 2.0 was custom modified by incorporating a capacitive sensor on the side and a metal block coaxially moving with the disk, which operates as a zero position trigger, allowing segmenting the data from each revolution of the disks, as shown in Figure 3.4. The zero position of every cycle was triggered when the metallic block moved over the capacitive sensor.

Before each tribological test, as shown in Figure 3.4a, the disk was fixed and leveled by three screws on the disk cover with a spherical surface at the bottom. **The total height difference on the sliding track was also strictly limited to a maximum of 4 µm (the lowest achievable value within our laboratory), as measured and recorded by a non-contact capacitive sensor located in the pre-contact area, as shown in Figure 3.4a**. The capacitive sensor was then moved to the top of the pin holder before the tribological test, as shown in Figure 3.4b.
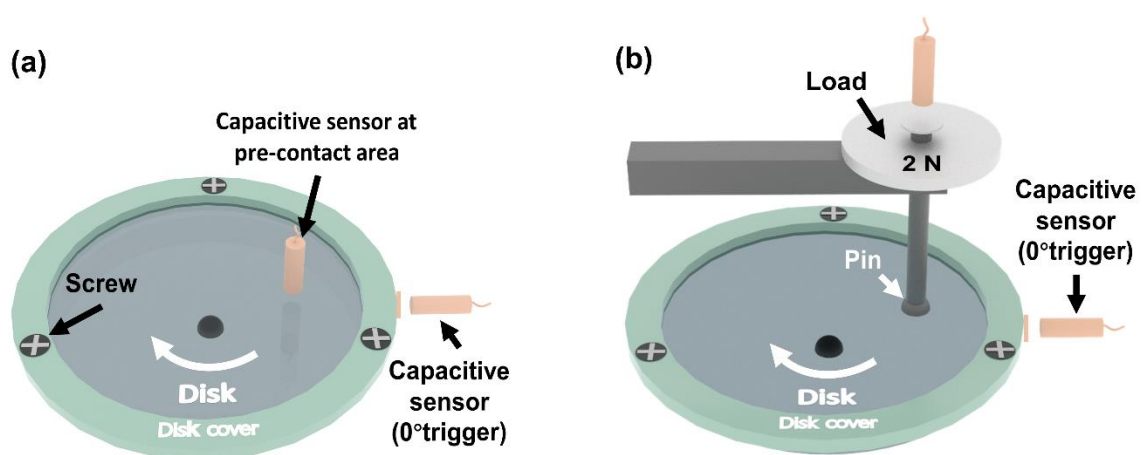
Figure 3.4: Schematic diagram of experimental setup on CSEM tribometer 2.0: (a) before the tribological test, the capacitive sensor records the height changes of the sliding track during rotation; the total height difference on the sliding track was strictly limited to a maximum of 4 µm; (b) experimental setup of the pin-on-disk tribological test.

3.3 Tribological Experiments

For all the experiments in this thesis, a normal force of 2 N was applied by dead weights to the pin. To limit the influence of a velocity gradient due to the large contact area [104], a mean sliding radius of 21 mm was selected. The friction force was determined by measuring the deflection of the elastic arm of the tribometer. In the following sections, the experimental details will be presented.

3.3.1   Investigating Tribological Mechanisms of Abrasive Wear

To investigate the tribological mechanisms of abrasive wear, tests were carried out on CSEM Tribometer 1.0 with a 1 Hz sampling rate. For each test, 100 ml of slurry were added to the experimental setup before the experiment to ensure a bath-like condition around the contacting surfaces throughout the tests.

Two kinds of speed sets were utilized: multi-step and constant speeds. For the multi-step speed experiments with the 5 µm and 13 µm slurries, the sliding speed was decreased stepwise from the fastest (400 mm/s) to the slowest (50 mm/s) speed, as shown in Figure 3.5, holding each of the nine steps for two minutes in order to generate data that can be evaluated as Stribeck curves. Each complete multi-step speed set (referred to as a ramp) was repeated five times, resulting in a total sliding distance of 846 m. To avoid any impact that may originate from a potential running-in process, only the last three ramps were used to calculate the mean value of the friction coefficient at each sliding speed. To ensure reproducibility, all experiments were carried out at least three times with completely new pins and disks.
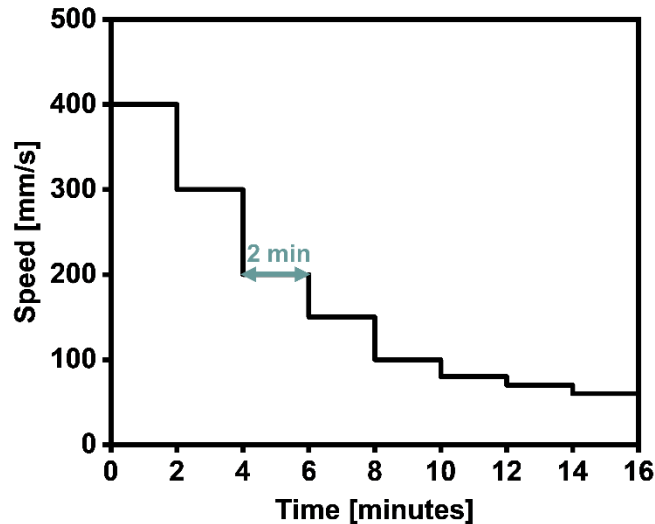
Figure 3.5: Multi-step speeds set, the sliding speed was decreased stepwise from the fastest (400 mm/s) to the slowest (50 mm/s) with each step of two minutes.

The highest (400 mm/s) and the lowest (50 mm/s) speeds of multi-step speeds set were selected to perform constant speed tests with the 5 µm slurry to reveal the wear mechanisms in different lubrication regimes. The second variable in the constant speed tests was the sliding distance, with values of 0.13 m (one revolution of the disk), 1 m, 10 m, 50 m, and 846 m for each speed. With the aim of evaluating the wear performance at 400 mm/s and 50 mm/s, experiments with the longest sliding distance (846 m) were repeated three times with fresh samples.

3.3.2   Investigating the Influence of Waviness on Abrasive Wear

To investigate the influence of disk waviness on abrasive wear, tribological tests were carried out with a CSEM Tribometer 2.0 with a 50 Hz sampling rate. 100 ml of slurry were added before each experiment to ensure bath-like conditions around the contacting surfaces throughout the tests.

In total, four different experimental settings were tested, as shown in Table 1. Initially, we examined the abrasive size effects under the same disk waviness with two experimental settings,

5_S and 13_S. Here, in the experiment label, "5" and "13" represent slurries with different

particle sizes, referring to the 5 µm slurry and the 13 µm slurry mentioned in section Table 1;

while "S" indicates the disk has a small waviness, $W_t \leq 2$ µm, the minimum achievable disk

waviness in our laboratory. To further investigate the influence of disk waviness W_t on abrasive

wear, a disk with deliberately larger waviness ($W_t \geq 7$ µm) was prepared and then tested with

a 13 µm slurry, label 13_L. "L" denotes that the disk utilized in the experiments possesses a

significantly larger waviness W_t. To explore the impact of waviness on abrasive wear at an

early stage, a short distance experiment was designed, referred to as 5_S_50. In this case, the

sliding distance was limited to 50 meters, whereas the other experiments had a sliding distance

of 846 m.

Table 1: Four different experimental settings. Two kinds of slurry with different abrasive
particle sizes were used, 5 µm slurry and 13 µm slurry, "5" and "13" in the label
represent slurry with different particle sizes. "S" in the label indicates the disk has
small waviness, $W_t \leq 2$ µm, while "L" denotes that a significantly larger disk
waviness W_t. The sliding distance was 846 m for all experiments except for one with
50 m (5_S_50).

Label	Slurry size	W_t (Total height of the waviness profile)	Sliding distance
5_S	5 µm	≤ 2 µm	846 m
5_S_50	5 µm	≤ 2 µm	50 m
13_S	13 µm	≤ 2 µm	846 m
13_L	13 µm	≥ 7 µm	846 m

3.3.3 Investigating the Influence of Oscillation and Waviness in Various Conditions

The CSEM Tribometer 2.0 was used for the experiments aimed at investigating the influence

of disk waviness and contacting surfaces' oscillation in various conditions, and the data

acquisition frequency was set at 50 Hz. Three kinds of experiments were performed with different interfacial media:

- **"Abrasive experiments":** 5 ml of water-based 5 µm Al_2O_3 abrasive slurry were added once before the experiment started.

- **"Lubricated experiments":** 5 ml FAV 1 oil were added once before the experiment started.

- **"LTA (lubricated to abrasive) experiments":** 5 ml FAV 1 oil were added once before the experiment started, and after 100 meters of sliding, 5 ml of 5 µm Al_2O_3 abrasive slurry were added to simulate the onset of abrasive wear. These experiments aimed to investigate the transition from lubricated conditions to abrasive wear.

3.4 Materials Characterization and Data Evaluation

3.4.1 Scanning Electron Microscopy

The scanning electron microscopes (SEM) are among the most versatile instruments available for examining and analyzing microstructural characteristics. One of the major reasons for the SEM's usefulness is its high resolution, which can reach 1-5 nm. For the microstructural and the worn surface characterization, a focused ion beam/scanning electron dual-beam microscope (FIB/SEM; Helios NanoLab Dual-beam 650 from FEI, Hillsborough, USA) was used. The worn surfaces of both pin and disk were examined by scanning electron microscopy. Cross-sectional SEM images were taken in the wear track and perpendicularly to the sliding direction to study the effect of abrasive wear on the subsurface of the disk. Two platinum layers were deposited before ion milling to limit the damage due to the ion beam; the first one was deposited with the electron beam, the second by the ion beam.

3.4.2   Chromatic White Light (CWL) Profilometry

Chromatic white light (CWL) profilometry is a non-destructive and non-contacting surface topography measurement based on the principle of chromatic aberration [105]. As shown in Figure 3.6, a measuring head featuring a strongly wavelength-dependent focal length (chromatic aberration) focuses white light on the surface. Only the incident light focused precisely at the intersection point of the optical axis and the object's surface is capable of entering the spectrum analyzer, generating a peak in the spectrometer. The distance from the sensor to the sample can be determined by the wavelength of this peak, along with a calibration table [106]. This technique is highly suitable for large-area characterization, such as whole wafers. In this thesis, FRT MicroProf MPR 1024 (Bergisch Gladbach, Germany) with an optical sensor CHR 150 N was employed for measuring the topography of the whole disk; the vertical resolution is up to 10 nm and lateral resolution up to 1 µm.
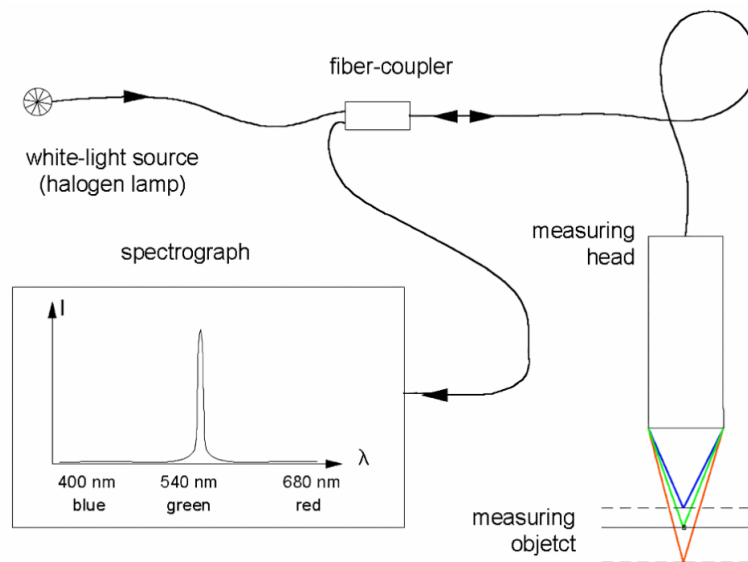
Figure 3.6: Principle of chromatic white light (CWL) measurement [106]. A white light beam undergoes dispersion, separating into distinct chromatic components with different wavelengths. These individual components converge at different positions along the optical axis. Only the incident light focused precisely at the intersection point of the optical axis and the object's surface is capable of entering the spectrum analyzer, generating a peak in the spectrograph.

3.4.3 Confocal Laser Scanning Microscopy

Confocal laser scanning microscopy is an advanced imaging technique that uses laser light to create high-resolution, three-dimensional images of samples. As shown in Figure 3.7, the basic principle of confocal microscopy is that the illumination and detection light are focused on the same diffraction-limited spot, which is moved over the sample to build the complete topography image on the detector [107]. The term "confocal" derives from the presence of two focal points: one at the surface of the sample and the other at the photodetector. Only the light beams that form a focus at the sample surface manage to establish a secondary focus at the photodetector and reach their destination. Other light beams fail to reach the photodetector. In essence, confocal optics exclusively capture reflected light from the focal plane. In this thesis, the PLµ Neox (SensoFar, Barcelona, Spanien) was employed with a vertical resolution down to 1 nm.
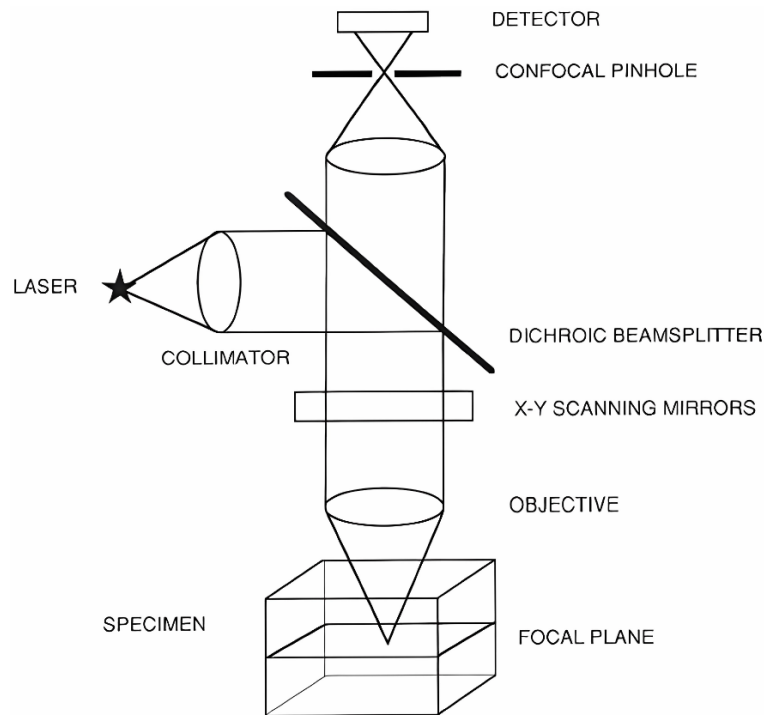
Figure 3.7: Schematic diagram of the optical pathway in a Confocal laser scanning microscopy
system [108]. The emitted light beams from the light source traverse an objective
and converge precisely onto the sample's surface. Subsequently, the light beams
reflected by the sample retrace their path through the same objective, ultimately
being directed toward the detector. The detector selectively registers only those
light beams that achieve a sharp focus and successfully pass through the pinhole
positioned directly in front of it.

3.4.4   Disk Waviness Profile

The surface topography data from chromatic white light (CWL) profilometry (FRT MicroProf

MPR 1024) was used to extract the surface profile along the sliding track (Figure 3.1). Thereby

the sliding track was divided into 120 sectors, and the waviness profile was obtained by

averaging the height of each sector and following with a profile filtering with a cut-off length

$\lambda_c = 0.08$ mm (in accordance with ISO 16610).

3.4.5   Wear Measurement

For the experiments investigating the tribological mechanism of abrasive wear (in chapter 3.3.1), the pins' wear was measured as a loss in weight with a precision scale (R160P, Sartorius research), with a resolution of 0.01 mg. The wear induced volume loss of the disks was determined with the FRT MicroProf optical surface profilometer's data. The disks were scanned in a square area with a side length of 78 mm and a size of 500*500 px. As shown in Figure 3.8, the cross-sectional area of the wear track was measured from eight fixed locations, and the result on each position is an average of 20 px. The average cross-sectional area of the wear track can then be used to calculate volumetric wear.

Figure 3.8: Volume loss evaluation using FRT MicroProf optical surface profilometer's data. Eight fixed locations were chosen to extract the cross-sectional area of the wear track, and the result on each position is an average of 20 px. The average cross-sectional area of the wear track can then be used to calculate volumetric wear.
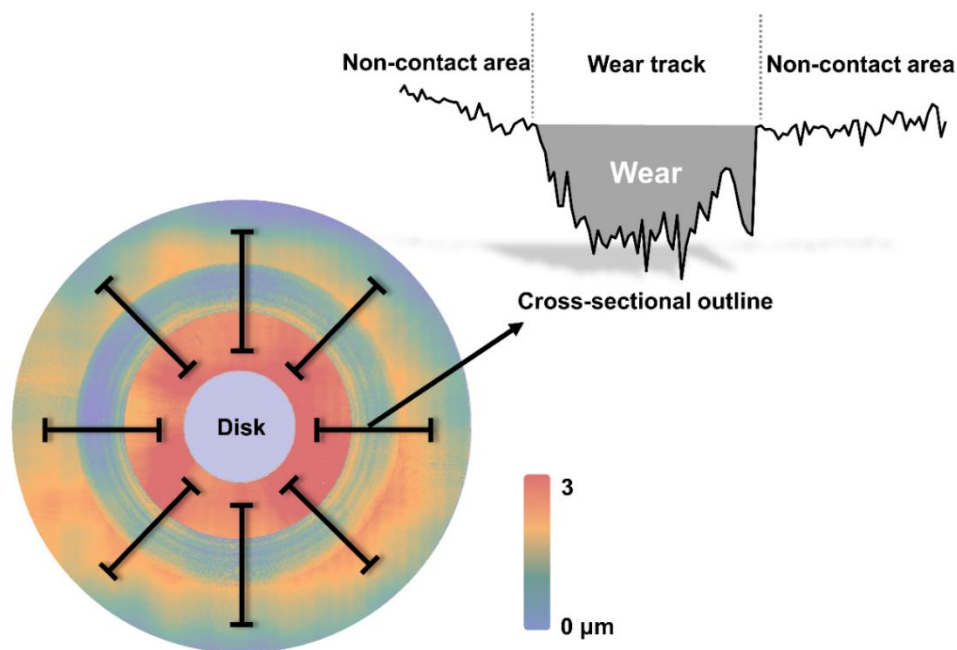
For the experiments investigating the influence of waviness and oscillation on abrasive wear (in chapter 3.3.2 and chapter 3.3.3), the amount of wear along the sliding track was calculated

by comparing the surface topography before and after the experiments (data from chromatic white light profilometry, FRT MicroProf MPR 1024).

3.4.6 Lubrication Film Thickness Variation

For the multi-step speed tests, the distance between the pin and the disk was measured with a capacitive sensor on the top of the pin holder (in Figure 3.3b). When the speed varies during the multi-step speed experiments, the change in the distance between the pin and the disk can also be monitored and is interpreted as the change in film thickness Δh. These Δh are also the average values of the three experiments. With this approach, the changes in separation between pin and disk due to wear are inevitably included. However, the change in film thickness was only considered for the 14 seconds before and after the speed change; thus, wear-induced separation changes are negligible and as a first order approximation ignored. According to the Hersey number in the Stribeck curve [109], it is evident that lubrication film thickness increases with the increase in velocity. Therefore, the film thickness value at the lowest experimental velocity of 50 mm/s was chosen as our reference point. It was assumed that the film thickness at 50 mm/s was only determined by the particle size d of the slurry, 5 and 13 µm respectively. With this assumption, the relative variation in film thickness R_v can be calculated in Eq.(3.1):

$$R_v = \frac{\Delta h}{d} \cdot 100\% \tag{3.1}$$

3.4.7 Roughness Measurement

The roughness distribution was measured radially every 15 degrees along the sliding track with a stylus profilometer HOMMEL-ETAMIC T8000 R120-400 (in Figure 3.9). These roughness measurements were performed for all disks before and after the tribological tests. Before the tribological experiments, the measurement direction was parallel to the sliding direction. In

contrast, the measurement direction was perpendicular to the sliding direction for the disks after the tests. The reason behind these choices is to measure perpendicular to the grinding/wear marks on the surfaces.
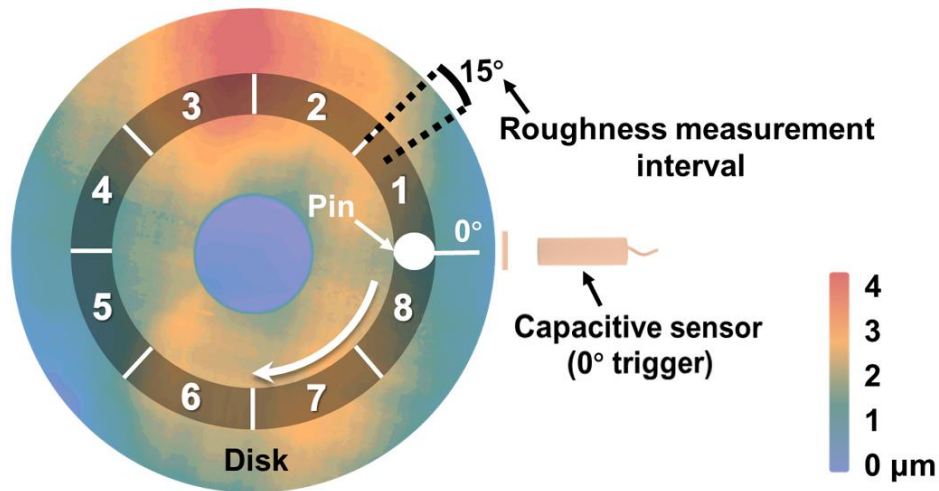
Figure 3.9: Top view of disk surface topography, separating the tribological data into eight zones with respect to the zero degree position defined by the capacitive sensor and roughness measurement with every 15 degrees interval on the disks' sliding track. From [103] with permission.

3.4.8   Data Segmentation

With a sampling rate of 50 Hz and a sliding speed of 50 mm/s, the precision of the tribological data is 1 mm along the sliding track (132 mm total sliding track per revolution). As shown in Figure 3.9, the zero position trigger allows the tribological data to be divided into individual cycles, which provide information on the friction coefficient at specific positions on the disk. This information helps to understand how the friction coefficient changes as the pin moves along the sliding radius. For example, the tribological data can be separated into eight zones; the angle-resolved tribological data can be obtained by dividing the entire 132 mm sliding track (360°) into 120 equal sectors. The average friction coefficient for each sector was calculated by averaging the data over the following 3 degrees.

3.4.9   Oscillation of the Contacting Surfaces

In this thesis, the term "oscillation of the contacting surfaces" specifically refers to the oscillation caused by the tilt of the disk mounting. Figure 3.10 illustrates the oscillation induced by the disk mounting's tilt in a pin-on-disk test. Ideally, the load axis should be perpendicular to the disk surface, as shown in Figure 3.10a, but achieving this is challenging. It is inevitable that the disk mounting will introduce some degree of tilt, as shown in Figure 3.10b, which in turn leads to what we have termed as "oscillation". What one can do is to make every effort to minimize the amplitude of oscillation, as we did in this thesis, such that the amplitude of oscillation is limited to 4 µm.
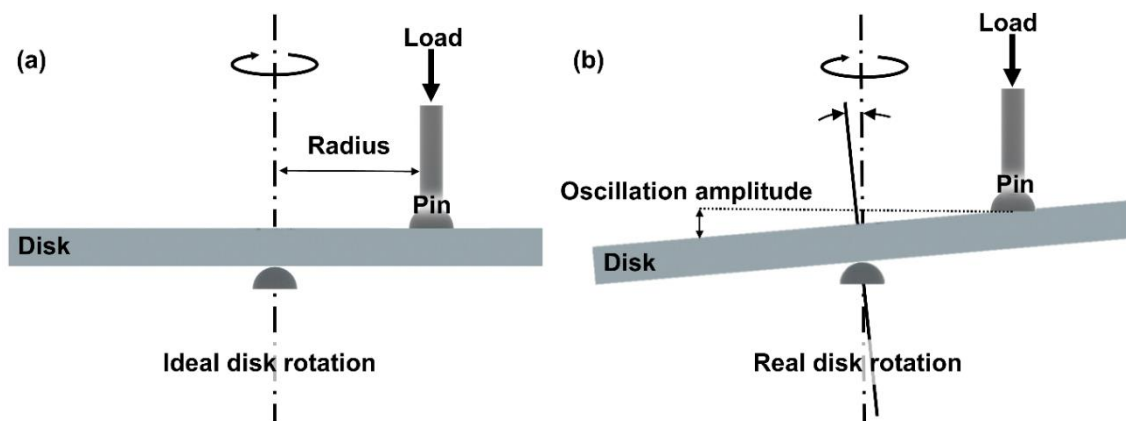
Figure 3.10: Schematic of "oscillation of the contacting surfaces" due to disk mounting tilt: (a) the ideal disk rotation in a pin-on-disk configuration, with the load axis perpendicular to the disk surface; the load is applied from the top of the pin, and the tribological contact occurs at a fixed radius. (b) the real disk rotation in a pin-on-disk configuration, the disk mounting inevitably results in tilting, which, in turn, leads to oscillations in the contacting surfaces.

However, the height difference data recorded by the capacitive sensor in Figure 3.4a was not the oscillation of contacting surfaces; it also included surface topography information. Therefore, the oscillation of the contacting surfaces was evaluated by subtracting the surface topography data (as shown in Figure 3.1) from the capacitive sensor data in Figure 3.4a.

3.4.10 Slope Angle of the Disk Waviness Profile

The slope angle of the disk waviness profile was evaluated through the waviness profile of the sliding track. An illustration of the evaluation of the slope angle is shown in Figure 3.11, where the slope angle of each sector was calculated from the slope of two selected points. For example, the slope angle at point L was determined with the slopes of points L_1 and L_2, which are always nine degrees apart from L. In order to better distinguish the two distinct characteristics of the waviness profile, the upward angle (θ_1) was defined as a positive value, while the downward angle (θ_2) was negative.
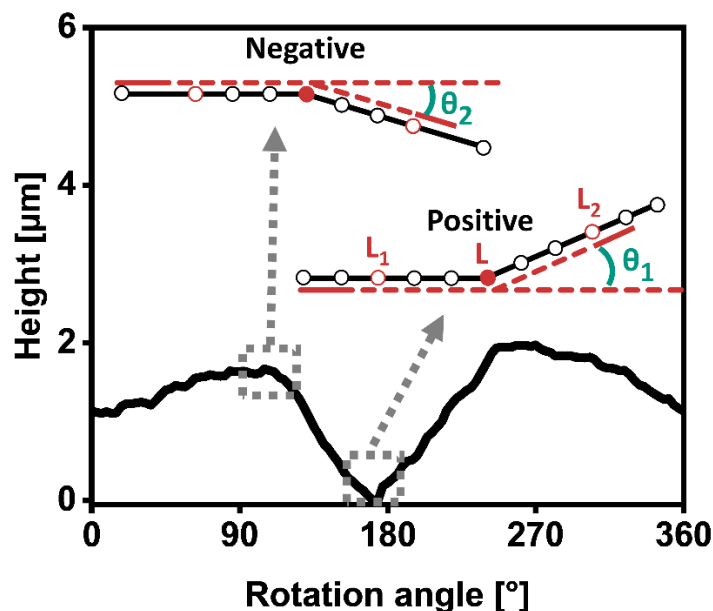
Figure 3.11: Schematic of the evaluation of the slope angle on a waviness profile; the upward trend was defined as a positive value (θ_1), while the downward trend was defined as a negative value (θ_2).

3.4.11 Z-score of the Friction Coefficient

In statistics, a Z-score, also known as a standard score, is a statistical measure that quantifies the number of standard deviations a data point is from the mean of a dataset. It is used to show how a particular data point relates to the overall distribution of data [110].

In this thesis, the Z-score of the friction coefficient refers to calculating the number of standard deviations by which a particular sector's friction coefficient deviates from the average friction coefficient on the sliding track. This deviation can be represented using the Z-score of the friction coefficient, which is calculated as follows:

$$z = \frac{\mu_x - m}{\sigma} \tag{3.2}$$

Where m is the mean of the friction coefficient along the sliding track, σ is the standard deviation of the friction coefficient along the sliding track, and μ_x is the friction coefficient of a sector (out of a total of 120 sectors).

The introduction of the Z-score in this thesis serves to make the deviations in friction coefficient from various experiments comparable. For instance, when one experiment yields a friction coefficient of 0.8±0.2 and another yields 0.1±0.1, it becomes challenging to directly compare which experiment exhibits more pronounced fluctuations in the coefficient of friction. However, the Z-score enables the direct comparison of friction force deviations from different experiments, as the values do not retain the original unit of measurement.

3.4.12 Time-frequency Analysis

Time-frequency analysis is a valuable technique in studying the intricate interactions involved in tribology. It allows for a comprehensive analysis of signals in both the time and frequency domains, thereby providing deeper insights into tribological data [111,112]. Time-frequency analyses are often performed using techniques such as the short-time Fourier transform (STFT) [113], the Wigner distribution (WD) [114], and the Hilbert-Huang transform (HHT) [115]. This approach has found broad applications in diverse fields, ranging from optics, as demonstrated

by Alonso [116], to speech analysis, as illustrated by Taal [117], and even in evaluating the physical condition of mechanical systems, as demonstrated by Wang [118].

Of the various numerical methods for time-frequency analysis mentioned above, the short-time Fourier transform is particularly useful for tribological experiments involving long-duration processes [114]. STFT involves breaking down a signal into smaller segments, allowing for analysis over short time intervals, as illustrated in Figure 3.12. The signal is divided into overlapping frames, and the Discrete Fourier Transform (DFT) is computed for each frame using the Fast Fourier Transform (FFT) algorithm. This results in a time-frequency representation of the signal, where the frequency content is analyzed at different time intervals.
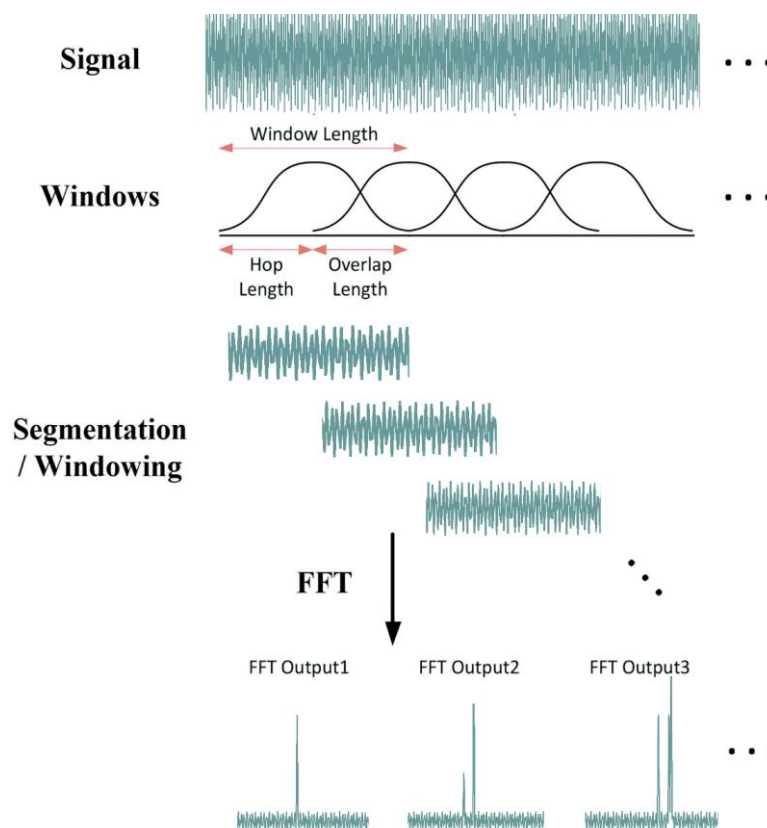
Figure 3.12: Overview of the short-time Fourier transforms (STFT). The principle involves using a Gaussian-shaped sliding window to segment the signal, the Fast Fourier Transform (FFT) is then applied to each window separately. This results in a time-frequency representation of the signal, where the frequency content is analyzed at different time intervals.

In the short-time Fourier transform (STFT), a window function is moved along the signal with a hop length, and the FFT operation is performed on the samples within the window. This allows for the frequency content of the signal to be measured over time [119]. Mathematically, STFT can be written as [113,114]:

$$STFT(t, \omega) = \int_{-\infty}^{\infty} x(\tau)\, g(\tau - t)e^{-j\omega\tau}\, d\tau \tag{3.3}$$

Where t is time, ω is frequency, x is the signal to be transformed, g is a window function centered at time t, and j is the imaginary unit with $j^2 = -1$.

The energy density spectrum of the STFT is known as the Power Spectral Density (PSD) and can be written as follows:

$$PSD = |STFT(t, \omega)|^2 \tag{3.4}$$

The resulting spectrogram displays the Fourier transforms of each time window along the x-axis, with corresponding frequencies along the y-axis. The spectral energy density of frequency components is represented by color values in the Power Spectral Density (PSD) representation. A time window of 20 seconds with a 50% overlap was utilized to achieve a desirable balance between time and frequency resolution.

4 Results

4.1 Tribological Mechanisms of Abrasive Wear

All the experiments in this chapter were conducted using the CSEM Pin-on-Disk Tribometer 1.0 introduced in chapter 3.2.1, and experimental details can be seen in chapter 3.3.1.

4.1.1 Multi-step Speed Experiments

In order to investigate the influence of increasing fluid film thickness caused by the hydrodynamic pressure on lubricated abrasive wear, multi-step speed experiments were conducted with slurries of two different particle sizes, 5 µm and 13 µm. The results of the multi-step experiments are presented in Figure 4.1, giving an overview of the friction coefficients under abrasive wear as well as the relative variation in film thickness R_v between the two frictional surfaces as a function of the sliding speed. As the speed increases, the friction coefficient decreases from 0.31 at 50 mm/s to 0.08 at 400 mm/s — a drop in friction coefficient of about 2/3. Simultaneously, a significant variation in film thickness is observed for the 5 µm slurry with sliding speed; the film thickness increases 14% at 400 mm/s under abrasive wear. The results for the 13 µm slurry exhibit a different trend compared to the 5 µm one and the sliding speed has a negligible effect on the friction coefficient. The friction coefficient only drops from 0.25 to 0.23 when the sliding speed increases from 50 mm/s to 400 mm/s. Simultaneously, the increase in film thickness is negligible and about 1%.
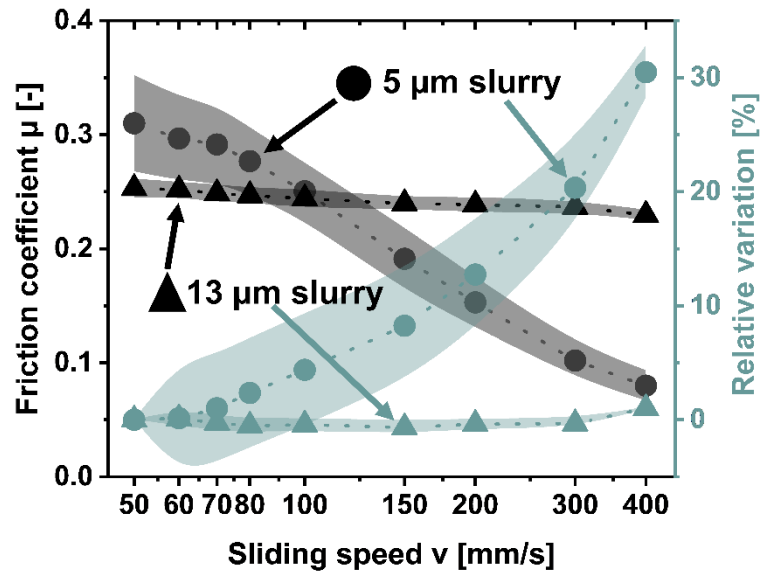
Figure 4.1: Friction coefficient and relative variation in film thickness R_v of frictional surfaces as a function of the sliding speed; the semi-transparent bands represent the standard deviation. The sliding speed strongly affects the friction coefficient when using 5 μm slurry, while the sliding speed has a negligible effect on the friction coefficient when using 13 μm slurry.

4.1.2   Constant Speed Experiments with the 5 μm Slurry

In Figure 4.2, the friction coefficient and wear loss for experiments with the 5 μm slurry at two constant speeds are shown. At 400 mm/s, the friction coefficient almost double, from 0.06 at the beginning to approximately 0.12 in the later stages. At 50 mm/s, the coefficient of friction rises from 0.15 at the beginning of the test to around 0.25 at the end. If we compare the overall average friction coefficient for the constant speed experiments, the ratio between the value for the tests at 400 mm/s to the one at 50 mm/s – μ400/μ50 – is approximately 1/3. Another marked contrast is the deviation of the friction coefficient, which was much more prominent throughout the whole constant speed tests at the low speed (50 mm/s).
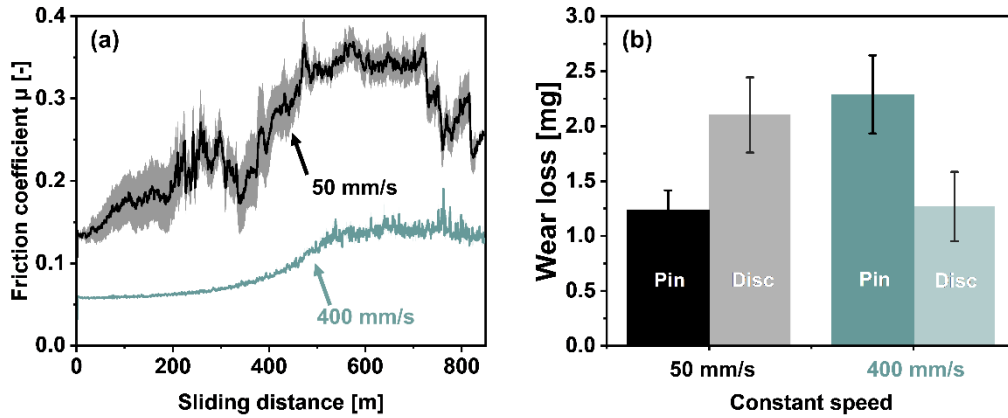
Figure 4.2: Results for the 5 µm slurry at constant sliding speeds of 50 and 400 mm/s for a maximum sliding distance of 846 m: (a) friction coefficient as a function of sliding distance, the semi-transparent bands represent the standard deviation.; (b) wear results of pin and disk for the two constant speeds.

The data in Figure 4.2b shows the results of the wear analysis of both frictional surfaces after experiments at different constant speeds. The sum of the wear of the entire tribological system after 400 mm/s and 50 mm/s experiments is 3.54±0.67 mg and 3.34±0.52 mg, respectively. Although the total amount of wear remains almost the same for the two different constant speeds, the wear loss has a different distribution between the pin and disk. At the low speed (50 mm/s) tests, the wear produced on the pin is about 1.24±0.18 mg, whereas the disk has a weight loss of 2.1±0.34 mg, which is 1.7 times that of the pin. The wear distribution is inverted 400 mm/s tests, leading to a wear loss of 2.29±0.36 mg for the pin and 1.27±0.32 mg for the disk.

Figure 4.3 presents SEM images of pin surfaces after different sliding distances at constant speeds for sliding distances of 10, 50, and 846 m. All worn surfaces were imaged in the center of each pin. After 10 m of sliding at 50 mm/s, clear and dense grooves are visible on the worn surface of the pin in Figure 4.3a. As the sliding distance increases to 50 m at 50 mm/s (in Figure 4.3b), the worn surface of the pin does not change much compared with that after 10 m, with

plenty of grooves and few indents. With the sliding distance increasing to 846 m, wider grooves and more indents are observed in Figure 4.3c compared to the surfaces after 10 m and 50 m. The worn surfaces of the pins after 400 mm/s experiments show different features from 50 mm/s ones. In Figure 4.3d, which shows the worn surface after 10 m at 400 mm/s, only some indents and very few grooves can be seen. After 50 m at 400 mm/s (in Figure 4.3e), indents distributed across most of the wear track and grooves are rare and shallow. With the sliding distance rising to 846 m at 400 mm/s (in Figure 4.3f), one can observe that the wear track is entirely covered by indents. As for the short distance experiments at 400 mm/s (10 m and 50 m), only sparse grooves can be seen with unclear traces.

Figure 4.3: SEM images of pins after constant speeds experiments: (a) Sliding 10 m at 50 mm/s; (b) Sliding 50 m at 50 mm/s; (c) Sliding 846 m at 50 mm/s; (d) Sliding 10 m at 400 mm/s; (e) Sliding 50 m at 400 mm/s; (f) Sliding 846 m at 400 mm/s. From [120] with permission.

The difference in the worn surfaces at different constant speeds also appears on the disks (see Figure 4.4), which are the counter bodies for the pins presented in Figure 4.3. The worn surfaces of the disks show the same trends as the pins, with more grooves after low speed

experiments (Figure 4.4a-c) and more indents after high speed experiments (Figure 4.4d-f). Notably, the grooves in Figure 4.4 are not all formed during the tribological tests; those grooves perpendicular or approximately perpendicular to the sliding direction are the vestiges of the grinding process during sample preparation.
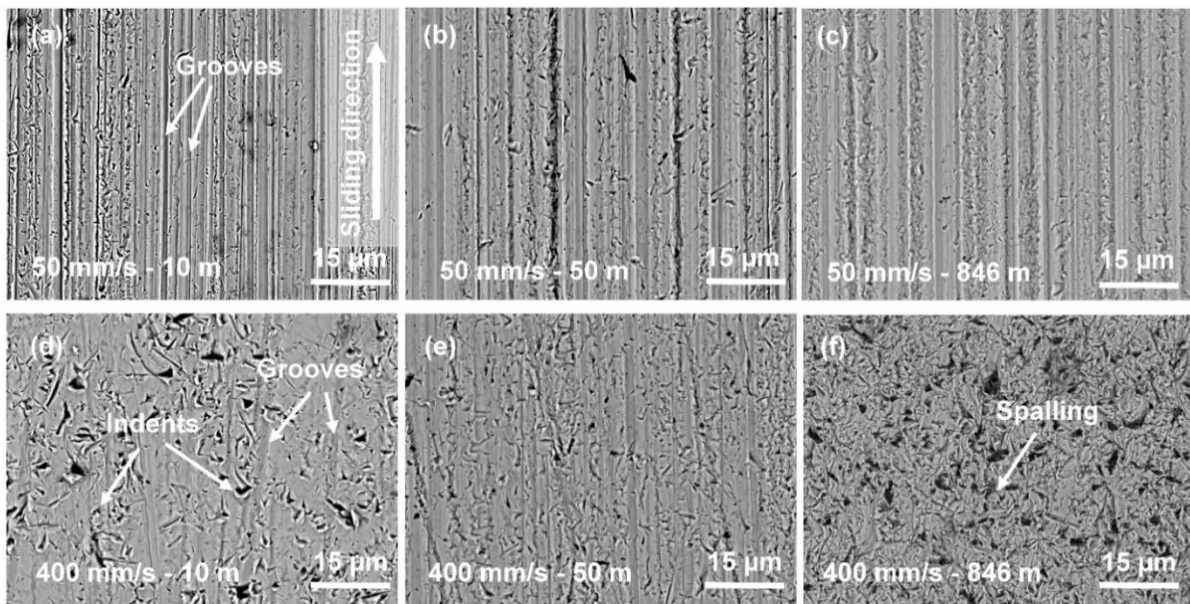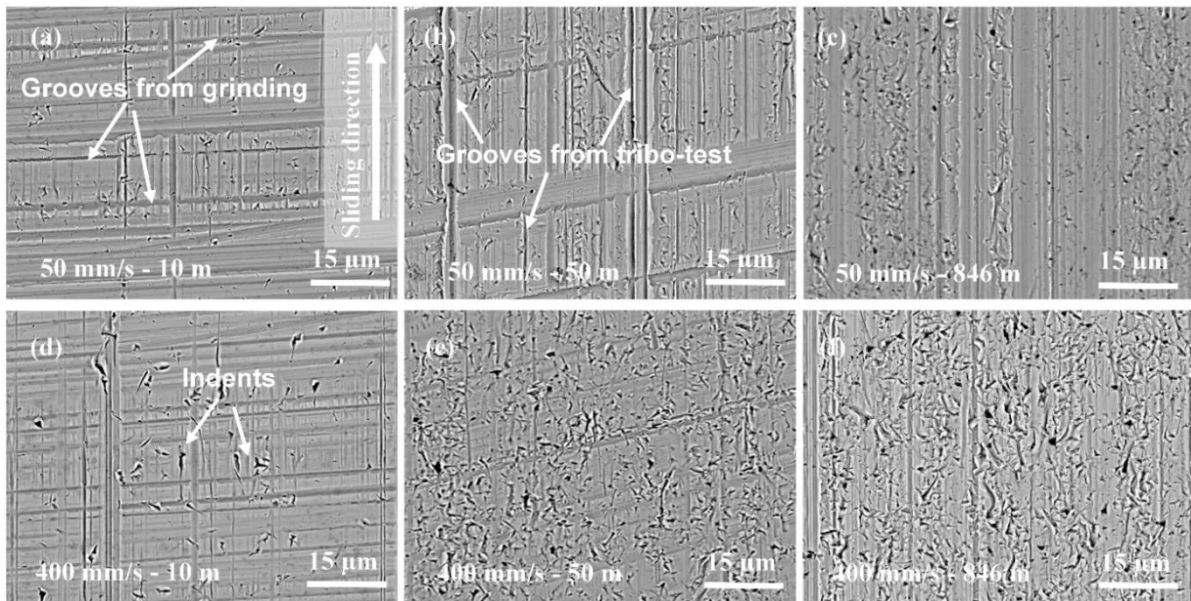

Figure 4.4: SEM images of disks after constant speeds experiments: (a) Sliding 10 m at 50 mm/s; (b) Sliding 50 m at 50 mm/s; (c) Sliding 846 m at 50 mm/s; (d) Sliding 10 m at 400 mm/s; (e) Sliding 50 m at 400 mm/s; (f) Sliding 846 m at 400 mm/s. From [120] with permission.

For a better understanding of the different mechanisms of abrasive wear, Figure 4.5 shows cross-sectional SEM images of the tribologically deformed subsurface material taken in the middle of the pin; a cross-sectional image of an undeformed pin is presented in Figure 4.5e. For the unloaded pin, the surface is smooth, and no subsurface deformation is observed in the subsurface area. The fine grained layer [34] results from the grinding process during sample preparation. Hardly any subsurface cracks are found in the cross-sectional SEM images after 50 m at 50 mm/s (Figure 4.5a). Only sporadic cracks exist in the subsurface after 846 m at 50 mm/s (Figure 4.5b). A considerable number of subsurface cracks appears in the early stage

of experiments at 400 mm/s (Figure 4.5c). For the 400 mm/s experiments after 846 m, a

network of cracks and a fractured subsurface becomes visible with depths from 200 nm to

650 nm (Figure 4.5d).
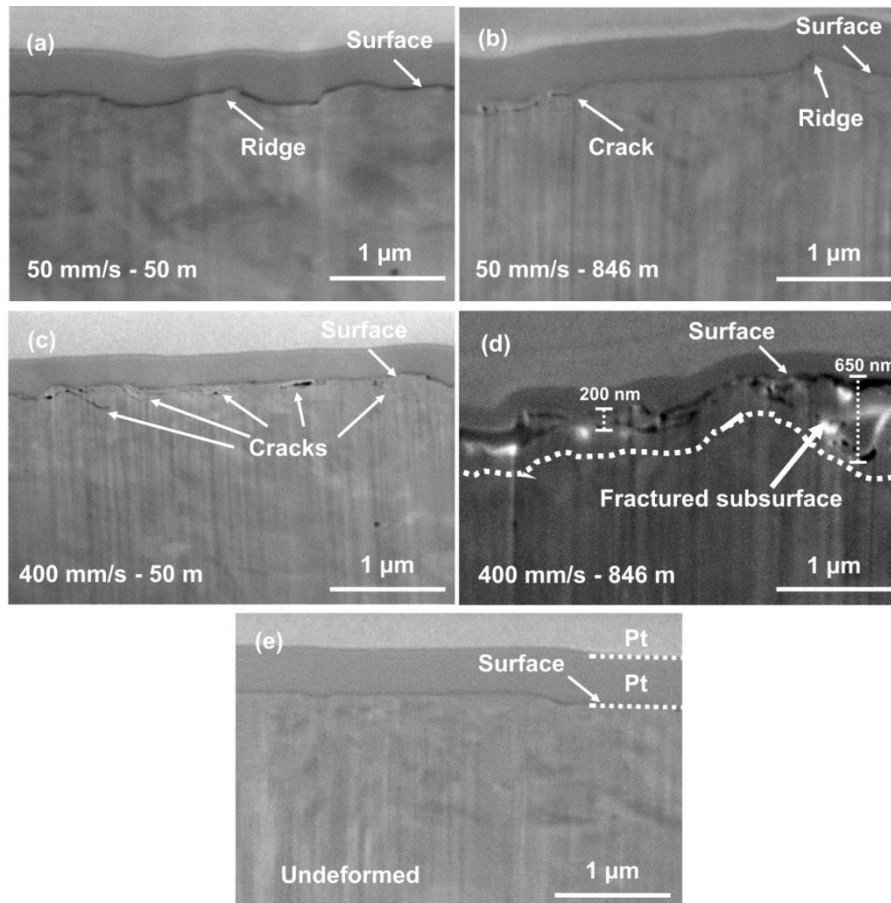
Figure 4.5: Cross-sectional SEM images of pins: (a) Sliding 50 m at 50 mm/s; (b) Sliding
846 m at 50 mm/s; (c) Sliding 50 m at 400 mm/s; (d) Sliding 846 m at 400 mm/s.
A considerable number of subsurface cracks appear at 400 mm/s in (c) and (d). At
50 mm/s, hardly any subsurface cracks can be found in (a), and only few cracks
exist in (b). From [120] with permission.

4.2 Influence of Disk Waviness on Friction and Abrasive Wear

All the experiments in this chapter were conducted using the CSEM Pin-on-Disk Tribometer

2.0 introduced in chapter 3.2.2, and experimental details can be seen in chapter 3.3.2. Four

different experimental setups were employed, denoted by abbreviations: 5_S, 13_S, 13_L, and 5_S_50. Here, 5 and 13 correspond to the abrasive particle size of the slurry, specifically 5 µm and 13 µm. The letter "S" represents the disk with a small waviness ($W_t \leq 2$ µm), while "L" represents the disk with a large waviness ($W_t \geq 7$ µm). All experiments had a sliding distance of 846 m, except for 5_S_50, where a reduced sliding distance of only 50 m was used to observe the tribological behavior in the early stages.

4.2.1 Disk Waviness Profile

Figure 4.6 displays the waviness profile and roughness distribution along the sliding track for four disks, which were then tested with the corresponding settings presented in Table 1. For the considered specific disks with a small waviness (5_S, 5_S_50, and 13_S), the total height of the profile W_t along the sliding track is 1.94 µm, 1.77 µm, and 1.56 µm, respectively. However, even with the same waviness standard ($W_t \leq 2$ µm), the waviness profiles of 5_S, 5_S_50, and 13_S differ significantly from each other. 5_S has two peaks with a sharp peak (around 110°) considerably higher than another peak (between 230° to 300°). The waviness profile of 5_S_50 also has two peaks, but the heights of the peaks in 5_S_50 are very close. Unlike 5_S and Disk 5_S_50, 13_S does not have significant high peaks but several small peaks along the sliding track. The waviness of 13_L was intentionally not mitigated during the grinding process, which yielded a total waviness profile height of $W_t = 7.24$ µm. The roughness R_a along the sliding track of the disks with a small waviness (5_S, 5_S_50, and 13_S) ranges from $0.08 - 0.12$ µm, with average values of 0.09 µm, 0.09 µm, and 0.11 µm, respectively. 13_L has a slightly higher average roughness than 5_S, 5_S_50, and 13_S, $R_a = 0.15$ µm. Similar to the waviness profiles, the roughness distribution along the sliding track varies from disk to disk.
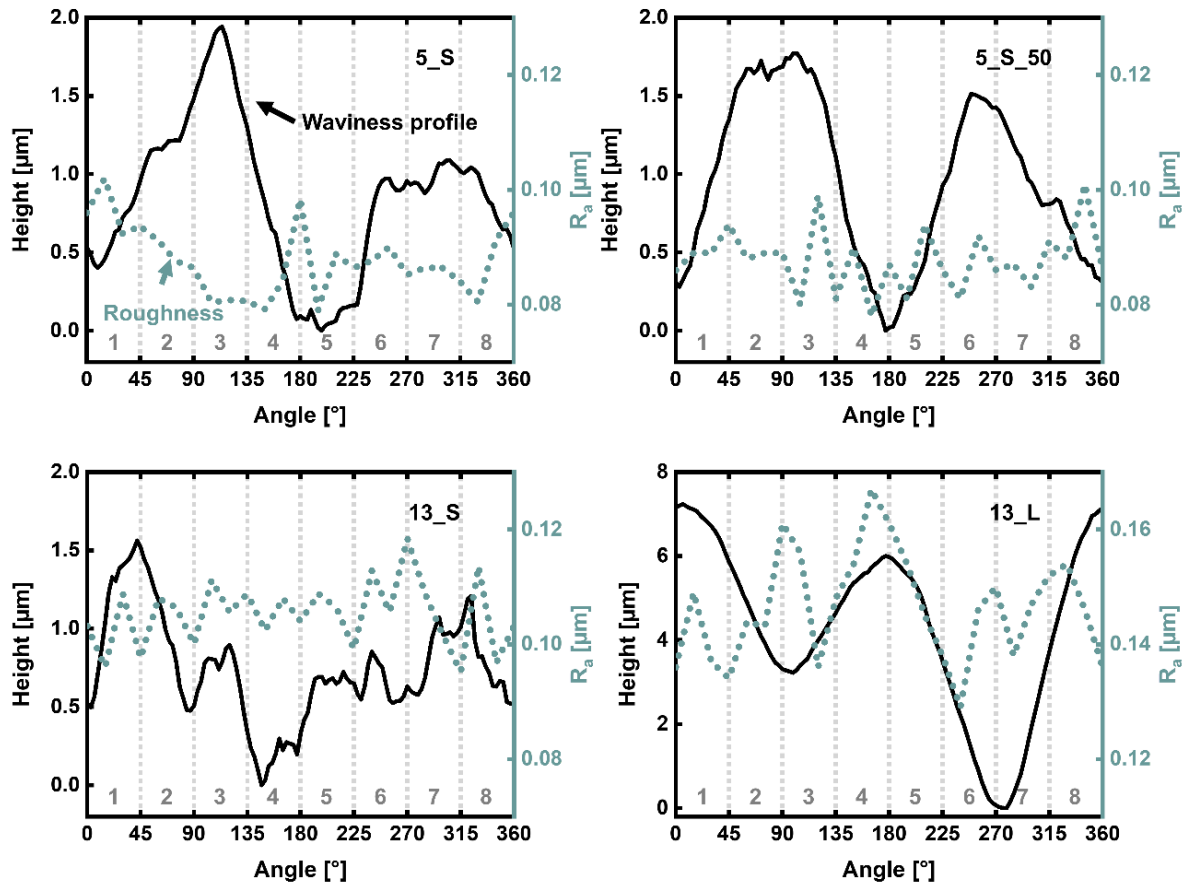
Figure 4.6: Waviness profile and roughness distribution along the sliding track for four individual disks: 5_S, tested with the 5 µm slurry and small waviness; 5_S_50, tested with the 5 µm slurry and small waviness for a short sliding distance (50 m); 13_S, tested with the 13 µm slurry and small waviness; 13_L, tested with the 13 µm slurry and large waviness. From [103] with permission.

4.2.2   Friction

The results for the friction coefficient as a function of the sliding distance for four different settings are presented in Figure 4.7. No smoothing or averaging was applied to these data, and for visualization purposes only the first out of every 100 data points is displayed; the evaluations in all later parts, however, are based on the entire data obtained at a 50 Hz sampling rate. The data shown here gives an overview of the friction coefficient as well as the influence of the abrasive particle size. For the experiments with the 5 µm slurry, small disk waviness, and 846 m sliding distance (5_S), frictional fluctuations appear from the beginning (0 – 50 m)

of the test, ranging from 0.1 to 0.3. An increase in friction coefficient is noticed after 400 m; the friction coefficient increases and then oscillates between 0.2 and 0.5. It is worth noting that although frictional fluctuations drop slightly with sliding distance, they are still considerable (around 0.2). The result of 5_S_50 (tested with the 5 µm slurry and small waviness for a shorter distance of 50 m) shows a similar trend to 5_S; frictional fluctuations start from the beginning of the test, ranging from 0.1 to 0.5.
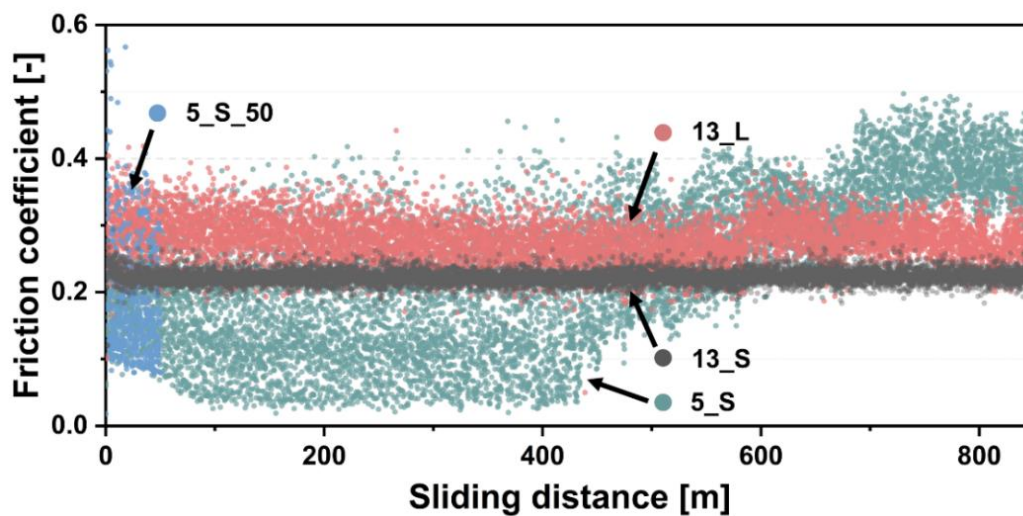
Figure 4.7: Friction coefficient from four experimental settings: 5_S, tested with the 5 µm slurry and small waviness; 5_S_50, tested with the 5 µm slurry and small waviness for a short distance (50 m); 13_S, tested with the 13 µm slurry and small waviness; 13_L, tested with 13 µm slurry and large waviness. From [103] with permission.

The friction coefficient for the experiments with the 13 µm slurry and a small disk waviness (13_S in Figure 4.7) exhibits a different trend than the experiments with the 5 µm slurry and small waviness (5_S and 5_S_50 in Figure 4.7). Apart from a decrease in friction coefficient for the first 20 m, frictional fluctuations mainly range from 0.2 to 0.25. The fluctuations in friction coefficient for 13_S is less than 1/5 compared to the tests performed with the 5 µm slurry (5_S and 5_S_50). The average friction coefficient for the 13_S is $\mu = 0.22$, a bit lower than that for the experiments with the 13 µm slurry and increased disk waviness of around

7 µm (13_L), µ = 0.28. Moreover, 13_L has a more significant fluctuation in friction coefficient (mainly ranging from 0.2 to 0.4) than 13_S (mainly ranging from 0.2 to 0.25).

With a sampling rate of 50 Hz, the tribological data is divided into eight zones of 45-degree intervals (schematic in Figure 3.9). It is possible to average the friction coefficient in each zone, as shown in Figure 3.9. For the results of the experiments with the 5 µm slurry and a small disk waviness (5_S in Figure 4.8), the friction coefficient in zone 3 is relatively high (average µ = 0.33) and low friction coefficient appears in zone 1 and 8 (average µ = 0.18).
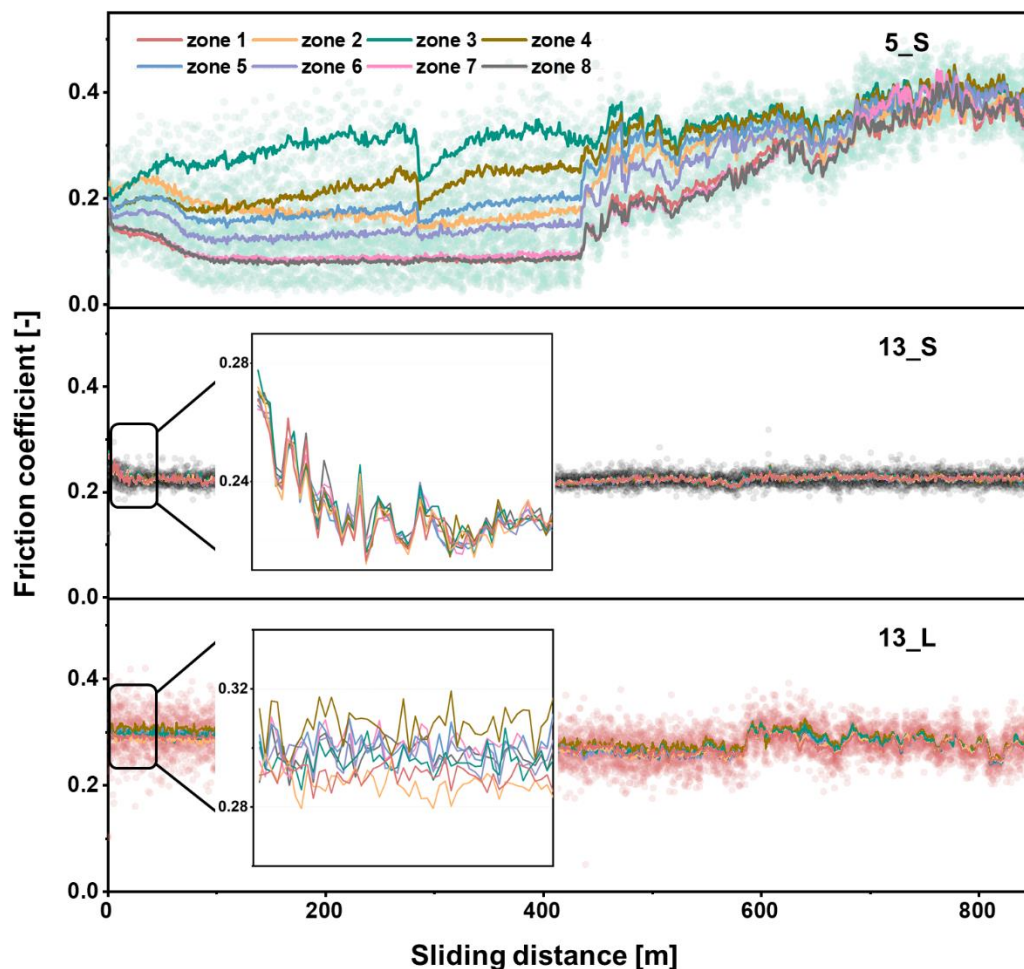
Figure 4.8: The friction coefficient on the disk is divided into eight zones: 5_S, tested with the 5 µm slurry and small waviness; 13_S, tested with the 13 µm slurry and small; 13_L, tested with the 13 µm slurry and large waviness. The maximum difference in friction coefficient between each zone for 5_S and 13_L is 0.2 and 0.04. The zones in 13_S show only little difference. From [103] with permission.

Similar to 5_S, the difference in friction coefficient between the individual zones is distinguished from 5_S_50 in Figure 4.9. The maximum difference in friction coefficient between each zone is up to 0.2 for 5_S and 5_S_50, but for 13_L, the value is only 0.04. In marked contrast to the experiments with the 5 µm slurry (5_S and 5_S_50), the friction coefficient of each zone for 13_S (in Figure 4.8) shows only very little difference.
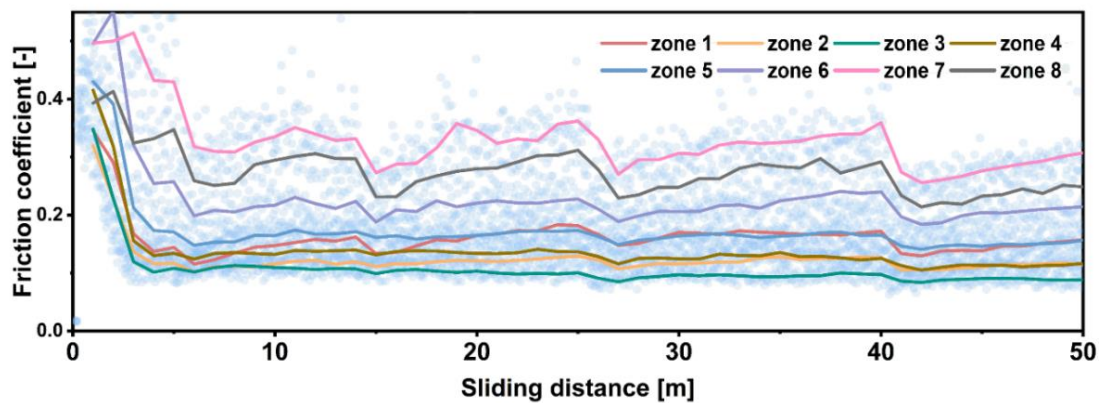
Figure 4.9: Friction coefficient as a function of sliding distance: 5_S_50, tested with the 5 µm slurry and small waviness for a short distance (50 m). The difference in friction coefficient between the individual zones appeared simultaneously with the onset of friction force. From [103] with permission.

4.2.3 Wear

This thesis focuses on the influence of disk waviness on disk wear. By comparing the optical surface topography of the disks before and after experiments, the wear at each position along the sliding track was precisely quantified. As shown in Figure 4.10, the wear-induced height losses for the experiments with the 5 µm slurry and a small disk waviness (5_S), 13 µm slurry and a small disk waviness (13_S), and 13 µm slurry and a large disk waviness (13_L) are shown; the average linear wear along the sliding track are 0.39 µm, 0.31 µm, and 1.47 µm, respectively.

For 13_S, the wear-induced height loss on the frictional track ranges from 0.28 µm to 0.46 µm. A significantly different behavior is noticed for 5_S and 13_L; the wear distribution along the

sliding track is uneven. For 5_S, almost no height loss is present around 0°, whereas the height

loss is close to 1 µm around 110°. Angles between 60° and 160° contribute almost 2/3 of the

wear. Uneven wear also occurs in 13_L: Around 150° the height loss is up to 1.93 µm, while

the lowest height loss appears around 270° (about 1.15 µm).
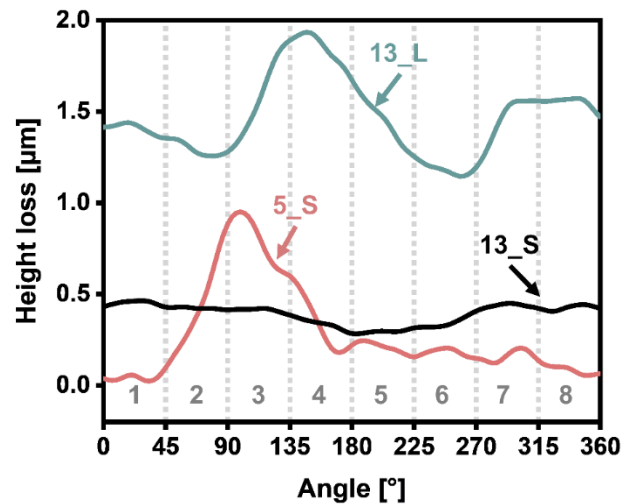
Figure 4.10: Wear-induced height loss along the sliding track: 5_S, tested with the 5 µm slurry
and small waviness, average wear 0.39 µm; 13_S, tested with the 13 µm slurry
and small waviness, average wear 0.31 µm; 13_L, tested with the 13 µm slurry
and large waviness, average wear 1.47 µm. From [103] with permission.

4.2.4   Worn Surfaces

Figure 4.11 presents SEM images of the areas with the highest and lowest friction coefficients

for experiments tested with the 5 µm slurry (5_S and 5_S_50) and the 13 µm slurry with large

waviness (13_L). The SEM images of worn surfaces were all taken in the middle of the sliding

tracks. For 5_S, grooves appear in both the high friction area (Figure 4.11a, corresponds to

zone 3, around 110°) and the low friction area (Figure 4.11c). The grooves in the high friction

area are more pronounced than those in the low friction area. The contrast in the worn surfaces

of different zones also appears for 5_S_50 (Figure 4.11b, 6d). The test of 5_S_50 was

performed for 50 m, so the vestiges of the surface preparation still exist in the wear track (the

grooves vertical or approximately vertical to the sliding direction). For the grooves generated during the tribological experiments, the high friction area (Figure 4.11e) of 5_S_50 has more distinct grooves than the low friction area (Figure 4.11b). The grooves do not have a significant difference between the high friction area and the low friction area of 13_L in Figure 4.11c+f.
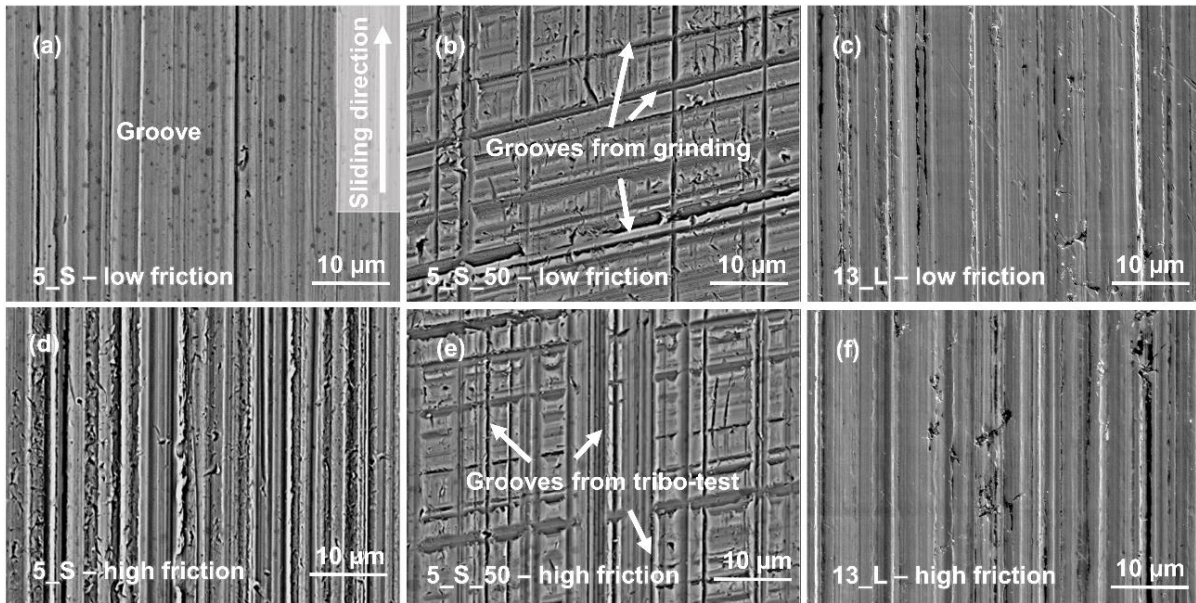
Figure 4.11: SEM images of worn surfaces at different areas on the sliding track: (a) and (d) tested with the 5 µm slurry and small waviness (5_S), (a) is the low friction area around 0°(zone 1 and zone 8), (d) is the high friction area around 110° (zone 3); (b) and (e) tested with the 5 µm slurry and small waviness for a short distance (50 m), (b) is the low friction area around 110° (zone 3), (e) is the high friction area around 300° (zone 7); (c) and (f) tested with the 13 µm slurry and large waviness, (c) is the low friction area around 70° (zone 2), (f) is the high friction area around 150° (zone 4). From [103] with permission.

4.2.5   Roughness Inside the Wear Tracks

The correlation between the friction coefficient and the roughness distribution along the sliding track for 5_S (tested with the 5 µm slurry and a small disk waviness) and 13_L (tested with the 13 µm slurry and a large disk waviness) are highlighted in Figure 4.12. Here, the roughness measurements were performed on the sliding track after the tribological tests. For 5_S, the roughness R_a along the sliding track ranges from 0.08 µm to 0.13 µm, with an average value

of 0.10 µm. 13_L has a relatively larger roughness R_a ranging from 0.19 µm to 0.23 µm, with

average roughness $R_a = 0.21$ µm.
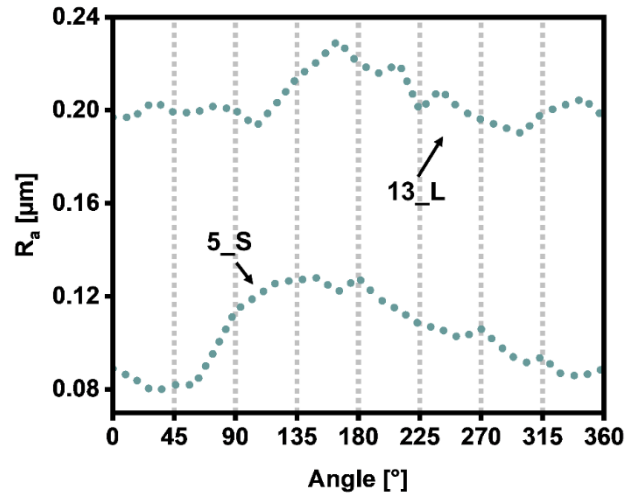
Figure 4.12: Roughness distribution along the sliding track after tribological tests: 5_S, tested
with the 5 µm slurry and small waviness; 13_L, tested with the 13 µm slurry and
large waviness. From [103] with permission.

4.3 Influence of the Contacting Surfaces' Oscillation

All the experiments in this chapter were conducted using the CSEM Pin-on-Disk Tribometer

2.0 introduced in chapter 3.2.2. As described in experimental details (in chapter 3.3.3), three

kinds of experiments were performed with different interfacial media: "Abrasive experiments"

with 5 µm Al_2O_3 abrasive slurry; "LTA (lubricated to abrasive) experiments" with FVA 1 oil

first, followed by the addition of 5 µm Al_2O_3 abrasive slurry after 100 m sliding distance;

"Lubricated experiments" with only FVA 1 oil.

In the "lubricated experiments", two situations can occur: the first is referred to as the "well-

lubricated condition". Here, the lubricant achieves the intended effect, resulting in stable and

low friction coefficients with minimal fluctuations. The second situation, where adding the

lubricant does not yield the desired outcome, leading to friction coefficients that are either not sufficiently low or exhibiting significant fluctuations compared with "well-lubricated experiments", is termed the "unsatisfactory-lubricated experiments".

4.3.1   Friction Coefficient

The results of the friction coefficient as a function of time for four kinds of experiments are presented in Figure 4.13. The solid line in the graph represents the variation of the friction coefficient over time. The friction coefficient is derived from the average value for every meter of sliding distance, while the transparent shaded area indicates the statistical standard deviation, referred to as "frictional fluctuations" in this thesis.
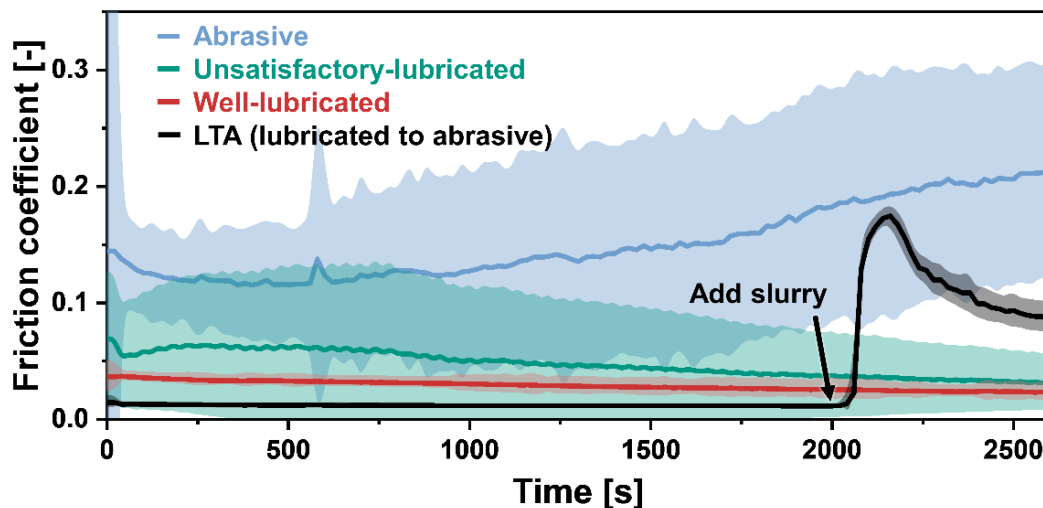
Figure 4.13: Friction coefficient as a function of testing time. The solid line in the graph represents the variation of the friction coefficient over time. The friction coefficient is derived from the average value for every meter of sliding distance, while the transparent shaded area indicates the statistical standard deviation, referred to as "frictional fluctuations" in this thesis. For the "Abrasive experiments", 5 ml water-based Al_2O_3 abrasive slurry was utilized as interfacial media; for the "well-lubricated" and "unsatisfactory-lubricated experiments", 5 ml FVA 1 was employed; the "LTA (lubricated to abrasive) experiments" began with lubrication using FVA 1 base oil (0-100 m), and at 100 meters, 5 ml of Al_2O_3 slurry were added to simulate the onset of abrasive wear.

In Figure 4.13, the "Abrasive experiments", with only Al_2O_3 slurries as interfacial media, exhibited a consistently higher friction coefficient and more significant frictional fluctuations than the other experiments presented here; the friction coefficient decreased initially before increasing, ranging from 0.11 to 0.21 (frictional fluctuations up to around 0.2). The "well-lubricated experiments" had an average friction coefficient of around 0.03 and frictional fluctuations of around 0.01. In the "unsatisfactory-lubricated experiments", the friction coefficient ranged from 0.3 to 0.7, and the frictional fluctuations were notably more pronounced compared to the "well-lubricated experiments", with a value of approximately 0.13. In the "LTA experiments", during the well-lubricated condition (0-2000 s) with only FVA 1 as the interfacial media, the friction coefficient was observed to be approximately 0.01 and maximum frictional fluctuations of around 0.005; upon adding Al_2O_3 slurry after 2000 s, the friction coefficient sharply increased to around 0.17 and demonstrated maximum frictional fluctuations of around 0.018.

4.3.2   Periodic Frictional Data

Figure 4.14 presents the frictional data from the "LTA experiments"; a 3D visualization of the friction coefficient over time and position is found in Figure 4.14a. The friction coefficient sharply increased after adding Al_2O_3 slurry at 2000 s. Figure 4.14a compares the angle-resolved friction coefficient between the lubricated condition (800-1200 s) and the abrasive wear (2200-2600 s). The friction coefficient in the abrasive wear state ranges from 0.07 to 0.11, whereas the friction coefficient in the lubricated condition ranges from 0.0119 to 0.0125. In Figure 4.14b, the angle-resolved friction coefficient shows a similar trend for lubricated and abrasive wear conditions. Figure 4.14c depicts the 3D visualization for abrasive wear (2200-2600 s) conditions; the plot highlights the periodic fluctuations of the friction coefficient along

the sliding track, with two localized regions (centered around 80° and 210°) exhibiting higher friction coefficients than other regions.
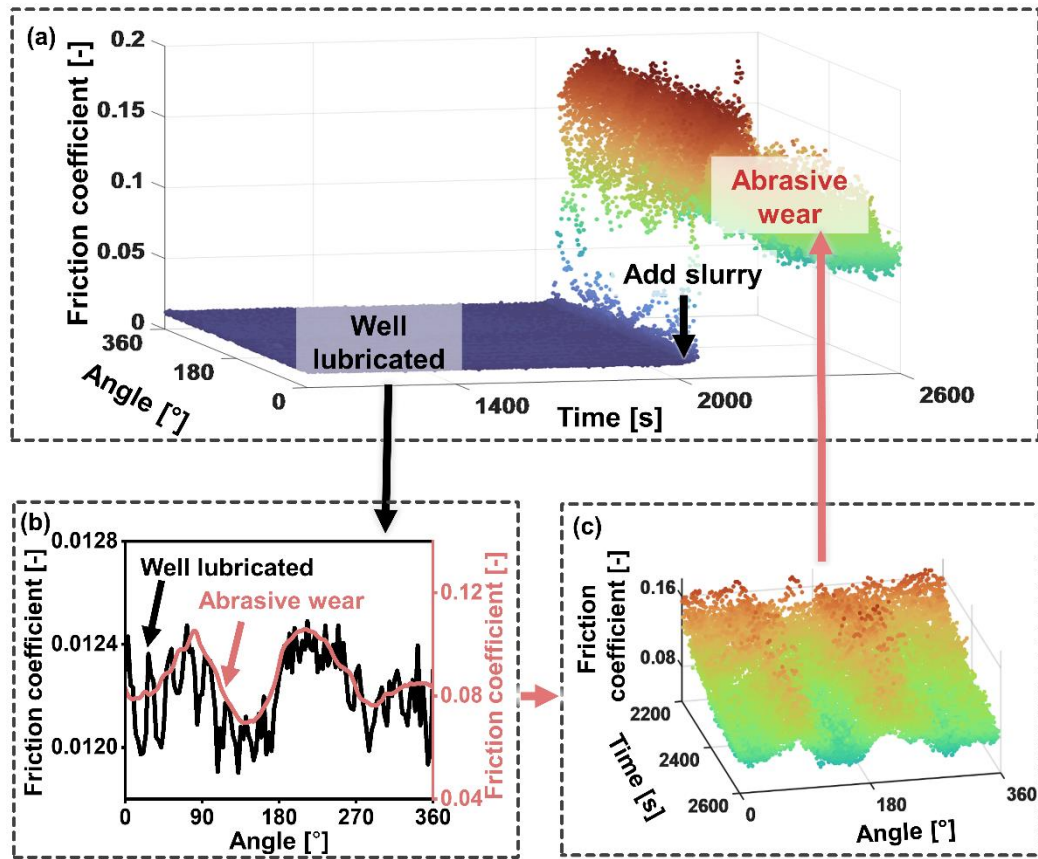
Figure 4.14: Frictional data from "lubricated to abrasive (LTA) experiments": (a) 3D visualization of friction coefficient; (b) angle-resolved friction coefficient at well-lubricated condition (1200-1600 s) and abrasive wear (2200-2600 s); (c) 3D visualization of friction coefficient at abrasive wear (2200-2600 s);

4.3.3   Disk Waviness Profile, Friction Coefficient, and Slope Angle

To investigate the relationship between the disk waviness profile and the friction coefficient, Figure 4.15a compares the angle-resolved friction coefficient for abrasive wear (2200-2600 s) and the disk waviness profile from the "LTA experiments". The frictional fluctuations along the sliding track exhibit a similar trend compared to the disk waviness profile irregularities, although there is a slight shift in the location of the two peaks.
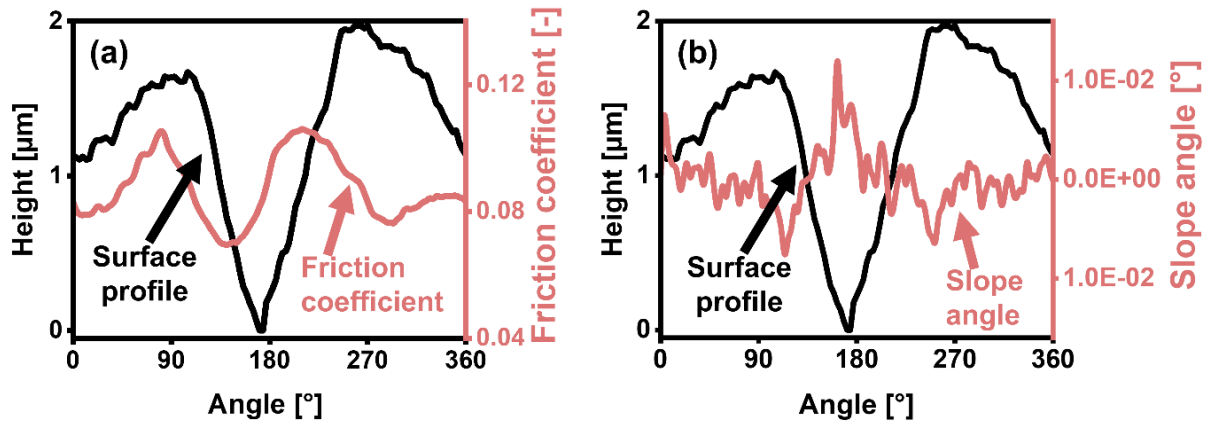
Figure 4.15: (a) The angle-resolved friction coefficient at abrasive wear (2200-2600 s) from the "LTA experiments" was compared with the disk waviness profile; (b) the disk waviness profile from the "LTA experiments" is displayed along with its slope angle, the evaluation of slope angle on disk waviness profile is given in Figure 3.10b.

In Figure 4.15b, the disk waviness profile from the "LTA experiments" is displayed along with its slope angle (the evaluation of the slope angle on the disk waviness profile is given in Figure 3.11b). The slope angle of the disk waviness profile represents the variation in the angle between the front and back contours of each point on the sliding track. The maximum slope angle for the disk in the "LTA experiments" is only approximately 0.012 degrees.

In Figure 4.16, the disk waviness profile is compared to the angle-resolved friction coefficient (0-50 m) of "well-lubricated" and "unsatisfactory-lubricated" experiments and their repeats. The locations of certain peaks in the friction coefficient along the sliding track roughly coincide with the locations of peaks in the disk waviness profile, for example, L3, L4, and L5 in Figure 4.16. However, this alignment does not always occur consistently, for example L1 and L2 in Figure 4.16.
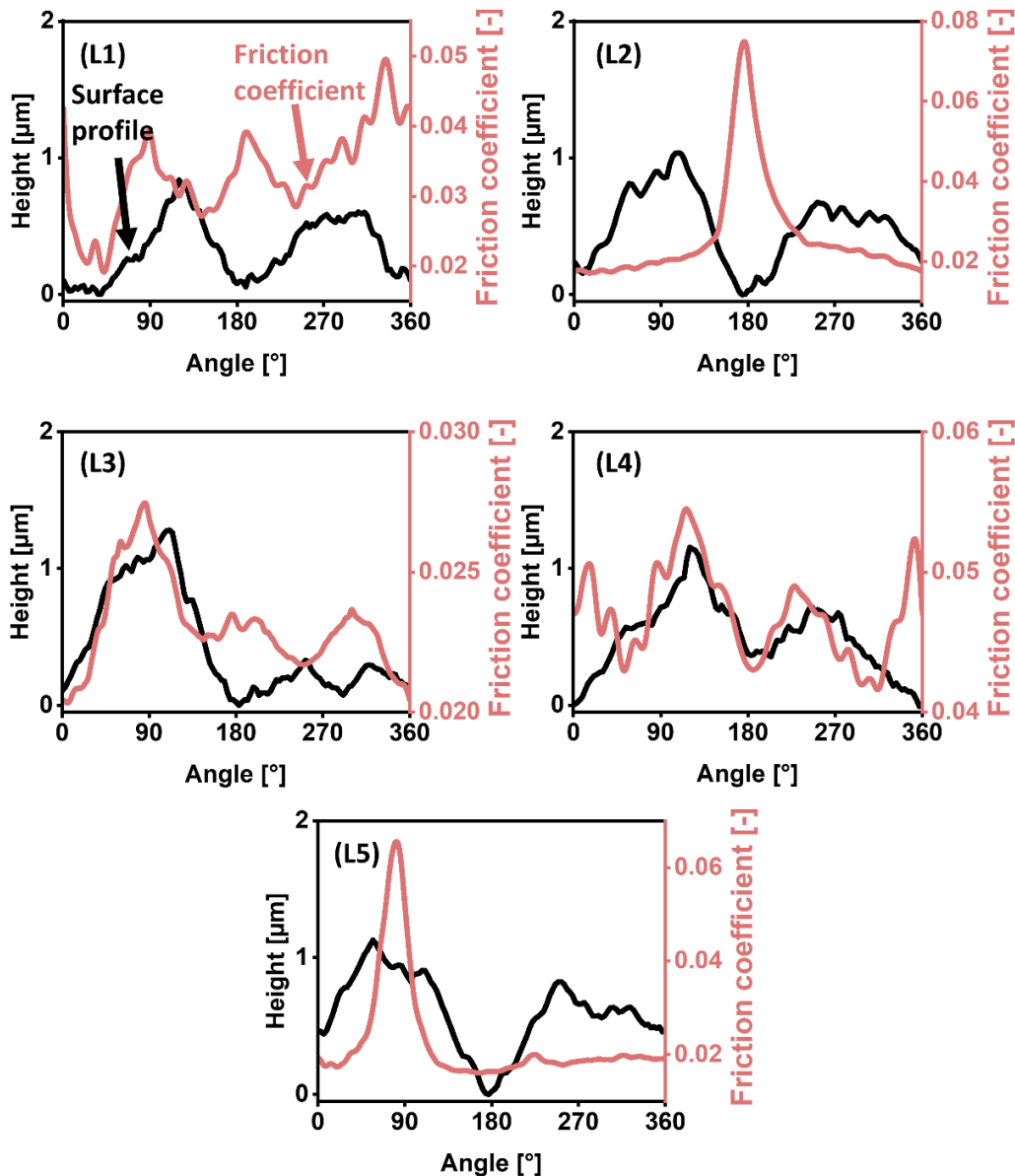
Figure 4.16: Disk waviness profile and angle-resolved friction coefficient (0-50 m) for lubricated experiments, all the experiments were performed with the same settings: (L1) "well-lubricated experiments" corresponding to the data in Figure 4.13; (L2) "unsatisfactory-lubricated experiments" corresponding to the data in Figure 4.13; (L3-L5) repeats of the lubricated experiment.

A similar trend is found for "abrasive experiments" and their repeats in Figure 4.17. All the disks in Figure 4.15-17 were prepared according to the standard outlined in chapter 3.1. **The height difference along the 132 mm sliding track for all disks in Figure 4.15-16 and Figure 4.17 remains within 2 μm, representing about the minimum achievable value in**

our laboratory. However, it can be observed that none of the disks' waviness profiles are

identical to each other; in fact, it can be said that each disk has a unique waviness profile.
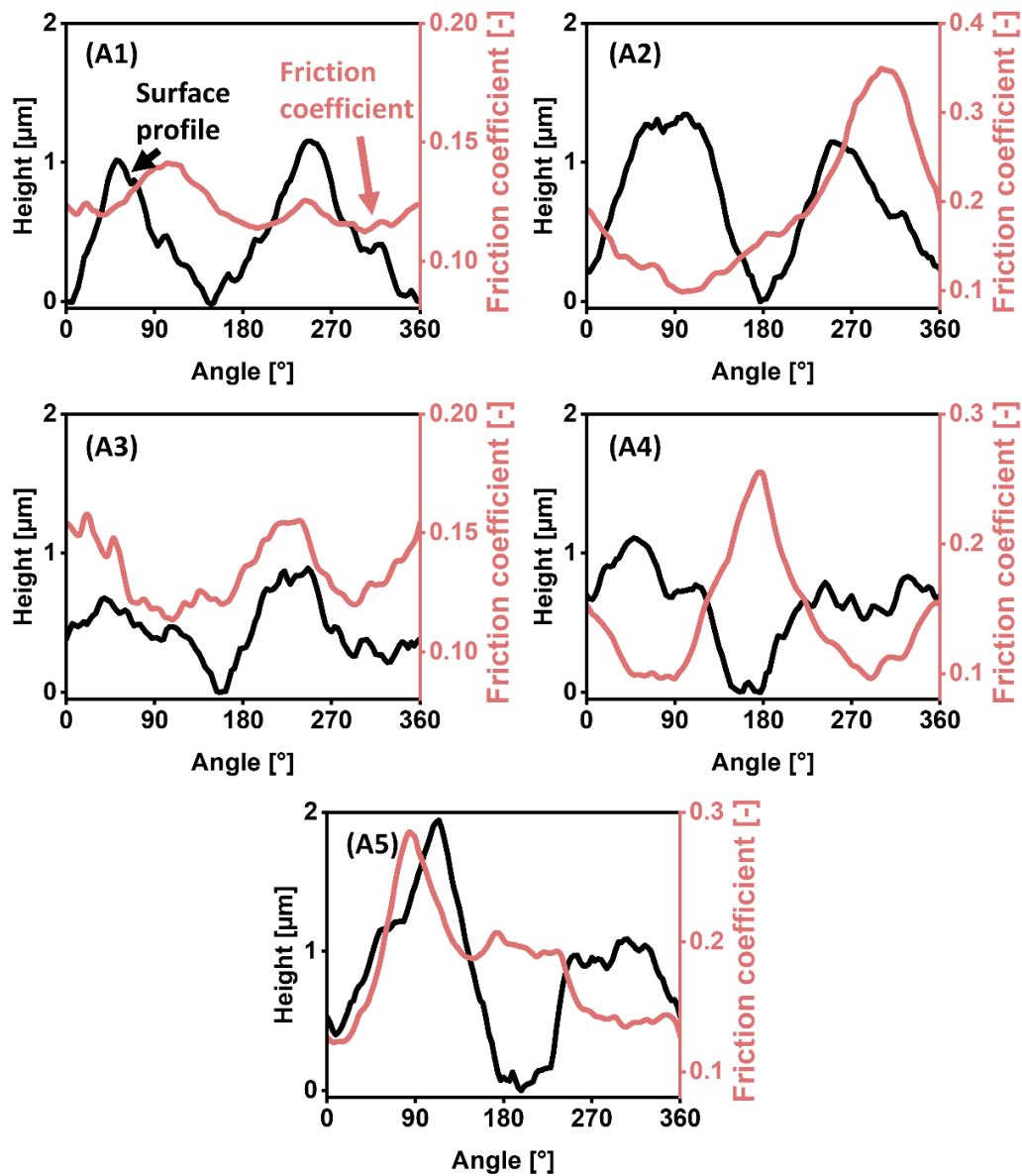
Figure 4.17: Disk waviness profile and angle-resolved friction coefficient (0-50 m) for "abrasive wear experiments"; all experiments were done with the same settings: (A1) abrasive wear experiment corresponding to the data in Figure 4.13; (A2-A5) repeats of "abrasive wear experiments".

4.3.4 Oscillation of the Contacting Surfaces, Friction Coefficient, and Z-score

The oscillation of the contacting surfaces in this thesis arises from the tilt of the disk mounting; evaluation details are shown in chapter 3.4.9. The comparison between the oscillation of the contacting surfaces and the angle-resolved friction coefficient (0-50 m) for "LTA experiments" is given in Figure 4.18. The black curve exhibits a maximum difference of 4 µm, representing the impact of disk mounting tilt and machine vibrations, resulting in a 4 µm height difference during each disk revolution. Consequently, during the tribological contact, the contacting surfaces oscillate in accordance with the black curve, giving rise to what we refer to as the "oscillation of contacting surfaces".
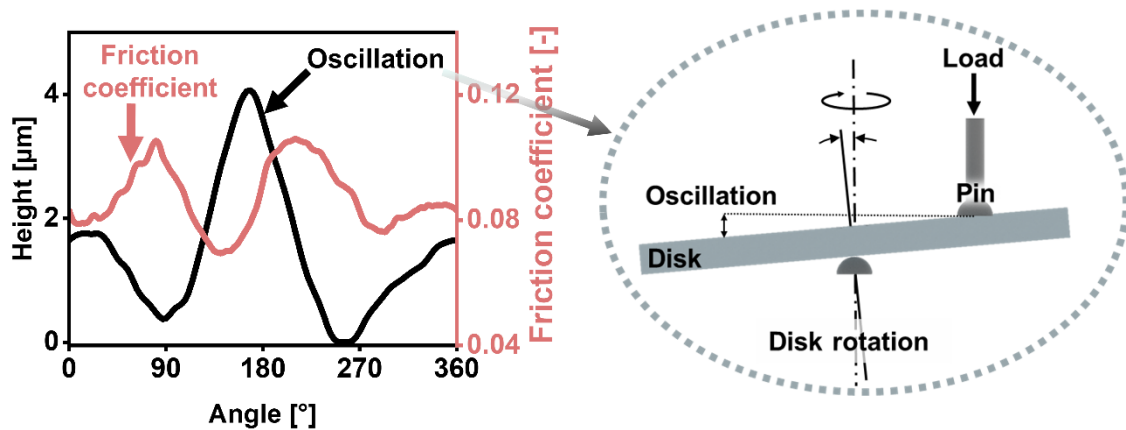
Figure 4.18: The comparison between oscillation of contacting surfaces and angle-resolved friction coefficient (0-50 m) for "LTA experiments", corresponding to the data in Figure 4.15. The black curve exhibits a maximum difference of 4 µm, representing that during tribological contact, surfaces would oscillate with an amplitude of 4 µm. The schematic of oscillation due to mounting tilt is from Figure 3.10.

The comparison between the oscillation of the contacting surfaces and the angle-resolved friction coefficient (0-50 m) of "well-lubricated" and "unsatisfactory-lubricated" experiments is given in Figure 4.19; no direct correlation can be seen.
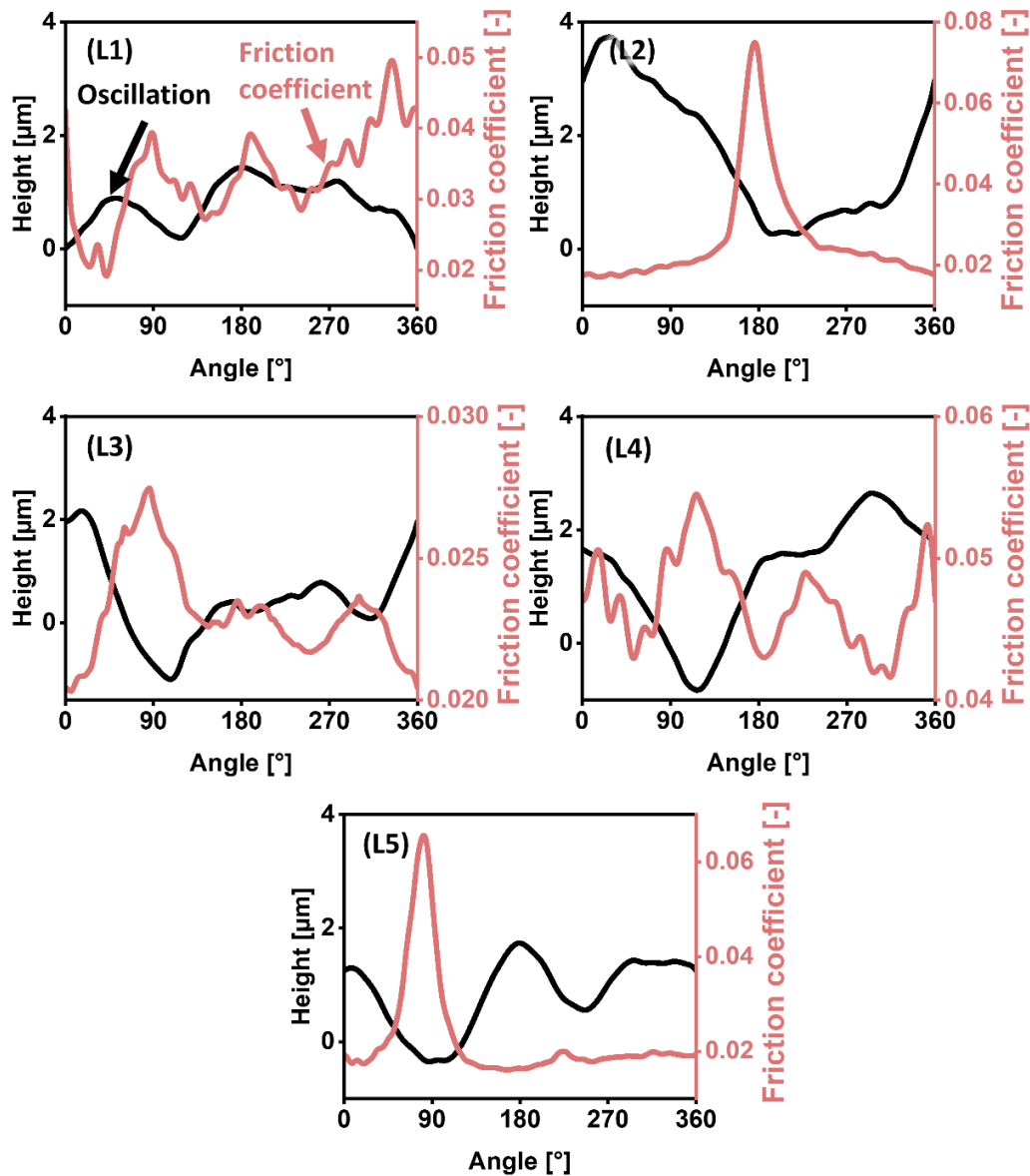
Figure 4.19: Oscillation of the contacting surfaces and angle-resolved friction coefficient (0-50 m) for lubricated experiments, corresponding to the data in Figure 4.16: (L1) "well-lubricated experiments" with corresponding to the data in Figure 4.13; (L2) "unsatisfactory lubricated experiments" with corresponding to the data Figure 4.13; (L3-L4) repeats of "well-lubricated experiments"; (L5) repeats of "unsatisfactory lubricated experiments"

For "abrasive wear experiments" as well as for their replicates in Figure 4.20, no obvious correlation can be seen between the oscillation of the contacting surfaces and the angle-resolved friction coefficient. For all experiments in Figure 4.18-20, the disk mounting followed the same procedure and standard as outlined in chapter 3.2.2. **The total height difference on**

the 132 mm sliding track was also strictly limited to a maximum of 4 μm (the lowest

achievable value within our laboratory). Each individual experiment depicted in

Figure 4.18-20 exhibits its own distinct oscillation pattern.
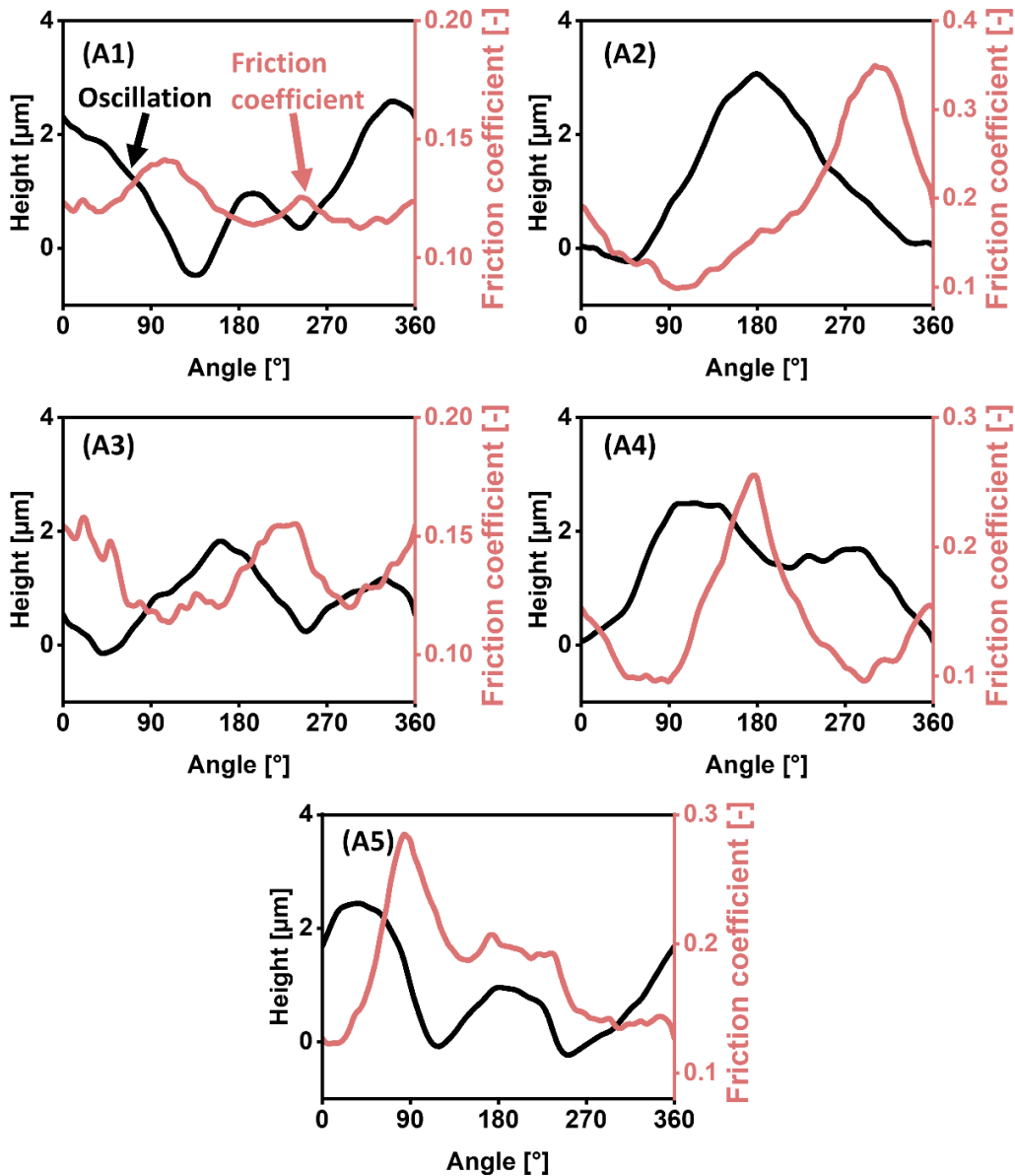
Figure 4.20: Oscillation of the contacting surfaces and angle-resolved friction coefficient (0-50 m) for "abrasive wear experiments", corresponding to the data in Figure 4.17: (A1) corresponding to the data in Figure 4.13; (A2-A5) repeats of "abrasive wear experiments",

To investigate the potential correlation between the oscillation of the contacting surfaces and the friction coefficient, the Z-score of the friction coefficient for each sector along the sliding track (the 132 mm circular sliding track was divided into 120 sectors) was calculated. The computation details of the Z-score can be found in chapter 3.4.11. The Z-score adeptly reflects the extent to which the friction coefficient in each sector along the sliding track deviates from the mean friction force across the entire sliding track. When a sector has a friction coefficient surpassing the average, its Z-score manifests as positive, and this Z-score increases with greater deviations in the friction coefficient.

The Z-score of the friction coefficient for each sector from the eleven experiments in Figure 4.18-20 was calculated, resulting in a total of 1320 Z-scores. Additionally, the slopes of the oscillation curves (oscillation of the contacting surfaces in Figure 4.18-20) for 1320 sectors were also evaluated and then plotted against these Z-scores, as shown in Figure 4.21; the friction coefficient of the sectors that deviates by one standard deviation from the mean (absolute Z-score greater than one) are highlighted in red. In Figure 4.21, within sectors characterized by a positive Z-score, 72% of them display a negative slope of oscillation; in sectors with a negative Z-score, 62% of them show a positive slope of oscillation. Furthermore, when the Z-score exceeds one, 92% of sectors demonstrate a negative slope of oscillation; whereas when the Z-score is less than -1, 93% of sectors display a positive slope of oscillation.
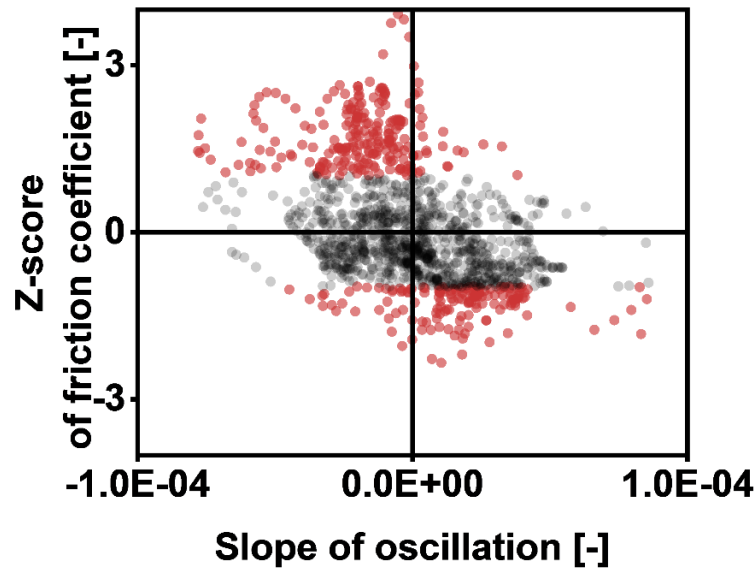
Figure 4.21: Friction coefficient Z-score as a function of oscillation slope, the figure contains 1320 sectors' data from 11 experiments; absolute Z-scores greater than 1 are highlighted with red color. The Z-score adeptly reflects the extent to which the friction coefficient in each sector along the sliding track deviates from the mean friction force across the entire sliding track. When a sector has a friction coefficient surpassing the average, its Z-score manifests as positive, and this Z-score amplifies with greater deviations in friction coefficient.

4.3.5 Worn Surfaces

To reveal the effect of friction on wear, the confocal images of the disks' worn surfaces from the "unsatisfactory-lubricated experiments" are presented in Figure 4.22b+c, along with the corresponding angle-resolved friction coefficient (0-50 m) in Figure 4.22a. It is important to note that the images were taken at the same sliding radius but at different sectors along the sliding track. The results indicate different worn surfaces along the sliding track, as evidenced by abrasive grooves in Figure 4.22b+c. The high friction area at around 180° exhibits more pronounced grooves in the sliding direction (in Figure 4.22c) than the low friction area depicted in Figure 4.22b.
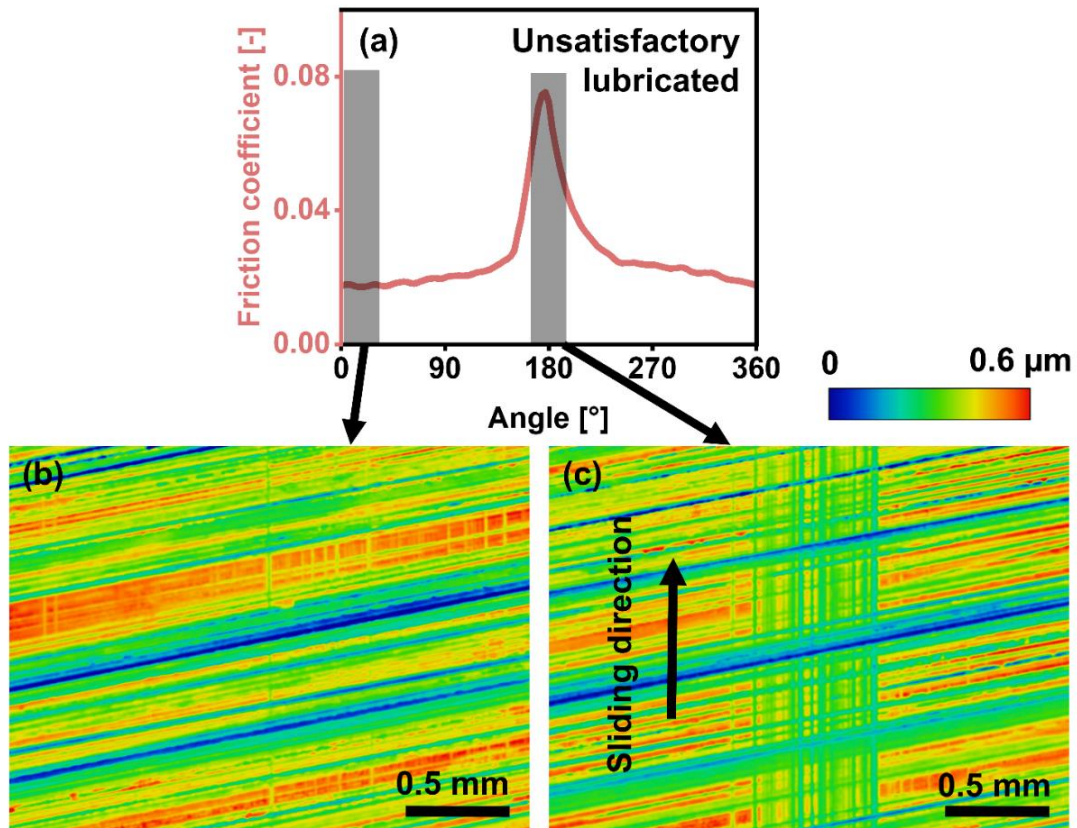
Figure 4.22: (a) angle-resolved friction coefficient for the "unsatisfactory-lubricated experiments"; (b) confocal image of the high friction area around 180°; (b) confocal image of low friction area around 0°. The confocal images in (b) and (c) were taken at the exact same sliding radius.

4.3.6   Time-frequency Analysis

Chapter 4.3.2 showcases the periodic data observed in "LTA experiments", where the friction coefficient undergoes periodic variations over time. To investigate the frequencies within these periodic variations and explore potential correlations with tribological behavior, in Figure 4.23, a time-frequency analysis was conducted on the tribological data acquired from the "LTA experiments" depicted in Figure 4.13. In the spectrogram, the x-axis represents time, and the y-axis represents frequency. The spectrogram visualizes the evolution of different frequency components in the tribological data over time. The color in the spectrogram conveys the power of the signal at different frequencies. The sliding speed in the experiment was 50 mm/s, and

the sliding track covered 132 mm. Consequently, the corresponding frequency of the sliding

speed was 0.38 Hz.
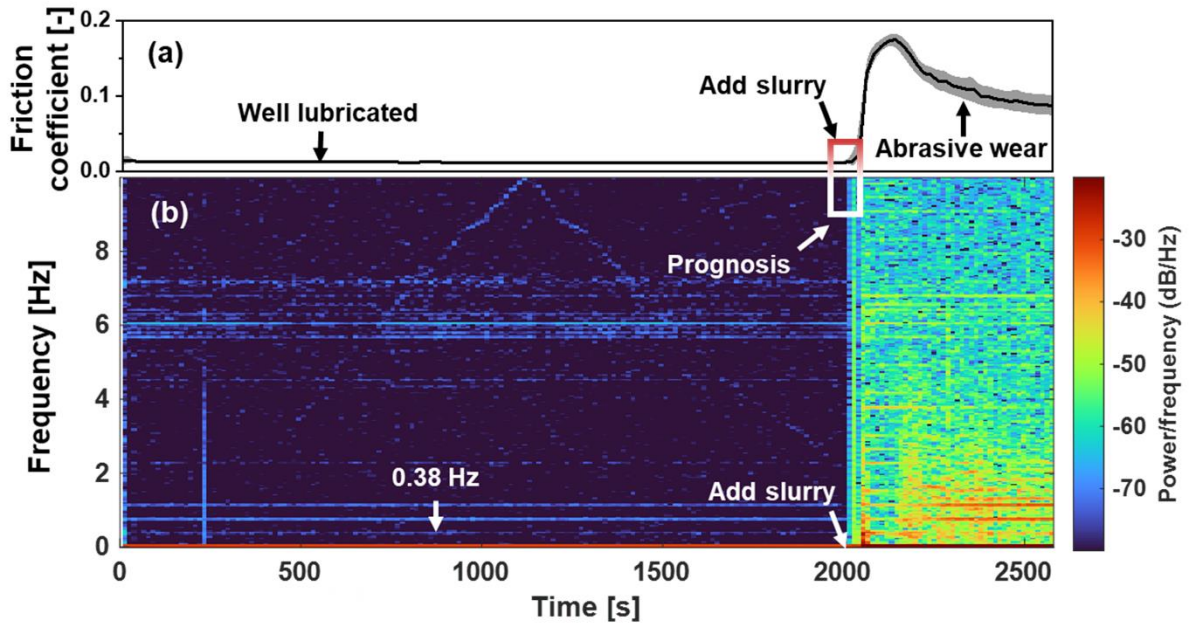
Figure 4.23: Time-frequency analysis of friction coefficient obtained from the "LTA experiments": (a) friction coefficient as a function of time for the "LTA experiments"; (b) spectrogram of friction coefficient. The spectrogram visually shows the evolution of different frequency components in the tribological data over time. The color in a spectrogram conveys the power of the signal at different frequencies.

Figure 4.23a shows the variation of the friction coefficient over time for "LTA experiments".

By applying the short-time Fourier transform (STFT, details are given in chapter 3.4.12) to the

data in Figure 4.23a, a time-frequency spectrogram of the friction coefficient was obtained, as

illustrated in Figure 4.23b. Stable frequency bands are observed from the beginning to around

2000 s, e.g., a natural frequency of 0.38 Hz and a continuous band at around 6 Hz, except for

some noise around 300 s. After adding the abrasive slurry at around 2000 s, the friction

coefficient in Figure 4.23a suddenly increases; discrete frequency bands in Figure 4.23b are

significantly intensified, and a continuous vertical spectrum of the frictional signals is observed immediately after adding the abrasive slurry.

5 Discussion

5.1 Mechanisms of Abrasive Wear

5.1.1 Friction

In the multi-step experiments conducted with the 5 µm slurry as the interfacial medium, a decrease in friction coefficient of around 0.22 was observed with increasing sliding speed (see Figure 4.1), combined with a significant relative variation in film thickness of around 15%. Such speed-induced hydrodynamic effects are common in the literature, whether the interfacial media are oil-based lubricants [121–125] or abrasive slurries [56,57]. At low speeds (50 mm/s – 80 mm/s), the film thickness only changes 1% with increasing speed. The load is mainly carried by particles between the frictional surfaces, so the friction coefficient is only slightly decreasing by around 0.03 with speed in this low speed regime (50 mm/s – 80 mm/s). This is an indication of "boundary lubrication " at low speeds for the multi-step experiments [126,127]. When the sliding speed is higher (200 mm/s – 400 mm/s), a 14% increase in film thickness was measured. This points to "mixed lubrication", where the lubricant film is still thin compared to hydrodynamic lubrication but thicker than in boundary lubrication [18,128,129]. The increasing film thickness can help separate contact asperities and partially carry the tribological load [128,130]. At this point, the load is supported by both particles and the solvent in the slurry, which leads to a significant drop in friction coefficient at high speeds (200 mm/s – 400 mm/s). Similar to previous research using abrasive slurries as an interfacial medium [131,132], pure "hydrodynamic lubrication" – a full separation of contacting surfaces resulting in very low friction coefficients – is not observed in our experiments.

For the multi-step experiments with the 13 µm slurry, both friction coefficient and film thickness did not change much with sliding speed, see Figure 4.1. The initial separation between the frictional surfaces is 13 µm when working with the 13 µm slurry as interfacial medium, which is 2.6 times the separation for the 5 µm slurry. On the one hand, the large initial film thickness will make the speed-induced thickness change negligible; on the other hand, the wide gap will also make it difficult to build up enough hydrodynamic pressure to carry the tribological load. This is why the gap between the frictional surfaces remains rather constant. With speed increasing from 50 mm/s to 400 mm/s, this study observes only little change in film thickness and friction coefficient during the multi-step experiments. This demonstrates that particle size plays an essential role under lubricated conditions. Larger particles between frictional surfaces hinder the generation of sufficient hydrodynamic pressure to separate the two contacting bodies.

5.1.2   Wear Mechanisms

In Figure 4.3 and Figure 4.4, wear analyses were performed for the samples utilized in constant speed experiments and the 5 µm slurry. As the experiments were carried out in bath conditions for the slurries, there were always sufficient particles between the frictional surfaces. The size of the particles in the slurry (5 µm) is a factor of one order of magnitude higher than the flatness (pin ≤ 0.6 µm, disk ≤ 1 µm) and roughness (pin: $R_a = 0.02$ to 0.04 µm, disk: $R_a = 0.08$ to 0.12 µm) of the frictional surfaces, which indicates that a solid contact was formed primarily between particles and sample surfaces. In other words, there was no direct tribological contact between the pin and the disk. The indents and grooves on the worn surfaces (Figure 4.3 and Figure 4.4) most likely were generated by the particles. The results of the SEM examinations in Figure 4.3 show that, from the beginning (10 m) to the end (846 m) of the tribological experiments, deeper grooves are observed for the 50 mm/s experiments (Figure 4.3a-c) and

Figure 4.4a-c)) and more indents appear on the surfaces for the 400 mm/s experiments (Figure 4.3d-f) and (Figure 4.4d-f). The dependence of the wear mechanisms on the sliding speeds is clarified by using the model from Williams and Hyncica. This model illustrates the transition from sliding to rolling to be associated with a critical ratio d/h, where d is the particle size and h is the gap between pin and disk. In their work, an increase in particle size or decrease in film thickness led to more particles sliding on the surface, which resulted in the generation of grooves on the worn surface. In contrast, a small ratio of d/h allows particles to roll or tumble between the surfaces, associated with characteristic indentations on the surfaces showing slight directionality. In our experiments, the particle size d is constant and narrowly distributed (see Figure 3.2). A speed-induced hydrodynamic effect determines the film thickness h ($h = d+\Delta h$).

Based on the results presented in Figure 4.1, the increase in film thickness reaches values up to 14% when the sliding speed increases from 50 mm/s to 400 mm/s. The large film thickness at 400 mm/s allows more particles to roll between the pin and the disk (in Figure 5.1a), while at 50 mm/s particles are more inclined to cut or groove (Figure 5.1d). This phenomenon is consistent with the literature's description of the transition from two-body abrasion to three-body abrasion [16,39] or grooving abrasion to rolling abrasion [133]. An increase in speed (50 mm/s to 400 mm/s) can lead to an increase in film thickness and finally change how the particles move through the contact (see schematics in Figure 5.1c+d).
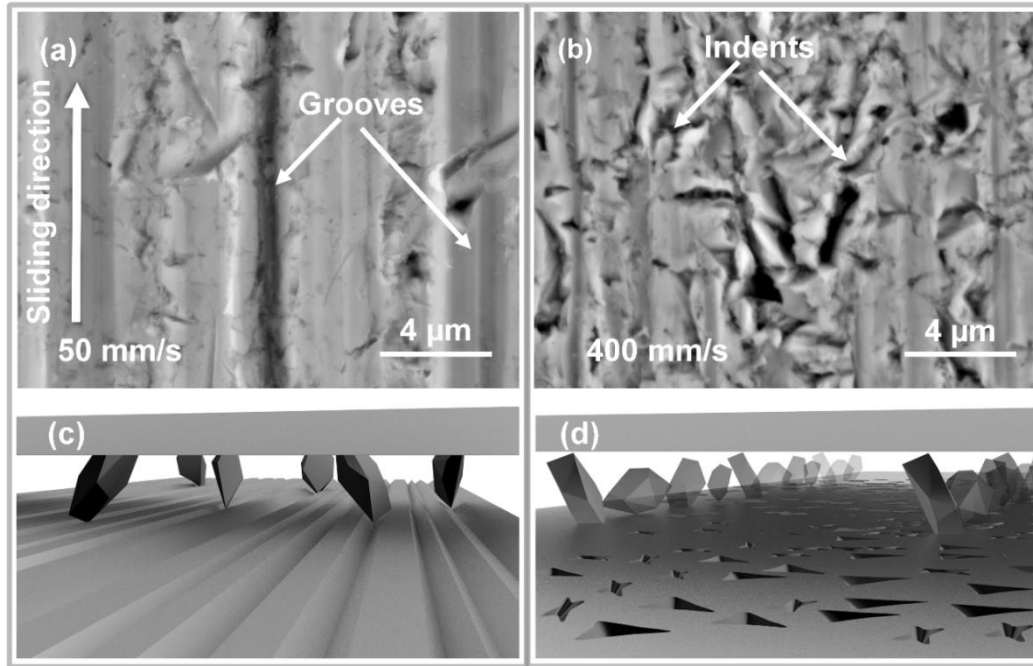
Figure 5.1: Two distinct worn surfaces generated by particles in different kinematic states and their schematics: (a) Heavily grooved surface at 50 mm/s by two-body abrasion; (b) The scattered indented surface at 400 mm/s by three-body abrasion; (c) Schematic of two-body abrasion in the lubricated contact; (d) Schematic of three-body abrasion in the lubricated contact. From [120] with permission.

Another observation further strengthens this hypothesis: In several SEM images, a periodic pattern of indents was found on the samples' surfaces after high speed (400 mm/s) experiments. Figure 5.2a shows a SEM image of a disk's surface after 846 m of sliding at 400 mm/s. Here, two distinctly different shapes of indents alternately appear along the sliding direction. As shown in the schematic of a single particle indentation process (Figure 5.2b), it is easy to imagine particles with large aspect ratios, or that are less sharp in a specific direction, that would create such periodic patterns of indents. Although the typical worn surface of three-body abrasion has been widely studied [44,134], such a trajectory of an individual rolling particle was seldom reported. The observation in Figure 5.2a provides strong evidence suggesting that the indentations on the abrasive worn surface are likely generated by the rolling of abrasive particles, indicative of three-body abrasion.
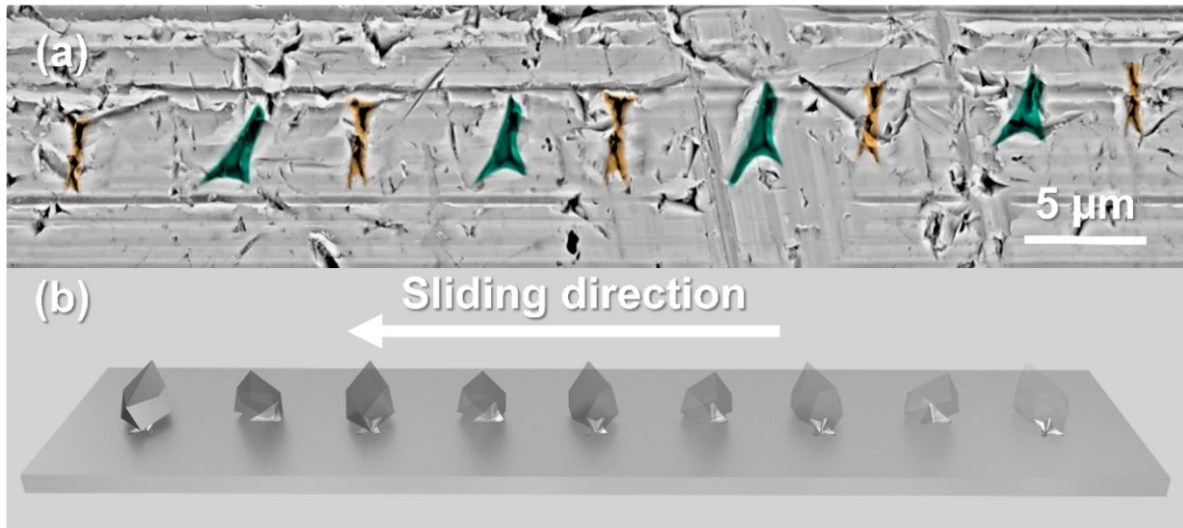
Figure 5.2: Periodic pattern of indents: (a) SEM image of a disk after 50 m of sliding at 400 mm/s, a periodic pattern of indents is observed; (b) Schematic of periodic indentation generation in Figure 5.2a, a single particle rolls along the sliding direction. From [120] with permission.

To understand the processes behind such changes in wear mechanisms further, cross-sectional investigations of the tribologically deformed subsurface microstructures were performed (Figure 4.5). A cross-section of the worn surface at 50 mm/s (Figure 4.5a) shows no recognizable subsurface deformation when the sliding distance is 50 m (Figure 4.5a). Only a few subsurface cracks are observed even if the sliding distance is at its maximum value of 846 m (Figure 4.5b). The limited amount of subsurface cracks (highlighted with an arrow in Figure 4.5b inside the groove might be the result of small particles that were able to roll inside the groove [135]. Perceptible ridges in Figure 4.5a+b were formed by the displacement of material due to plastic deformation [136,137]. The predominant wear mechanism at 50 mm/s is two-body abrasion, and the material is removed from the contact by microcutting and microploughing.

In contrast to the cross-sections at 50 mm/s, a considerable amount of cracks is observed already at the beginning of the tests at 400 mm/s and for 50 m of sliding (Figure 4.5c). As the

sliding distance increases to 846 m, a very high defect density in the subsurface material is observed at a depth of around 200 nm to 650 nm. When the sharp edges of the particles (see Figure 3.2b) indent the surface during the rolling process (Figure 4.5d), each contact can be interpreted as an indentation. Based on earlier research [138–142], such sharp indentation generates a localized plastic deformation zone and material displacement beneath the indentation contact. Lots of particles rolling between the contact's gap might result in cyclic loading and unloading of the surface, creating a series of closely spaced indentations and fatigue. As shown in Figure 4.5d, a period of repeated elastic-plastic loading would certainly cause microstructural changes [143–146] together with cyclic softening or hardening, leading to crack formation and propagation in the plastic deformation zone below or at the surface, which eventually can lead to surface fatigue. The indented surface along with the fractured subsurface, are very similar to what previous researchers have observed [16,36,147–151], who also noted surface fatigue. Since subsurface cracks occurred already at the early stages (50 m of sliding), surface fatigue might make the materials vulnerable to removal during subsequent impacts. As a consequence, with particles' kinematics changed due to the speed induced hydrodynamic effect, surface fatigue might be a determinant factor for the wear at 400 mm/s.

A reference experiment was performed using the 13 µm slurry at 400 mm/s. This experiment aimed to demonstrate that subsurface cracks are not caused by high sliding speeds (400 mm/s) but rather by surface fatigue resulting from particle indentation in three-body abrasion. Here, the tribological system cannot benefit from hydrodynamic pressure because of the big particle size in the slurry (see Figure 4.1), so the dominant wear mechanism is two-body abrasion in Figure 5.3a. The subsurface in Figure 5.3b only shows a few subsurface cracks.
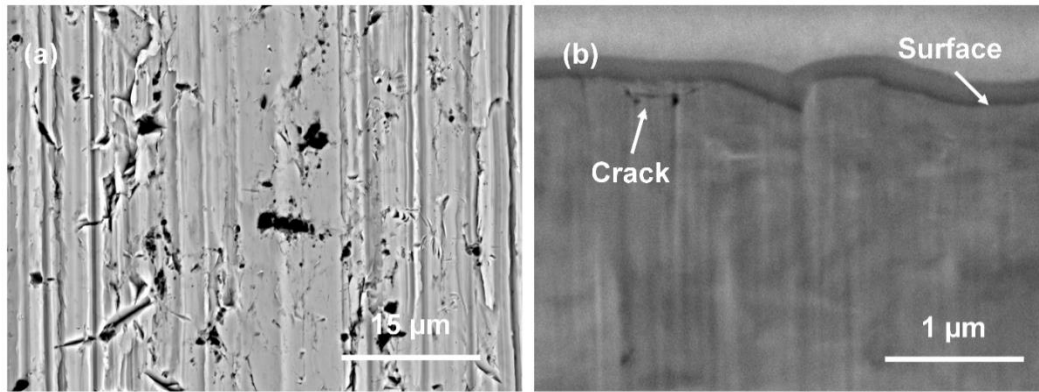
Figure 5.3: Pin after testing with the 13 µm slurry at 400 mm/s: (a) SEM image of the worn surface; (b) Cross-sectional SEM image of the worn surface, only one crack is overserved. From [120] with permission.

5.1.3   Wear

To the best of our knowledge, the majority of published research reported that three-body abrasion generates less wear compared to two-body abrasion [16,32,34,36,39,41,43,44,134,152]. However, the wear results in Figure 4.2 have at least two aspects which are not easy to grasp: First, the total amount of wear for the high speed (400 mm/s, three-body abrasion) and the low speed (50 mm/s, two-body abrasion) experiments is almost identical; while, second, the wear distribution between pin and disk is inverted (see Figure 4.2b).

As stated in the literature, abrasion of a metal involves a certain minimum strain energy sufficient to saturate the material's capacity for work hardening under tribological loading [153]. This energy, for some metals at least, happens to be close to the melting energy. Therefore, an energetic approach might be an effective way to explain our wear results [154]. The dissipated energy E in a tribological contact is calculated as the work done by the frictional force F. For each sliding distance Δx, the dissipated energy ΔE can be calculated following Equation (5.1).

$$\Delta E = \int\limits_{0}^{\Delta x} F \, dx \tag{5.1}$$

$$P = \frac{E}{t} \tag{5.2}$$

The total dissipated energy E for a sliding distance of 846 m in the constant speed experiments is calculated by following Equation (5.1). Then, the frictional power P is calculated from E and the testing time t, as shown in Equation (5.2).

Table 2: Wear results for experiments with the 5 µm slurry at constant speeds after a sliding distance of 846 m. Total wear refers to wear from both pin and disk. Dissipated energy and frictional power are calculated using Equation (5.1) and Equation (5.2), respectively. From [120] with permission.

Speed (mm/s)	Total wear (mg)	Dissipated energy (J)	Frictional power (mW)
50	3.34	447	26.4
400	3.56	170	80.6

The results for the dissipated energy and the frictional power for the constant speeds experiments after 846 m of sliding are presented in Table 2. Due to a hydrodynamic effect, the dissipated energy decreases from 447 J at 50 mm/s to 170 J at 400 mm/s. However, if the experiments' run times are taken into account, the frictional power at 400 mm/s is three times the one at 50 mm/s. The combination of high frictional power and fatigued subsurface material might exacerbate the wear on the frictional surfaces at 400 mm/s, causing the total amount of wear observed after sliding at 400 m/s to be almost the same as after sliding at 50 mm/s – despite the lower friction coefficient. Frictional power – or the rate of energy dissipation – appears to play a key role in the generation of abrasive wear during abrasive experiments.

Another question that remains is why at 400 mm/s the wear of the pin increases and the wear of the disk decreases compared to experiments at 50 mm/s. As discussed above, surface fatigue generated by indentations is an essential factor for the wear performance during the experiments at higher speeds. Possibly, the contact area A could play an essential role, as different indent densities would induce variable levels of subsurface deformation. The contact area of the pin has a 7.33 mm diameter circular shape, maintaining continuous tribological contact with the disk. In contrast, the disk's contact area has a 132 mm circular diameter sliding track, where only the region in contact with the pin has tribological interactions at each point in time. Thus, the dissipated power density ρ might be an important parameter when it comes to finding an explanation for the different reactions of pin and disk to a speed-induced change of wear mechanism, as it has previously already been used to compare tribological pairs with different contact areas [155]. The dissipated power density ρ is defined as the ratio between the frictional power and the contact area A:

$$\rho = \frac{P}{A} \tag{5.3}$$

For our pin-on-disk experiments, the pins' contact area is in permanent contact, while any given point on the disk is only in intermittent contact. The disks' contact area is almost 23 times that of the pins', which means the dissipated power density for the pin is as well higher than that of the disk. When – as assumed – surface fatigue dominates the wear generation at 400 mm/s, a high dissipated power density will most likely result in more severe wear conditions for the pin when compared to experiments run at 50 mm/s — resulting in a higher material loss due to fatigue. Contrarily to this effect, the disks' wear decreases at 400 mm/s compared to 50 mm/s as the dissipated power density is not sufficient to cause a completely fatigued surface on the disk.

This line of thinking can not only be supported by the fact that in Figure 4.3f, a more severely fatigued surface is observed than in Figure 4.4f, but also by a cross-sectional SEM image of the disk after 846 m at 400 mm/s (Figure 5.4), where fewer cracks are observed as compared with the pin (see Figure 4.5).
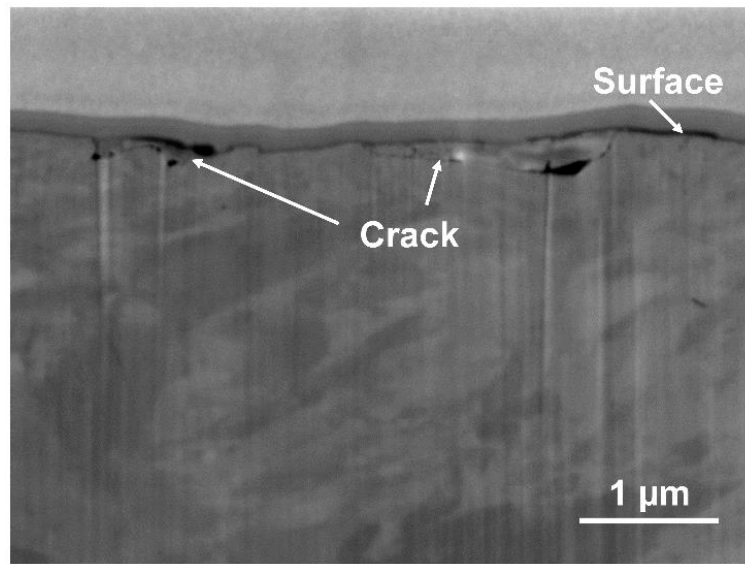
Figure 5.4: Cross-sectional SEM image of the disk after testing for 846 m at 400 mm/s; few cracks can be observed. From [120] with permission.

Despite having unraveled the mechanisms of abrasive wear, some of our findings might still have puzzling aspects. Specifically, the multi-step speed experiments presented in Figure 4.1 raise questions about why the friction coefficient for the 13 µm slurry remains highly stable with minimal fluctuations at all speeds, while the 5 µm slurry experiments exhibit significant fluctuations in friction coefficient. Another interesting trend is in the constant speed experiments with the 5 µm slurry, as shown in Figure 4.2: The friction coefficient at 400 mm/s displays lower fluctuations than that at 50 mm/s. The following section will embark on shedding light on these aspects.

5.2 Waviness Affects Friction and Abrasive Wear

In line with previous reports [2,4,63], frictional fluctuations also occur with abrasive wear in our data (in Figure 4.1, Figure 4.2, and Figure 4.7). In this section, the reason for the friction coefficient fluctuations is addressed. This is followed by a direct comparison between the distribution of the friction coefficient along the disk sliding track with the roughness distribution, waviness profile, and wear.

To investigate the influence of waviness on abrasive wear, four experimental setups were designed, denoted by abbreviations: 5_S, 13_S, 13_L, and 5_S_50. Here, 5 and 13 correspond to the abrasive particle size, specifically 5 µm and 13 µm. The letter "S" represents the disks with a small waviness ($W_t \leq 2$ µm), while "L" represents the disks with a large waviness ($W_t \geq 7$ µm).

5.2.1   Frictional Fluctuations

In Figure 4.8, the tribological data of the experiments is divided into eight zones; the results strongly suggested that fluctuations in friction coefficient for 5_S, 5_S_50, and 13_L are due to inconstant friction coefficient along the sliding track. Some areas on the disk obviously lead to higher friction, for example, zone 3 on 5_S; some areas result in a locally lower friction, e.g., zones 7 and 8 on 5_S. The inconstant friction coefficient along the sliding track has not been a focus of attention in most tribological studies, and only a few publications reported such a phenomenon, and these that do, do not attempt to speculate about the root cause for this phenomenon. [111,156,157].

However, dividing the tribological data from the experiments into eight zones is insufficient for identifying the reasons behind the inconsistent friction coefficient along the sliding track.

To elucidate what could be the reason for inconstant friction along the sliding track for tests with the 5 µm slurry and small waviness (5_S), in Figure 5.5, the average friction coefficient along the entire disk's wear track (in Figure 4.8) is compared to the roughness distribution and the waviness profile (in Figure 4.6), respectively. The entire sliding track (360°) is divided equally into 120 segments when evaluating the average friction coefficient, and the average friction coefficient of each segment is the average for the next 3°. e.g., the friction coefficient at x = 0° (as plotted) is the average friction coefficient between 0° and 3°.
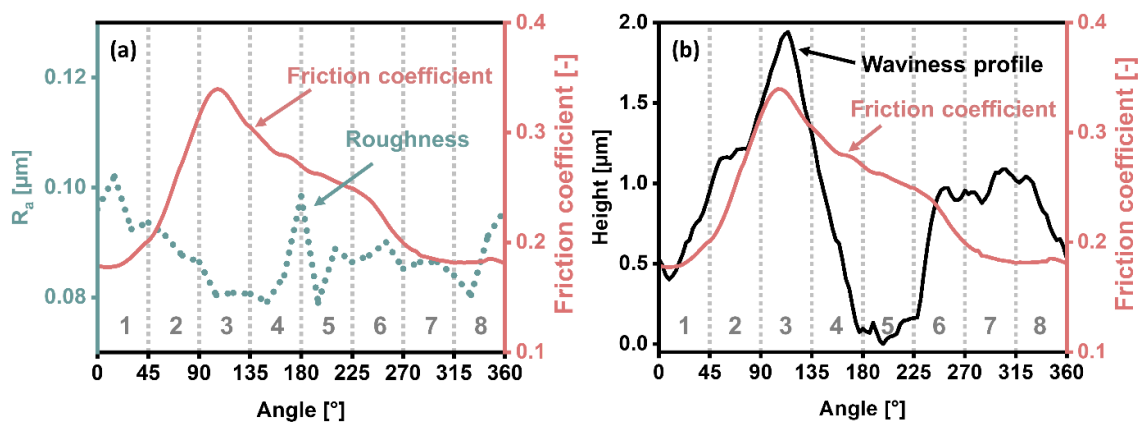
Figure 5.5: Comparing friction coefficient (0-846 m, in Figure 4.8) with roughness distribution and waviness profile (in Figure 4.6) for 5_S, tested with the 5 µm slurry and small waviness: (a) friction coefficient & roughness distribution; (b) friction coefficient & waviness profile. From [103] with permission.

For 5_S (Figure 5.5a), there is no visible correlation between friction coefficient (0-846 m) and roughness. By contrast, there is a partial correlation between friction coefficient (0-846 m) and disk waviness profile in Figure 5.5b. The friction coefficient is the highest where the waviness profile has maximum height. **A "hill" of around 2 µm height increases the friction coefficient by 91%.** The impact of these "2 µm" is astonishing, given our utmost efforts to control waviness, maintaining it at less than 2 µm on such a long sliding track (132 mm). Even within the highly precise semiconductor manufacturing, as exemplified by the 7 nm node lithography process, the tolerated height difference on a 300 mm wafer is merely below 5 µm

[158]. So, if a 132 mm sliding track has a height difference of only 2 µm, it is typically considered "flat" in tribology. However, this thesis has discovered that even such a tiny difference can dominate tribological behavior, which is a point often overlooked by tribologists and deserves broader attention in the future. Similar results are obtained when testing with a 5 µm slurry and small waviness for a short distance (5_S_50 in Figure 5.6) and a 13 µm slurry and a large waviness (13_L in Figure 5.6).
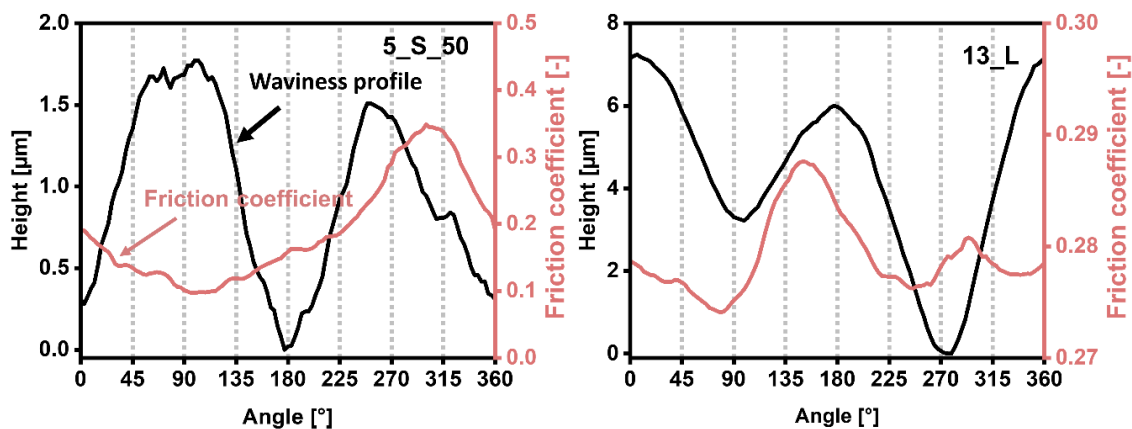
Figure 5.6: Comparing the waviness profile in Figure 4.6 and friction coefficient (0-846 m) in Figure 4.8 for 5_S_50 and 13_L: 5_S_50, tested with the 5 µm slurry and small waviness; 13_L tested with the 13 µm slurry and large waviness. From [103] with permission.

When making use of disks with a small waviness ($W_t \leq 2$ µm), fluctuations in friction coefficient (of around 0.2) were only observed for experiments with the 5 µm slurry (5_S and 5_S_50 in Figure 4.7), while friction coefficient fluctuations in experiments with the 13 µm slurry (13_S in Figure 4.7) are less than 0.05.

The question, therefore, arises whether this behavior is caused by the fact that smaller slurry particles are more sensitive to the waviness profile, thereby leading to higher fluctuations in friction coefficient. With this question in mind, base bodies (e.g., 13_L) with intentionally higher waviness ($W_t = 7.24$ µm) were tested with the 13 µm slurry. By comparing the average

friction coefficient along the sliding track and the waviness profile for the experiments conducted with the 13 µm slurry and increased waviness (13_L), one can infer that at locations on the disks where the waviness profile shows a positive slope (of the "hills"), the friction coefficient also increases. When W_t is increased from 1.56 µm (13_S) to 7.24 µm (13_L), the base bodies' waviness profile shows an influence on the friction behavior when tested with the 13 µm slurry. This underlines that for abrasive conditions with small abrasive particles (5 µm slurry), the waviness profile has a much more pronounced influence compared to systems where the abrasive particles are larger (13 µm slurry).

The above results and discussion sheds light on the two questions raised at the end of chapter 5.1 regarding the results in Figure 4.1 and Figure 4.2, "why the friction coefficient for the 13 µm slurry remains highly stable with minimal fluctuations at all speeds that have been tested, while the 5 µm slurry exhibits significant fluctuations, especially at lower speeds?"

- When using small abrasive particles (5 µm slurry), the frictional fluctuations are more pronounced than with the 13 µm slurry. This is attributed to the stronger influence of the waviness profile for small abrasive particles. Particle size determines the separation distance of the contact bodies. As the particle size increases, a relatively larger separation distance causes the smaller irregularities on the surface asperities to have a less pronounced impact on the tribological properties.

- As for the 5 µm slurry, at low speeds (50 mm/s – 80 mm/s), the film thickness does not change much with increasing speed. The load is carried by particles between the frictional surfaces, indicating boundary lubrication-like conditions, making the influence of disk surface topography (waviness) on the friction behavior particularly significant, resulting in large frictional fluctuations at low speeds. However, at high speeds (200 mm/s – 400 mm/s), a 14% increase in film thickness aids the separation of

the contacting asperities and partially carries the tribological load (as shown in Figure 4.1 and discussed in section 5.1.1). Therefore, using a 5 µm slurry as an interfacial medium, the frictional fluctuations significantly decrease at higher speeds.

5.2.2 Wear

In most cases, friction has a strong influence on wear during tribological loading [1]; consequently, frictional fluctuations are also expected to influence wear. In Figure 4.10, the wear of 5_S (tested with the 5 µm slurry and a small disk waviness) and 13_L (tested with the 13 µm slurry and a large disk waviness) is more uneven than that of 13_S (tested with the 13 µm slurry and a small disk waviness). To elucidate the relationship between fluctuations in friction coefficient and uneven wear along the sliding track, the wear-induced height loss along the sliding track (Figure 4.10) is directly compared to the friction coefficient for 5_S, 13_S, and 13_L (Figure 4.8) in Figure 5.7.
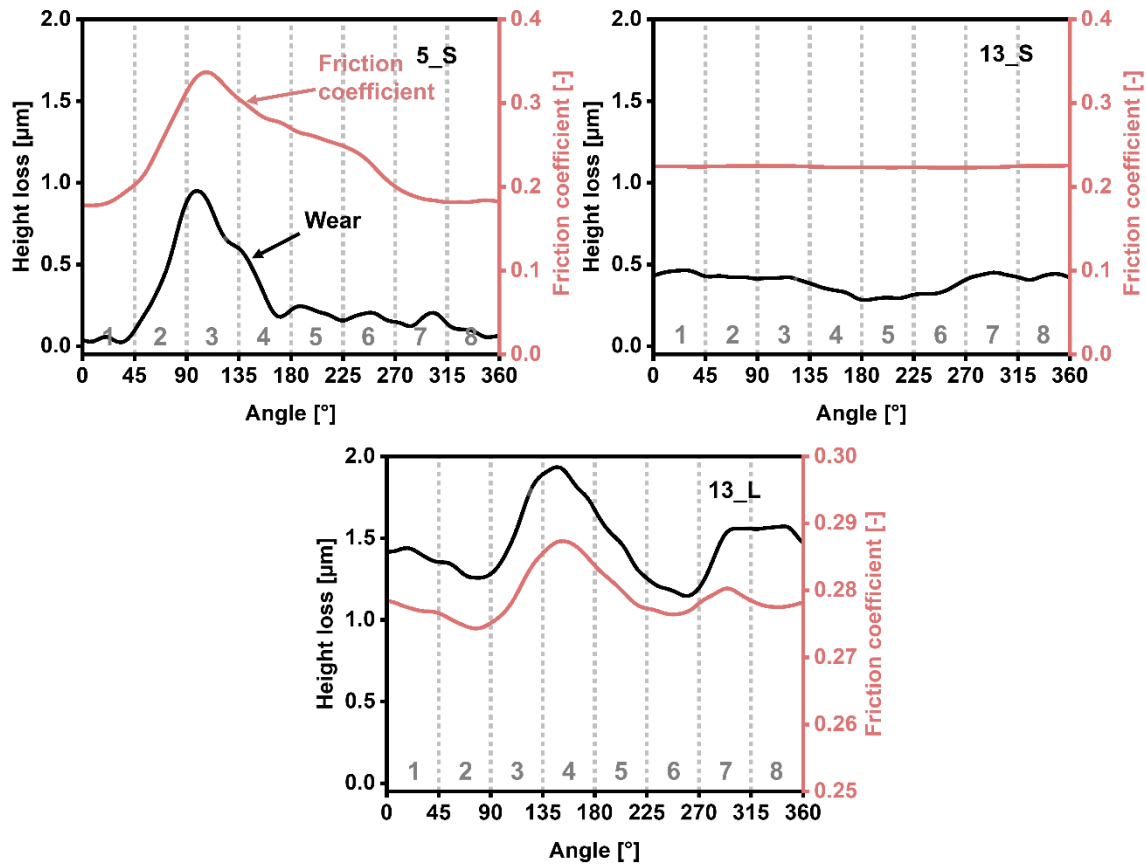
Figure 5.7: Comparing friction coefficient (0-846 m, in Figure 4.8) with wear-induced height loss (from Figure 4.10) for 5_S, tested with the 5 µm slurry and small waviness; 13_S, tested with the 13 µm slurry and small waviness; 13_L, tested with the 13 µm slurry and large waviness. From [103] with permission.

For 5_S and 13_L, it is apparent that most of the wear occurred in the areas with the highest friction coefficient. There is a very clear and close correlation between the friction coefficient and the height loss in both cases. In contrast, for 13_S, the friction coefficient is almost constant over the entire sliding radius, and the same can – with a grain of salt – also be said about the height loss. These results indicate that fluctuations in friction, together with increased base body waviness, correlate with uneven wear along the sliding track.

In Figure 5.8, the friction coefficient for the last 50 m of the tests (790-840 m, Figure 4.8) and the roughness R_a along the sliding track after the test (Figure 4.12) are compared for 5_S and 13_L. A clear correlation is seen between in-track roughness distribution and friction

coefficient. This data demonstrates the intricate feedback mechanisms between waviness, wear, friction coefficient, and surface roughness. The SEM images of the worn surfaces presented in Figure 4.11 also support this line of thought. For experiments tested with a 5 µm slurry and small waviness (5_S), the portion of the disks with a higher friction coefficient (around 110°) shows more distinct grooves than the parts of the disks with a lower average friction coefficient (around 0°), which also correlates with the roughness profile presented in Figure 5.8. This difference in surface morphology is observed from early on in the tests (5_S_50, 50 m, Figure 4.11b) and until the end of the experiments (5_S, 846 m, Figure 4.11c). This indicates that the influence of friction on the worn surface exists from the very beginning and persists until the end of the experiment.
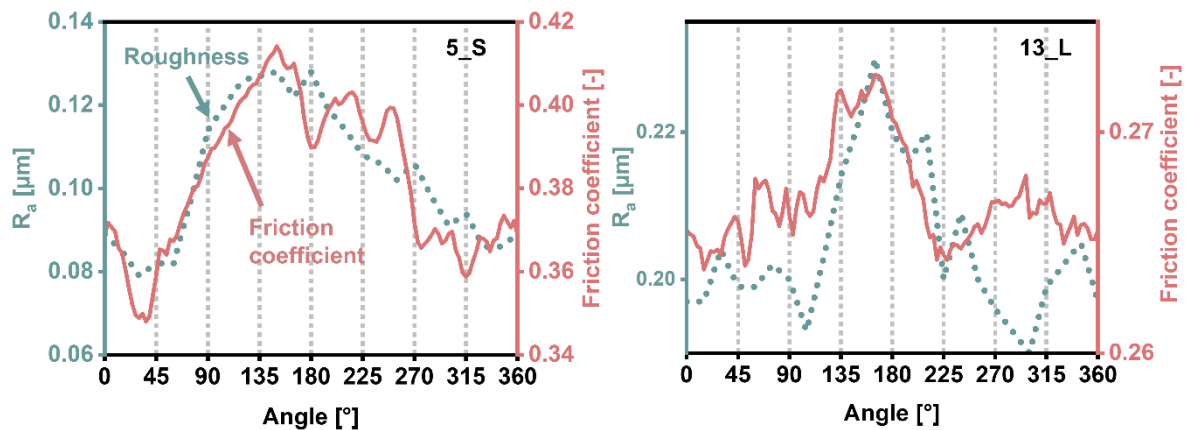
Figure 5.8: Comparing roughness R_a along the sliding track after test (Figure 4.12) and friction coefficient in the later phases (790 - 840 m, in Figure 4.8): 5_S, tested with the 5 µm slurry and small waviness; 13_L, tested with the 13 µm slurry and large waviness. From [103] with permission.

In contrast and owing to the stable friction coefficient of experiments tested with the 13 µm slurry and small waviness (13_S), the worn surface in different areas shows very little difference, as shown in Figure 5.9. For 13_L, the worn surfaces in high friction and low friction zones again do not show significant differences; this is due to the fact that the friction differences in these regions are not as large as for 5_S and 5_S_50 and thereby do not cause

significantly different worn surfaces. This is another indication that fluctuations in friction coefficient result in differently worn surfaces.
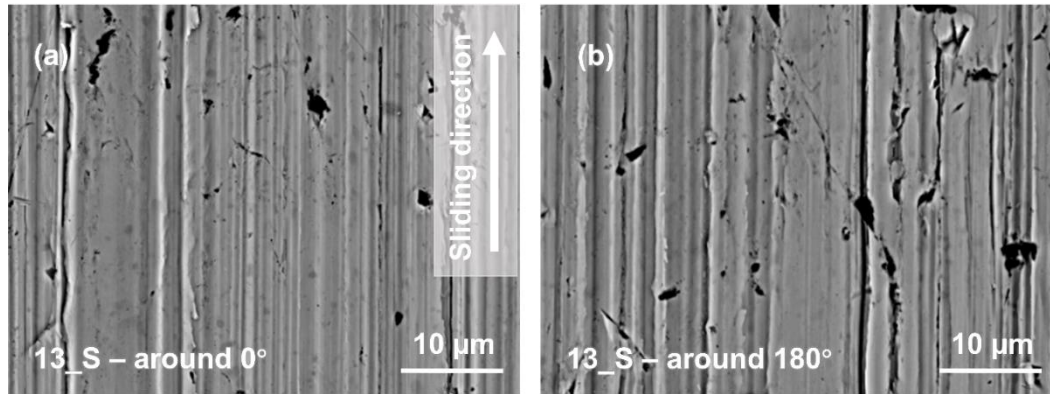
Figure 5.9: SEM images of 13_S, tested with the 13 µm slurry and small waviness; friction coefficient was comparable along the sliding track: (a) around 0° (the boundary between zone 1 and zone 8) ;(b) 180° (the boundary between zone 4 and zone 5). From [103] with permission.

Owing to the complexity of any waviness profile, simple scalar quantities like R_a and W_t can only be first order approximations when it comes to the effect that the whole profile has on the properties of the tribological system, even if these scalar quantities (e.g., R_a and W_t) are commonly used to define surface topography during a manufacturing process. Our data strongly suggests that apparent friction coefficient fluctuations, as they are most prevalent in literature, are the result of a variation in friction coefficients along the sliding track. These fluctuations are themselves the result of the waviness profile. Finally, this also leads to uneven wear on the loaded surfaces.

While it is somewhat surprising to discover that such minor deviations (as a 2 µm height tiny "hill" along a 132 mm sliding track) in the waviness profile does increase the friction coefficient by 91%, as demonstrated in Figure 5.5b, the relationship between the waviness profile and the tribological behavior is intricate and non-monotonic. In other words, the friction coefficient does not consistently respond to each hill in the waviness profile. For example,
92

5_S_50 in Figure 5.6 depicts a waviness profile with two peaks, and the friction coefficient along the sliding track only exhibits a single peak. What other factors influence how friction reacts to waviness profiles? The following section will expound on this question.

5.3 Predicting Abrasive Wear

Undesirable scratches and grooves on lubricated contact surfaces are oftentimes inevitable. An example is given in Figure 4.22 and Figure 4.13; the "unsatisfactory-lubricated experiments", as its name implies, are not what can be expected but could not be gotten rid of. The "unsatisfactory-lubricated experiments" represent the tests where adding the lubricant does not yield the desired outcome, leading to friction coefficients that are either not sufficiently low or exhibit significant fluctuations compared with "well-lubricated experiments".

Despite following the established testing protocol for lubricated experiments in this thesis (in chapter 3.3.3) and using strict sample standards (in chapter 3.1), the "unsatisfactory-lubricated experiments" still have a higher friction coefficient and greater frictional fluctuations compared with the well-lubricated experiment in Figure 4.13. The presence of abrasive grooves on the worn surface in Figure 4.22 suggests that abrasive wear contributed to the unsatisfactory experiments. Notably, the formation of these grooves appears to be strongly correlated with the magnitude of friction, with higher friction regions exhibiting more pronounced grooves than those with lower friction, as indicated by Figure 4.22.

Typically, such experiments are considered to produce anomalous results, which are often treated as outliers in further analyses [159,160]. Identifying the precise cause of the abrasive wear in such experiments is challenging; however, if we shift our attention from identifying the reason for the unsatisfactory lubrication to predicting the locations where most wear may

form, will we possibly predict where the wear occurs? In what follows, the data presented in this thesis will support the prediction of inconsistent friction and uneven wear along the sliding track.

5.3.1   The Influence of Oscillation

In section 5.2, we were astonished to find that even minor deviations (a 2 µm height gentle "hill" along a 132 mm sliding track) in the waviness profile can increase the friction coefficient by 91%. Similar observations are found between the waviness profile and the friction coefficient, as evident in Figure 4.15a, Figure 4.16, and Figure 4.17.

However, the friction coefficient does not respond consistently to each hill or feature in the waviness profile. If we only examine the waviness profile and the friction coefficient (in Figure 4.15a, Figure 4.16, and Figure 4.17), could the impact of the waviness profile on the tribological performance be considered randomly generated? The reason for such a situation might be that the inevitable experimental and instrumental deviations (e.g., the oscillation induced by the mounting tilt) play a crucial role, even if they are minimized and controlled to the highest degree possible.

When directly comparing oscillations and the angle-resolved friction coefficients, there is no obvious correlation between these two quantities. To describe the relationship between oscillation and angle-resolved friction coefficient, a new parameter, the Z-score of the friction coefficient, is introduced. The Z-score is used to show how the friction coefficient of a certain sector relates to the overall distribution of friction coefficient on the sliding track. As demonstrated by the Z-score analysis in Figure 4.21, the normalized friction coefficient negatively correlates with oscillations, particularly when the absolute Z-score exceeds one

(highlighted in red). This indicates that the locations where higher friction occurs along the frictional track tend to be strongly biased toward the negative slope of the oscillation.

This phenomenon can at least be partially explained by Popov's model, introduced in chapter 2.3.2, where the contact is modeled as a single Hookean spring, the sliding velocity is constant while the vertical spring oscillates. Popov's model, although it relies on stick-slip behavior, can be applied to enhance our understanding of the effects of oscillation on friction, even though stick-slip is not evident in the experiments of this thesis.

In this thesis, the oscillation induced by a disk mounting tilt is treated as a vertical oscillation. Popov's model predicts that the fluctuations of the friction force will coincide with the fluctuations of vertical oscillation, as shown in Figure 2.13. However, if stick-slip occurs, the maximum friction force will appear after the crest. This is because during the "stick phase", the condition for static friction holds according to:

$$F_{stick}(t) \; < \; \mu_0 F_z(t) \tag{5.4}$$

In equation (2.6), the stick force $F_{stick}(t)$ increases linearly. Therefore, in order to satisfy the condition for the end of the stick phase, where $F_{stick}(t_2) = \mu_0 F_z(t_2)$ as depicted in Figure 2.13, a decline in $\mu_0 F_z(t)$ is necassary. This requirement can only be met on the negative slope of the oscillation. In other words, within a period of vertical oscillation, the maximum frictional force will occur on the negative slope of the oscillation, as shown in Figure 2.13.

While this model is helpful, one cannot ascertain the existence of stick-slip in our frictional system. In the future, this model could be refined to better elucidate the influence of vertical oscillation on friction, especially without stick-slip. Nonetheless, further experimentation and theoretical investigations are necessary.

5.3.2   High Friction Predictor

The results in Figure 4.21 are from eleven individual experiments conducted under both lubricated (using FVA 1) and abrasive wear (using Al_2O_3 slurry) conditions; they clearly suggest the influence of oscillations on frictional behavior. In chapter 5.2, we elucidated the influence of the disk waviness profile on the frictional behavior. The question, then is, whether it is possible to integrate aspects from both waviness profile and oscillations to predict frictional behavior. Here, we introduce a novel tool, the "High Friction Predictor", which signifies sectors on the sliding track where high friction is likely to occur by integrating key features from both the disk waviness profile and the oscillation of the contacting surfaces.

To evaluate the "High Friction Predictor", we choose the "slope of oscillation" as the key feature for the oscillations. This choice is motivated by the observation in Figure 4.21, where the highest friction sectors tend to be strongly biased toward the negative slope of the oscillation. For the waviness, this thesis treats the "slope angle" (as shown in Figure 4.15b) as the key feature for evaluating the "High Friction Predictor", as previous research [161] has indicated that a positive slope angle (such as θ_1 in Figure 3.11) alters the contact between the surfaces, leading to a sharp increase in friction.

The "High Friction Predictor" was determined by selecting sectors (the sliding track is divided into 120 sectors) with both following features:

- In the waviness profile, the sectors that have a positive "slope angle" along the waviness profile
- In the oscillation of the contacting surfaces, the sectors that have a negative "slope of oscillation"

The "High Friction Predictor" is depicted by the gray stripes, as shown in Figure 5.10 (corresponding to the experiments shown in Figure 4.13).
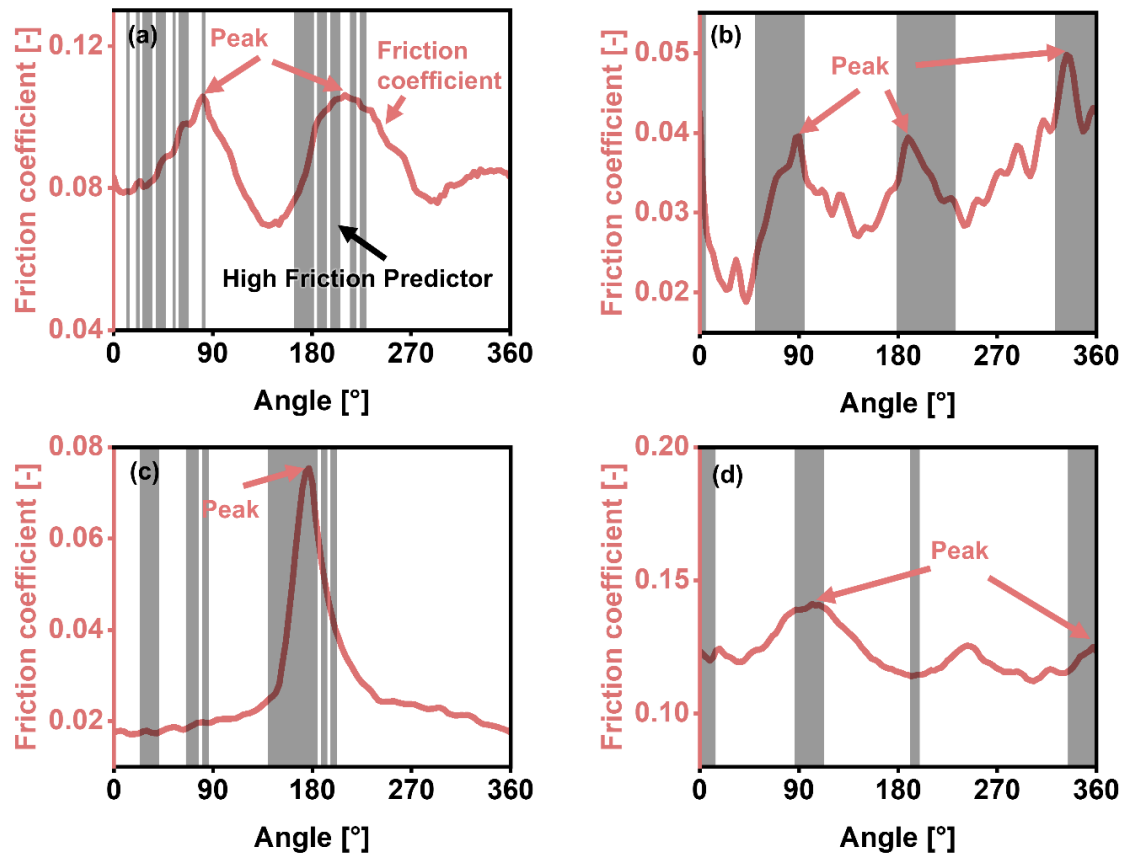
Figure 5.10: Angle-resolved friction coefficient (0 – 50 m) and "High Friction Predictor" for experiments shown in Figure 4.13; the "High Friction Predictor" is a term used to identify sectors on the sliding track where high friction is likely to occur: (a) "LTA (lubricated to abrasive) experiments", friction coefficient are from abrasive condition (2200-2600 s); (b) "well-lubricated experiments"; (c) "unsatisfactory-lubricated experiments"; (d) "abrasive experiments". The maximum friction coefficient on the sliding track is consistently located in the gray stripes specified by the "High Friction Predictor".

The "High Friction Predictor" for the repeats is shown in Figure 5.11. Upon close examination of sectors specified by the "High Friction Predictor" in Figure 5.10 and Figure 5.11, a consistent observation emerges: the maximum friction coefficient along the sliding track is consistently located in the gray stripes specified by the "High Friction Predictor" (except L4 in

Figure 5.11). Furthermore, it is worth noting that the peaks of the friction coefficient tend to be

located in the sectors specified by the "High Friction Predictor". For example in Figure 5.10b,

all three peaks of friction coefficient distinctly fall within the sectors marked by the "High

Friction Predictor".
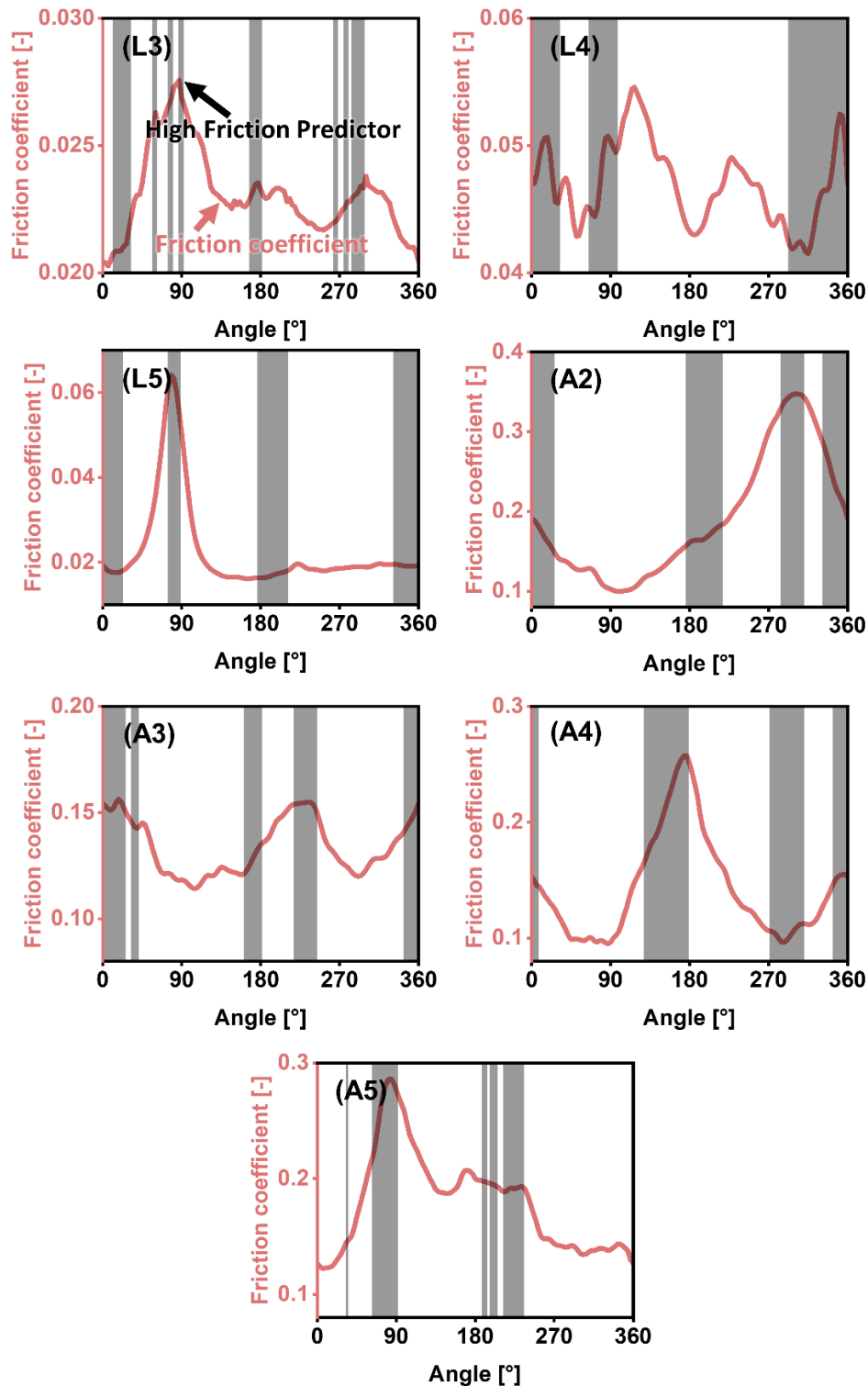
Figure 5.11: "High Friction Predictor" and angle-resolved friction coefficient (0 - 50 m) for abrasive wear experiments; the "High Friction Predictor" is a term used to identify sectors on the sliding track where high friction is likely to occur. (L3-L5) are repeats of lubricated experiments corresponding to the data in Figure 4.16 and Figure 4.19; (A2-A5) are repeats of abrasive wear experiments corresponding to the data in Figure 4.17 and Figure 4.20.

The "High Friction Predictor" is obtained only by integrating features from the disk waviness profile and the oscillation of the contacting surfaces. These features can be extracted before the tribology experiments, enabling us to determine where most friction and wear will occur along the sliding track before the tribological experiments even begin.

An example is the "unsatisfactory-lubricated experiments" in Figure 4.13c: We used the waviness profile and the oscillation data to evaluate the "High Friction Predictor" before the actual tribology experiment. It was possible to foresee that a location at around 180 ° (Figure 4.13c) might have a lot of grooves in case of abrasive wear, and this is indeed what was found after the experiment was conducted, as highlighted in Figure 4.22. This signifies that, before the operation of a tribological system, with the application of the "High Friction Predictor", one has the tool at hand to predict locations of high wear and thus also to prevent such conditions.

5.3.3   Predicting Abrasive Wear with Data from Well-lubricated Experiments

In this chapter, we only focus on the "LTA (lubricated to abrasive) experiments" in Figure 4.13. The "LTA (lubricated to abrasive) experiments" started under lubricated conditions using FVA 1 oil, and after 100 meters of sliding distance, we introduced 5 µm Al_2O_3 abrasive slurry to induce abrasion. The introduction of the abrasive slurry to the initially well-lubricated tribological system in Figure 4.13 causes a sharp rise in the friction coefficient, indicating a transition into an abrasive wear regime. The fluctuations in friction coefficient observed during abrasive wear are attributed to inconsistent friction along the sliding track, as shown in Figure 4.14. The angle-resolved friction coefficient exhibits the same trend for well-lubricated conditions and for abrasive wear, despite variations of up to two orders of magnitude in friction coefficient. This observation strongly suggests that fluctuations in friction are present for well-

lubricated conditions as well, as it might not be a big surprise to the tribology community. However, this means that one should be able follow a similar reasoning as what was presented above and allowing for predicting frictional fluctuations for abrasive wear conditions. In other words, the data from well-lubricated conditions can be used to predict future inconsistent friction and uneven wear.

5.3.4 Time-frequency Analysis

Periodic features in frictional signals are commonly observed in tribological experiments [111,112,156,162,163]. Short-Time Fourier Transform (STFT) based time-frequency analyses of tribological data have demonstrated their ability to identify periodic patterns as well as changes in states of operation. In a reciprocating tribological system [164], the dominant frequency in the frictional signal is typically fundamental frequency, as the friction force undergoes reciprocating periodic changes in sync with the variations in speed frequency. In the case of pin-on-disk setups, periodic structures in the frictional signal are observed as well. The results of this thesis indicate that this behavior is most likely due to the presence of surface topography (in Figure 5.5) and oscillations (in Figure 4.21), which affect tribological behavior. The periodic rotation of the disk causes periodic changes in the frictional signal. Therefore, although the natural frequency of 0.38 Hz (frequency of speed) is visible in Figure 4.23b, it is not necessarily the most dominant frequency. Surface topography and oscillations cause periodic changes with higher/lower frequencies as well. This serves as a reminder that the natural frequency should not always be considered the dominant frequency in tribology, as it is sometimes described in the literature [111,165,166].

In Figure 4.23a, after adding the abrasive slurry, the tribological system transitions from a well-lubricated to an abrasive wear condition. Simultaneously, in Figure 4.23b, it can be seen that a

continuous vertical spectrum appears after the addition of the slurry (at 2000 s), highlighting how time-frequency analysis can indicate a transition in the wear mechanism. The discrete frequency bands in Figure 4.23b at abrasive wear condition (2200-2600 s), e.g. 0.38 Hz and 6 Hz, are intensified compared to the well-lubricated condition (1200-1600 s). This suggests that the introduction of the slurry may have intensified the interactions between the pin and the disk without altering the periodic nature of the frictional behavior.

When carefully comparing the data before and after the addition of the slurry in Figure 4.23a and Figure 4.23b, as highlighted within a square between the two figures, it's clear that the continuous vertical spectrum appears a little bit before the sharp increase in friction coefficient. This phenomenon may be attributed to the fact that although the introduction of the abrasive slurry did not fully change the inherent periodic response of the pin and disk in the stable regimes (100-2000 s and 2200-2600 s), the tribological system may undergo a "running-in" upon the initial addition of the abrasive slurry to reach a stable state. During this "running-in" regime, the friction coefficient is on the verge of or continuously increasing, as observed in Figure 4.23b, with no dominant frequency, as indicated by the continuous vertical spectrum right after adding slurry at 2000 s. This observation highlights the potential of implementing the STFT algorithm in machines to prognosis abrasive wear and avoid high friction build-up by enabling proactive actions, such as supplementing lubricant, exchanging components, and even emergency machinery shutdowns.

6 Summary and Outlook

In this thesis, tribological tests were conducted in a flat-on-flat configuration with water-based Al_2O_3 slurries of varying particle sizes (5 and 13 µm) as the abrasive medium, employing 100Cr6 bearing steel for both pins and disks.

First, this work investigated the influence of the speed-induced hydrodynamic pressure on abrasive wear mechanisms. When utilizing the 5 µm sized Al_2O_3 slurry, a classical Stribeck curve like behavior was observed for the friction coefficient as well as an increase in film thickness. The speed-induced hydrodynamic effect extended the film thickness up to 14% and led to a friction reduction of about 2/3. When using the 5 µm slurry, the hydrodynamic effect resulted in a change of the dominating wear mechanism from microcutting and microploughing to fatigue wear as observed when the sliding speed increased from 50 mm/s to 400 mm/s. Simultaneously, a periodic pattern of indents was found on the worn surface at 400 mm/s using the 5 µm slurry. This observation provides strong evidence suggesting that the indentations on the worn surface were likely generated by the rolling of abrasive particles.

Second, we have persistently worked on unraveling a perplexing question: Why does the friction coefficient fluctuate dramatically during abrasive wear? In pursuit of this, we made every effort to mitigate potential sources of experimental deviations. For example, when preparing the disk, the height difference along the 132 mm sliding track was strictly controlled, ensuring it remained within 2 µm. Likewise, upon mounting the disk, the height difference (namely the oscillation of the contacting surfaces) along the sliding track was maintained below 4 µm. Remarkably, our most significant findings emerged from these factors that are typically overlooked.

Waviness is a concept that only a few tribologists consider on a regular basis. However, our data suggest that even minimized and controlled disk waviness strongly influences the friction behavior, e.g., a "hill" of around 2 µm height (along the 132 mm sliding track) increases the friction coefficient by 91%. The local difference in friction coefficient is the reason behind these large frictional fluctuations observed in abrasive wear conditions. Tribological systems with smaller abrasive particles (e.g., in 5 µm slurry) are more sensitive to the waviness profile than systems with larger particles (e.g., in 13 µm slurry). However, the relationship between the waviness profile and the frictional behavior is intricate and non-monotonic. Then, another commonly overlooked factor, the oscillation of contacting surfaces (due to disk mounting tilt), was considered. By introducing the friction coefficient Z-score, we found that these minimized oscillations strongly influence tribological behavior. Specifically, areas that have the highest friction tend to exhibit a strong bias towards the negative slope of the oscillations.

There is an undeniable truth in tribology: frictional behavior is virtually impossible to exactly replicate. The findings presented in this thesis provide a comprehensible explanation for this inherent unrepeatability. Even with minimized and controlled surface topography and oscillation of contacting surfaces, there remains a substantial and previously unacknowledged impact on tribological behavior. As the surface topography and the oscillation in each experiment are unique, achieving complete replication in frictional behavior is inherently impossible!

By integrating key features from the disk waviness profiles and the oscillation of the contacting surfaces, we introduced a novel tool, the "High Friction Predictor", denoting areas along the sliding track where friction is most likely higher than at other areas. Both waviness profiles and oscillations are evaluated before the onset of the tribological contact. This signifies that, before the operation of a tribological system, with the application of the methods detailed in

this thesis, one has the tools at hand to predict locations of high friction and thus also to prevent such conditions.

Our findings also prompt new considerations for several fundamental concepts in tribology, such as the Stirbeck curve. As illustrated in Figure 2.2, in lubrication systems, the friction coefficient can be effectively reduced by appropriately increasing the lubrication film thickness through variations in viscosity, speed, or load. Then the questions arise:

- If lubrication film thickness increases, is this increase consistent along the sliding track?

- What kind of surface topography can result in a thicker lubrication film thickness?

- How does the oscillation of the contacting surfaces affect the lubrication film thickness and subsequently influence the tribological performance?

- Can film thickness be regulated by controlling oscillation?

However, given that every surface as well as each mounting process in real world experiments is inherently different, traditional approaches to control these variables can not be successfully employed to conclusively correlate surface topography and oscillation with tribological properties. This in turn means that there is a huge potential to tailor – and minimize – friction and wear once correlations have been established. It will then be possible to formulate guidelines for what kind of surface topographies and tilt of the surfaces are desired to achieve certain sets of tribological properties.

7 References

[1] Stachowiak GW, Batchelor AW. *Engineering tribology*. Butterworth-Heinemann; 2013.

[2] Deshpande P, Pandiyan V, Meylan B, Wasmer K. Acoustic emission and machine learning based classification of wear generated using a pin-on-disc tribometer equipped with a digital holographic microscope. *Wear* (2021) 203622.

[3] Azad K, Rasul MG, Khan M, Sharma SC. Ecofuel and its compatibility with different automotive metals to assess diesel engine durability. In: Advances in Eco-Fuels for a Sustainable Environment. Elsevier; 2019, p. 337–351.

[4] Mindivan H, Tekmen C, Dikici B, Tsunekawa Y, Gavgali M. Wear behavior of plasma sprayed composite coatings with in situ formed Al2O3. *Materials & Design* 10 (2009) 4516–20.

[5] Great Britain. Department of Education and Science., Jost HP, Lubrication engineering Working Group. *Lubrication (tribology) education and research a report on the present position and industry's needs*. London: H.M. Stationery Off; 1966.

[6] Bo N. T. Persson. *Encyclopedia of lubricants and lubrication*. New York: Springer; 2014.

[7] Dowson D. *History of tribology.* 2nd ed. London: Professional Engineering Publishing; 1989.

[8] Hutchings IM. Leonardo da Vinci's studies of friction. *Wear* (2016) 51–66.

[9] Czichos H (ed.). Tribologie-Handbuch: Tribometrie, Tribomaterialien, Tribotechnik. 4th ed. Wiesbaden: Springer Vieweg; 2015.

[10] Bowden FP, Tabor D. *The friction and lubrication of solids*. Oxford, New York: Clarendon Press; Oxford University Press; 2001, 1954.

[11] Dyson J, Hirst W. The True Contact Area Between Solids. *Proceedings of the Physical Society. Section B* 4 (1954) 309–12.

[12] Eguchi M, Shibamiya T, Yamamoto T. Measurement of real contact area and analysis of stick/slip region. *Tribology International* 11-12 (2009) 1781–91.

[13] Weber B, Suhina T, Junge T, Pastewka L, Brouwer AM, Bonn D. Molecular probes reveal deviations from Amontons' law in multi-asperity frictional contacts. *Nature communications* 1 (2018) 888.

[14] Persson BNJ. Fluid Leakage in Static Rubber Seals. *Tribology Letters* 2 (2022).

[15] Garabedian NT, Bhattacharjee A, Webster MN, Hunter GL, Jacobs PW, Konicek AR et al. Quantifying, Locating, and Following Asperity-Scale Wear Processes Within Multiasperity Contacts. *Tribology Letters* 3 (2019).

[16] zum Gahr K-H. *Microstructure and wear of materials*. Amsterdam, New York: Elsevier; 1987.

[17] Bhushan B. *Introduction to tribology*. Chichester, West Sussex: John Wiley & Sons Inc; 2013.

[18] Richard Stribeck. *Die Wesentlichen Eigenschaften der Gleit- und Rollenlager*. Z. Ver. deutsch. Ing; 1902.

[19] Schreiber PJ. *Die tribologischen Eigenschaften Silicium-basierter Keramiken in Isooctan unter Berücksichtigung der Umgebungsatmosphäre*. Karlsruhe; 2019.

[20] Palacio M, Bhushan B. A Review of Ionic Liquids for Green Molecular Lubrication in Nanotechnology. *Tribology Letters* 2 (2010) 247–68.

[21] Zhou F, Liang Y, Liu W. Ionic liquid lubricants: designed chemistry for engineering applications. *Chemical Society reviews* 9 (2009) 2590–9.

[22] Neale MJ. *Lubrication and reliability handbook*. Boston, Oxford: Butterworth-Heinemann; 2001.

[23] Digitales Tonrundfunksystem_- Spezifikation des DAB-Befehlssatzes für Empfänger (DCSR); Deutsche Fassung EN_50320:2000. Berlin: Beuth Verlag GmbH. https://doi.org/10.31030/9126901.

[24] Davis JR. *Surface engineering for corrosion and wear resistance*. Materials Park, Ohio, Great Britain: ASM International Institute of Materials; 2001.

[25] Stolarski TA. *Tribology in machine design*. Oxford England, Boston: Butterworth Heinemann; 2000.

[26] Stachowiak GW, Batchelor AW. *Engineering tribology*. 3rd ed. Amsterdam [u.a.]: Elsevier Butterworth-Heinemann; 2005.

[27] Holmberg K, Kivikytö-Reponen P, Härkisaari P, Valtonen K, Erdemir A. Global energy consumption due to friction and wear in the mining industry. *Tribology International* (2017) 116–39.

[28] Petrica M, Badisch E, Peinsitt T. Abrasive wear mechanisms and their relation to rock properties. *Wear* 1-2 (2013) 86–94.

[29] Wang L, Qiao Z, Qi Q, Yu Y, Li T, Liu X et al. Improving abrasive wear resistance of Si3N4 ceramics with self-matching through tungsten induced tribochemical wear. *Wear* (2022) 204254.

[30] Stachowiak GW, Batchelor AW (eds.). Engineering Tribology (Fourth Edition). Boston: Butterworth-Heinemann; 2014.

[31] Winer WO, Peterson MB (eds.). Wear control handbook. New York, N.Y.: American Society of mechanical engineers; 1980.

[32] Rabinowicz E, Dunn LA, Russell PG. A study of abrasive wear under three-body conditions. *Wear* 5 (1961) 345–55.

[33] Czichos H. *Tribology*: A Systems Approach to the Science and Technology of Friction, Lubrication, and Wear. Burlington: Elsevier; 1978.

[34] Trezona RI, Allsopp DN, Hutchings IM. Transitions between two-body and three-body abrasive wear: influence of test conditions in the microscale abrasive wear test. *Wear* (1999) 205–14.

[35] Resendiz-Calderon CD, Cázares-Ramírez I, Samperio-Galicia DL, Farfan-Cabrera LI. Method for conducting micro-abrasion wear testing of materials in oscillating sliding. *MethodsX* (2022) 101703.

[36] Gahr K-H. Wear by hard particles. *Tribology International* 10 (1998) 587–96.

[37] Sin H, Saka N, Suh NP. Abrasive wear mechanisms and the grit size effect. *Wear* 1 (1979) 163–90.

[38] Nathan GK, Jones W. The empirical relationship between abrasive wear and the applied conditions. *Wear* 4 (1966) 300–9.

[39] Misra A, Finnie I. A classification of three-body abrasive wear and design of a new tester. *Wear* 1 (1980) 111–21.

[40] Misra A, Finnie I. Some observations on two-body abrasive wear. *Wear* 1 (1981) 41–56.

[41] Misra A, Finnie I. Correlations between two-body and three-body abrasion and erosion of metals. *Wear* 1 (1981) 33–9.

[42] Ambrish Misra. On the size effect in abrasive and erosive wear. *Wear* (1981) 359–73.

[43] Williams JA, Hyncica AM. Mechanisms of abrasive wear in lubricated contacts. *Wear* 1 (1992) 57–74.

[44] Williams JA, Hyncica AM. Abrasive wear in lubricated contacts. *Journal of Physics D: Applied Physics* 1A (1992) A81-A90.

[45] Tressia G, Penagos JJ, Sinatora A. Effect of abrasive particle size on slurry abrasion resistance of austenitic and martensitic steels. *Wear* (2017) 63–9.

[46] Andrade M, Martinho RP, Silva F, Alexandre R, Baptista A. Influence of the abrasive particles size in the micro-abrasion wear tests of TiAlSiN thin coatings. *Wear* 1-4 (2009) 12–8.

[47] Ren X, Peng Z, Hu Y, Rong H, Wang C, Fu Z et al. Three-body abrasion behavior of ultrafine WC–Co hardmetal RX8UF with carborundum, corundum and silica sands in water-based slurries. *Tribology International* (2014) 179–90.

[48] Bose K, Wood R. Optimum tests conditions for attaining uniform rolling abrasion in ball cratering tests on hard coatings. *Wear* 1-4 (2005) 322–32.

[49] Gee MG, Gant A, Hutchings I, Bethke R, Schiffman K, van Acker K et al. Progress towards standardisation of ball cratering. *Wear* 1-6 (2003) 1–13.

[50] Petrica M, Katsich C, Badisch E, Kremsner F. Study of abrasive wear phenomena in dry and slurry 3-body conditions. *Tribology International* (2013) 196–203.

[51] Yu R, Chen Y, Liu S, Huang Z, Yang W, Wei W. Abrasive wear behavior of Nb-containing hypoeutectic Fe–Cr–C hardfacing alloy under the dry-sand/rubber-wheel system. *Materials Research Express* 2 (2019) 26535.

[52] Xiao H, Liu S, Guo Y, Wang D, Chen Y. Effects of Microscale Particles as Antiwear Additives in Water-Based Slurries with Abrasives. *Tribology Transactions* 2 (2016) 323–9.

[53] da Silva WM, Suarez MP, Machado AR, Costa HL. Effect of laser surface modification on the micro-abrasive wear resistance of coated cemented carbide tools. *Wear* 1-2 (2013) 1230–40.

[54] Vashishtha N, Sapate SG. Abrasive wear maps for High Velocity Oxy Fuel (HVOF) sprayed WC-12Co and Cr 3 C 2 −25NiCr coatings. *Tribology International* (2017) 290–305.

[55] Kumar S, Balasubramanian V. Effect of reinforcement size and volume fraction on the abrasive wear behaviour of AA7075 Al/SiCp P/M composites—A statistical analysis. *Tribology International* 1-2 (2010) 414–22.

[56] Qi J, Wang L, Yan F, Xue Q. The tribological performance of DLC-based coating under the solid–liquid lubrication system with sand-dust particles. *Wear* 1-2 (2013) 972–85.

[57] Yakubov GE, Branfield TE, Bongaerts J, Stokes JR. Tribology of particle suspensions in rolling-sliding soft contacts. *Biotribology* (2015) 1–10.

[58] Kalin M, Velkavrh I, Vižintin J. The Stribeck curve and lubrication design for non-fully wetted surfaces. *Wear* 5-8 (2009) 1232–40.

[59] Spikes HA. Some Challenges to Tribology Posed by Energy Efficient Technology. In: Tribology for Energy Conservation, Proceedings of the 24th Leeds-Lyon Symposium on Tribology. Elsevier; 1998, p. 35–47.

[60] Braun D, Greiner C, Schneider J, Gumbsch P. Efficiency of laser surface texturing in the reduction of friction under mixed lubrication. *Tribology International* (2014) 142–7.

[61] Greiner C, Schäfer M. Bio-inspired scale-like surface textures and their tribological properties. *Bioinspiration & biomimetics* 4 (2015) 44001.

[62] Hase A, Kazuho M, Yukio N, Koji S, Katsuya O (eds.). Visualization and Evaluation of Friction and Wear Phenomena for Brake Pads Using In Situ Observation and Acoustic Emission Measurement Method; 2015.

[63] Ma G, Wang L, Gao H, Zhang J, Reddyhoff T. The friction coefficient evolution of a TiN coated contact during sliding wear. *Applied Surface Science* (2015) 109–15.

[64] Haug C, Molodov D, Gumbsch P, Greiner C. Tribologically induced crystal rotation kinematics revealed by electron backscatter diffraction. *Acta Materialia* (2022) 117566.

[65] Pastewka L, Moser S, Gumbsch P, Moseler M. Anisotropic mechanical amorphization drives wear in diamond. *Nature materials* 1 (2011) 34–8.

[66] Aghababaei R, Brink T, Molinari J-F. Asperity-Level Origins of Transition from Mild to Severe Wear. *Physical review letters* 18 (2018) 186105.

[67] Meine K, Schneider T, Spaltmann D, Santner E. The influence of roughness on friction. *Wear* 7-8 (2002) 733–8.

[68] Schreiber PJ, Schneider J. Liquid superlubricity obtained for self-mated silicon carbide in nonaqueous low-viscosity fluid. *Tribology International* (2019) 7–14.

[69] Morstein CE, Klemenz A, Dienwiebel M, Moseler M. Humidity-dependent lubrication of highly loaded contacts by graphite and a structural transition to turbostratic carbon. *Nature communications* 1 (2022) 5958.

[70] Jacobs TDB, Pastewka L. Surface topography as a material parameter. *MRS bulletin* 12 (2022) 1205–10.

[71] Hanaor DA, Gan Y, Einav I. Contact mechanics of fractal surfaces by spline assisted discretisation. *International Journal of Solids and Structures* (2015) 121–31.

[72] Aghababaei R, Brodsky EE, Molinari J-F, Chandrasekar S. How roughness emerges on natural and engineered surfaces. *MRS bulletin* (2023).

[73] American Society of Mechanical Engineers. *Surface texture*: Surface roughness, waviness, and lay. New York: American Society of mechanical engineers; 6/30/2020.

[74] DIN EN ISO 4287:2010-07, Geometrische Produktspezifikation (GPS)_- Oberflächenbeschaffenheit: Tastschnittverfahren_- Benennungen, Definitionen und Kenngrößen der Oberflächenbeschaffenheit (ISO_4287:1997_+ Cor_1:1998_+ Cor_2:2005_+ Amd_1:2009); Deutsche Fassung EN_ISO_4287:1998_+ AC:2008_+ A1:2009. Berlin: Beuth Verlag GmbH. https://doi.org/10.31030/1699310.

[75] Persson BNJ. Theory of rubber friction and contact mechanics. *The Journal of Chemical Physics* 8 (2001) 3840–61.

[76] Elson JM, Bennett JM. Calculation of the power spectral density from surface profile data. *Applied optics* 1 (1995) 201–8.

[77] Stover JC. *Optical scattering*: Measurement and analysis / John C. Stover. 3rd ed. Bellingham, Wash.: SPIE Press; 2012.

[78] Jacobs TDB, Junge T, Pastewka L. Quantitative characterization of surface topography using spectral analysis. *Surface Topography: Metrology and Properties* 1 (2017) 13001.

[79] Duparré A, Ferre-Borrull J, Gliech S, Notni G, Steinert J, Bennett JM. Surface characterization techniques for determining the root-mean-square roughness and power spectral densities of optical components. *Applied optics* 1 (2002) 154–71.

[80] Gujrati A, Khanal SR, Pastewka L, Jacobs TDB. Combining TEM, AFM, and Profilometry for Quantitative Topography Characterization Across All Scales. *ACS applied materials & interfaces* 34 (2018) 29169–78.

[81] Al-Samarai RA, Haftirman KRA, Al-Douri Y. The Influence of Roughness on the Wear and Friction Coefficient under dry and lubricated sliding. *Int. J. Sci. Eng. Res* 4 (2012) 1–6.

[82] Kubiak KJ, Liskiewicz TW, Mathia TG. Surface morphology in engineering applications: Influence of roughness on sliding and wear in dry fretting. *Tribology International* 11 (2011) 1427–32.

[83] Shi R, Wang B, Yan Z, Wang Z, Dong L. Effect of Surface Topography Parameters on Friction and Wear of Random Rough Surface. *Materials (Basel, Switzerland)* 17 (2019).

[84] Liang G, Schmauder S, Lyu M, Schneider Y, Zhang C, Han Y. An Investigation of the Influence of Initial Roughness on the Friction and Wear Behavior of Ground Surfaces. *Materials (Basel, Switzerland)* 2 (2018).

[85] Raja J, Muralikrishnan B, Fu S. Recent advances in separation of roughness, waviness and form. *Precision Engineering* 2 (2002) 222–35.

[86] Chang W-R, Grönqvist R, Hirvonen M, Matz S. The effect of surface waviness on friction between Neolite and quarry tiles. *Ergonomics* 8 (2004) 890–906.

[87] Wang Y, Li C, Du J, Morina A. Understanding the Influences of Multiscale Waviness on the Elastohydrodynamic Lubrication Performance, Part I: The Full-Film Condition. *Lubricants* 12 (2022) 368.

[88] Fridman HD, Levesque P. Reduction of Static Friction by Sonic Vibrations. *Journal of Applied Physics* 10 (1959) 1572–5.

[89] Kumar S, Wu CS, Padhy GK, Ding W. Application of ultrasonic vibrations in welding and metal processing: A status review. *Journal of Manufacturing Processes* (2017) 295–322.

[90] Ma C, Shamoto E, Moriwaki T, Zhang Y, Wang L. Suppression of burrs in turning with ultrasonic elliptical vibration cutting. *International Journal of Machine Tools and Manufacture* 11 (2005) 1295–300.

[91] Eaves AE, Smith AW, Waterhouse WJ, Sansome DH. Review of the application of ultrasonic vibrations to deforming metals. *Ultrasonics* 4 (1975) 162–70.

[92] Siegert K, Ulmer J. Superimposing Ultrasonic Waves on the Dies in Tube and Wire Drawing. *Journal of Engineering Materials and Technology* 4 (2001) 517–23.

[93] Murakawa M, Jin M. The utility of radially and ultrasonically vibrated dies in the wire drawing process. *Journal of Materials Processing Technology* 1-3 (2001) 81–6.

[94] Ashida Y, Aoyama H. Press forming using ultrasonic vibration. *Journal of Materials Processing Technology* (2007) 118–22.

[95] Socoliuc A, Gnecco E, Maier S, Pfeiffer O, Baratoff A, Bennewitz R et al. Atomic-scale control of friction by actuation of nanometer-sized contacts. *Science (New York, N.Y.)* 5784 (2006) 207–10.

[96] Carpick RW. Physics. Controlling friction. *Science (New York, N.Y.)* 5784 (2006) 184–5.

[97] Chowdhury MA, Helali M. The effect of amplitude of vibration on the coefficient of friction for different materials. *Tribology International* 4 (2008) 307–14.

[98] Teidelt E, Willert E, Filippov AE, Popov VL. Modeling of the dynamic contact in stick-slip microdrives using the method of reduction of dimensionality. *Physical Mesomechanics* 5-6 (2012) 287–92.

[99] Popov VL, Starcevic J, Filippov AE. Influence of Ultrasonic In-Plane Oscillations on Static and Sliding Friction and Intrinsic Length Scale of Dry Friction Processes. *Tribology Letters* 1 (2010) 25–30.

[100] Storck H, Littmann W, Wallaschek J, Mracek M. The effect of friction reduction in presence of ultrasonic vibrations and its relevance to travelling wave ultrasonic motors. *Ultrasonics* 1-8 (2002) 379–83.

[101] Popov M. The Influence of Vibration on Friction: A Contact-Mechanical Perspective. *Frontiers in Mechanical Engineering* (2020).

[102] Popov M, Popov VL, Popov NV. Reduction of friction by normal oscillations. I. Influence of contact stiffness. *Friction* 1 (2017) 45–55.

[103] Li Y, Garabedian N, Schneider J, Greiner C. Waviness Affects Friction and Abrasive Wear. *Tribology Letters* 2 (2023).

[104] Greiner C, Merz T, Braun D, Codrignani A, Magagnato F. Optimum dimple diameter for friction reduction with laser surface texturing: The effect of velocity gradient. *Surface Topography: Metrology and Properties* 4 (2015) 44001.

[105] Ruprecht AK, Körner K, Wiesendanger TF, Tiziani HJ, Osten Prof. Dr. sc. nat., Wolfgang, Lücke P et al. Chromatic confocal sensors for micro-topography measurements. *Maschinenbau von Makro bis Nano: 50. Internationales Wissenschaftliches Kolloquium, September, 19 - 23, 2005 ; proceedings* (2010) [05.2.03].

[106] Calvimontes A, Grundke K, Müller A, Stamm M. Advances for the Topographic Characterisation of SMC Materials. *Materials* 3 (2009) 1084–103.

[107] Leach R. *Optical Measurement of Surface Topography*. Berlin, Heidelberg: Springer Berlin Heidelberg; 2011.

[108] Masters BR. Confocal Laser Scanning Microscopy. *Microscopy research and technique* 4 (2012) 895–947.

[109] Hersey MD. The laws of lubrication of horizontal journal bearings. *Journal of the Washington Academy of Sciences* 19 (1914) 542–52.

[110] Salkind N. *Encyclopedia of Measurement and Statistics*. 2455 Teller Road, Thousand Oaks California 91320 United States of America: Sage Publications, Inc; 2007.

[111] Prost J, Boidi G, Lebersorger T, Varga M, Vorlaufer G. Comprehensive review of tribometer dynamics-Cycle-based data analysis and visualization. *Friction* 5 (2022) 772–86.

[112] Prost J, Boidi G, Varga M, Vorlaufer G, Eder SJ. Lifetime assessment of porous journal bearings using joint time-frequency analysis of real-time sensor data. *Tribology International* (2022) 107488.

[113] Cohen L. Time-frequency distributions-a review. *Proceedings of the IEEE* 7 (1989) 941–81.

[114] Menon AK, Boutaghou Z-E. Time–frequency analysis of tribological systems—part I: implementation and interpretation. *Tribology International* 9 (1998) 501–10.

[115] Huang NE, Shen Z, Long SR, Wu MC, Shih HH, Zheng Q et al. The empirical mode decomposition and the Hilbert spectrum for nonlinear and non-stationary time series analysis. *Proceedings of the Royal Society of London. Series A: Mathematical, Physical and Engineering Sciences* 1971 (1998) 903–95.

[116] Alonso MA. Wigner functions in optics: describing beams as ray bundles and pulses as particle ensembles. *Advances in Optics and Photonics* 4 (2011) 272.

[117] Taal CH, Hendriks RC, Heusdens R, Jensen J. An Algorithm for Intelligibility Prediction of Time–Frequency Weighted Noisy Speech. *IEEE Transactions on Audio, Speech, and Language Processing* 7 (2011) 2125–36.

[118] Wang WJ, McFadden PD. Early detection of gear failure by vibration analysis i. calculation of the time-frequency distribution. *Mechanical Systems and Signal Processing* 3 (1993) 193–203.

[119] Jeon H, Jung Y, Lee S, Jung Y. Area-Efficient Short-Time Fourier Transform Processor for Time–Frequency Analysis of Non-Stationary Signals. *Applied Sciences* 20 (2020) 7208.

[120] Li Y, Schreiber P, Schneider J, Greiner C. Tribological mechanisms of slurry abrasive wear. *Friction* 6 (2023) 1079–93.

[121] Zum Gahr K-H, Wahl R, Wauthier K. Experimental study of the effect of microtexturing on oil lubricated ceramic/steel friction pairs. *Wear* 5-8 (2009) 1241–51.

[122] Schneider J, Braun D, Greiner C. Laser Textured Surfaces for Mixed Lubrication: Influence of Aspect Ratio, Textured Area and Dimple Arrangement. *Lubricants* 3 (2017) 32.

[123] Galda L, Pawlus P, Sep J. Dimples shape and distribution effect on characteristics of Stribeck curve. *Tribology International* 10 (2009) 1505–12.

[124] Hansen E, Vaitkunaite G, Schneider J, Gumbsch P, Frohnapfel B. Establishment and Calibration of a Digital Twin to Replicate the Friction Behaviour of a Pin-on-Disk Tribometer (2023).

[125] Pondicherry KS, Rummel F, Laeuger J. Extended stribeck curves for food samples. *Biosurface and Biotribology* 1 (2018) 34–7.

[126] Lu X, Khonsari MM, Gelinck ERM. The Stribeck Curve: Experimental Results and Theoretical Prediction. *Journal of Tribology* 4 (2006) 789–94.

[127] Spikes HA. Boundary Lubrication and Boundary Films. In: Thin Films in Tribology, Proceedings of the 19th Leeds-Lyon Symposium on Tribology held at the Institute of Tribology, University of Leeds. Elsevier; 1993, p. 331–346.

[128] Spikes HA. Mixed lubrication — an overview. *Lubrication Science* 3 (1997) 221–53.

[129] Spikes HA, Olver AV. Basics of mixed lubrication. *Lubrication Science* 1 (2003) 1–28.

[130] Persson BNJ, Scaraggi M. On the transition from boundary lubrication to hydrodynamic lubrication in soft contacts. *Journal of physics. Condensed matter an Institute of Physics journal* 18 (2009) 185002.

[131] Liang H, Helen Xu G. Lubricating behavior in chemical–mechanical polishing of copper. *Scripta Materialia* 5 (2002) 343–7.

[132] Bahr M, Sampurno Y, Han R, Philipossian A. Improvements in Stribeck Curves for Copper and Tungsten Chemical Mechanical Planarization on Soft Pads. *ECS Journal of Solid State Science and Technology* 5 (2017) P290-P295.

[133] Rovani AC, Rosso TA, Pintaude G. On the Use of Microscale Abrasion Test for Determining the Particle Abrasivity. *Journal of Testing and Evaluation* 1 (2021) 20180576.

[134] Harsha AP, Tewari US. Two-body and three-body abrasive wear behaviour of polyaryletherketone composites. *Polymer Testing* 4 (2003) 403–18.

[135] Cozza RC, Tanaka DK, Souza RM. Friction coefficient and abrasive wear modes in ball-cratering tests conducted at constant normal force and constant pressure—Preliminary results. *Wear* 1-4 (2009) 61–70.

[136] Spikes HA, Olver AV, Macpherson PB. Wear in rolling contacts. *Wear* 2 (1986) 121–44.

[137] Wegener K. Ploughing. In: Produ TIAf, Laperrière L, Reinhart G, editors. CIRP Encyclopedia of Production Engineering. Berlin, Heidelberg: Springer Berlin Heidelberg; 2014, p. 1–7.

[138] Lawn B, Wilshaw R. Indentation fracture: principles and applications. *Journal of Materials Science* 6 (1975) 1049–81.

[139] Cook RF, Pharr GM. Direct Observation and Analysis of Indentation Cracking in Glasses and Ceramics. *Journal of the American Ceramic Society* 4 (1990) 787–817.

[140] Sun G, Bhattacharya S, White DR, McClory B, Alpas AT. Indentation Fracture Behavior of Low Carbon Steel Thermal Spray Coatings: Role of Dry Sliding-Induced Tribolayer. *Journal of Thermal Spray Technology* 8 (2018) 1602–14.

[141] Cook RF. Fracture sequences during elastic–plastic indentation of brittle materials. *Journal of Materials Research* 10 (2019) 1633–44.

[142] Blickensderfer R, Tylczak JH. A large-scale impact spalling test. *Wear* 3 (1983) 361–73.

[143] Greiner C, Liu Z, Schneider R, Pastewka L, Gumbsch P. The origin of surface microstructure evolution in sliding friction. *Scripta Materialia* (2018) 63–7.

[144] Haug C, Ruebeling F, Kashiwar A, Gumbsch P, Kübel C, Greiner C. Early deformation mechanisms in the shear affected region underneath a copper sliding contact. *Nature communications* (2020) 839.

[145] Dollmann A, Kauffmann A, Heilmaier M, Haug C, Greiner C. Microstructural changes in CoCrFeMnNi under mild tribological load. *Journal of materials science* (2020) 12353–72.

[146] Greiner C, Liu Z, Strassberger L, Gumbsch P. Sequence of Stages in the Microstructure Evolution in Copper under Mild Reciprocating Tribological Loading. *ACS applied materials & interfaces* 24 (2016) 15809–19.

[147] Landgraf RW. *Cyclic Deformation and Fatigue Behavior of Hardened Steels*: Mechanics Metals Steel. Urbana, Illinois; 1968.

[148] Bílý M. *Cyclic deformation and fatigue of metals*. Amsterdam, New York: Elsevier; 1993.

[149] Babitsky VI, Wittenburg J, Sosnovskiy LA. *Tribo-Fatigue*. Berlin, Heidelberg: Springer Berlin Heidelberg; 2005.

[150] Sciammarella CA, Chen R, Gallo P, Berto F, Lamberti L. Experimental evaluation of rolling contact fatigue in railroad wheels. *International Journal of Fatigue* (2016) 158–70.

[151] Brownlie F, Hodgkiess T, Galloway AM, Pearson A. Experimental Investigation of Engineering Materials under Repetitive Impact with Slurry Conditions. *Tribology Letters* 1 (2021).

[152] J.D. Gates. Two-body and three-body abrasion: A critical discussion. *Wear* (1998) 139–46.

[153] Torrance AA, d'Art JM. A study of lubricated abrasive wear. *Wear* 1 (1986) 49–59.

[154] Ramalho A, Miranda JC. The relationship between wear and dissipated energy in sliding systems. *Wear* 4-5 (2006) 361–7.

[155] Dante RC, Vannucci F, Durando P, Galetto E, Kajdas CK. Relationship between wear of friction materials and dissipated power density. *Tribology International* 6 (2009) 958–63.

[156] Hsiao E, Kim SH. Analyzing Periodic Signals in Rotating Pin-on-Disc Tribotest Measurements Using Discrete Fourier Transform Algorithm. *Tribology Letters* 2 (2009) 141–7.

[157] Godfrey D. Friction oscillations with a pin-on-disc tribometer. *Tribology International* 2 (1995) 119–26.

[158] Iida S, Nagai T, Uchiyama T. Standard wafer with programed defects to evaluate the pattern inspection tools for 300-mm wafer fabrication for 7-nm node and beyond. *Journal of Micro/Nanolithography, MEMS, and MOEMS* 02 (2019) 1.

[159] Guicciardi S, Melandri C, Lucchini F, Portu G de. On data dispersion in pin-on-disk wear tests. *Wear* 11-12 (2002) 1001–6.

[160] Farnham MS, Larson RE, Burris DL, Price C. Effects of mechanical injury on the tribological rehydration and lubrication of articular cartilage. *Journal of the mechanical behavior of biomedical materials* (2020) 103422.

[161] Sung I-H, Lee H-S, Kim D-E. Effect of surface topography on the frictional behavior at the micro/nano-scale. *Wear* 10 (2003) 1019–31.

[162] Wang DW, Mo JL, Zhu ZY, Ouyang H, Zhu MH, Zhou ZR. How do grooves on friction interface affect tribological and vibration and squeal noise performance. *Tribology International* (2017) 192–205.

[163] Menon AK, Boutaghou Z-E. Time–frequency analysis of tribological systems—part II: tribology of head–disk interactions. *Tribology International* 9 (1998) 511–8.

[164] Song J, Liu T, Shi H, Yan S, Liao Z, Liu Y et al. Time-frequency analysis of the tribological behaviors of Ti6Al4V alloy under a dry sliding condition. *Journal of Alloys and Compounds* (2017) 752–62.

[165] Li G, Lin Y, Wang H, Wei H, Wang G. Harmonic Wavelet Packet Analysis of Friction-Induced Vibration. *Tribology Transactions* 6 (2011) 895–901.

[166] Dweib AH, D'Souza AF. Self-excited vibrations induced by dry friction, part 1: Experimental study. *Journal of Sound and Vibration* 2 (1990) 163–75.